SAPIENZA
UNIVERSITÀ DI ROMA

A Parametric Acoustic Source for the Calibration of an Underwater Acoustic Apparatus for Ultra High Energy Astrophysical Neutrinos

Facoltà di Scienze Matematiche, Fisiche e Naturali

Corso di Laurea Magistrale in Astronomia e Astrofisica

Candidate

Greta Di Gravio

ID number 1552967

Thesis Advisor

Prof. Antonio Capone

Co-Advisor

Dr. Francesco Simeone

Academic Year 2017/2018

A Parametric Acoustic Source for the Calibration of an Underwater Acoustic Apparatus for Ultra High Energy Astrophysical Neutrinos

Master thesis. Sapienza – University of Rome

This thesis has been typeset by LaTeX and the Sapthesis class.

Author's email: greta.digravio@gmail.com

Ai miei nonni

«*O greggia mia che posi, oh te beata,*
che la miseria tua, credo, non sai!
Quanta invidia ti porto!
Non sol perché d'affanno
quasi libera vai;
ch'ogni stento, ogni danno,
ogni estremo timor subito scordi;
ma più perché giammai tedio non provi.»

Contents

Introduction

The discovery of cosmic rays in 1912 stated the beginning of particle physics. In the early 1900s experiments on cosmic rays, as the principal source of high energy particles, ensured lots of important achievements. With the advent of particles accelerators, the role of cosmic rays in particle physics became gradually marginal. However, they are still important for what concerns astrophysics and cosmology; indeed, cosmic rays and neutrinos, obviously along with photons, can give us information about the structure and evolution of the universe. In particular the neutrino, that is neutral and interacts only weakly, offer us the opportunity to study distant and energetic astrophysical objects. Neutrinos can travel from the source to the Earth unperturbed because they have a low probability of interacting with the interstellar medium (probability of interaction is proportional to the target density), then they can carry out important informations about astrophysical sources.

The detection of cosmic rays is a very broad topic, due to the various measurement techniques available and the great variety of particles existing. The method depends also on the energy range to measure. During this thesis optical and sound detections, of neutrinos, will be described.

This thesis project consists of the characterization of a parametric acoustic source to use in the calibration of an acoustic apparatus and it is arranged in five chapters.

Chapter 1 is an overview on the characteristics and origin of cosmic rays and the principal measurement techniques. The first part of the chapter is on the description of the spectrum and on the galactic and extragalactic origin of the high energy particles and the GZK effect. The second part focuses on neutrino detection, in particular optical (Čerenkov and hybrid) and sound (radio and acoustic) techniques, with a description of the principal experiments. There is particular attention on the motivations that support the sound detection, that allows to expand the volume of detection and to investigate neutrinos with ultra high energies.

Chapter 2 is dedicated to the acoustic signal induced by neutrino interaction in water. Its interactions in water and the thermo-acoustic model are described. There are also the description of the sound propagating in water, including the attenuation phenomena, and the introduction of the neutrino acoustic signal.

After the theoretical explanation of the neutrino acoustic pulse in water, we can illustrate the characterization of the parametric source in Chapter 3. It includes the analysis of the data acquired at the Insitute of Acoustics and Sensors "Orso Mario Corbino" [1]. After the apparatus description, that involves a parametric source, excited with sinusoidal input signals at various frequency, made by eight piezoelectric and an hydrophone immersed in a pool, the data analysis begins. The analysis has been made using the programming language MATLAB[2], and consists of the interpolation of the regular part of the data, acquired for several positions of the source, that could rotate around its axis, and various frequencies. Then we are able to study the response of the ceramics to different input signals.

This analysis is completed by the discussion made in Chapter 4. Starting from a bipolar pressure pulse generated from neutrino interaction in water, simulated with the ACoRNE program[3], we want to reconstruct the input signal that we have to apply to the parametric source to obtain this pulse. To do this we have used data obtained in Chapter 3 to estimate the parametric source transfer function and we have considered the attenuation phenomena in water. This analysis, like the previous one, has been made with MATLAB.

Finally, Chapter 5 is a summary of the previous chapters.

In addition, four appendices are included.

Appendix A contains the data acquired during the characterization of the parametric source. The data reported concern the beamsteering analysis and the study of the directivity of the source in the source plane and in a vertical plan.

Appendix B contains the MATLAB code used to calculate the theoretical beampattern, in order to compare it with data acquired during the study of the directivity of the source.

Appendix C includes the ACoRNE acoustic program, that simulates neutrino interactions in water that generate hadronic showers.

Appendix D concerns the MATLAB code used to estimate the transfer function of our parametric source and to figure out the input signal that we have to send to the source to generate a bipolar pressure pulse. This code takes in input the pressure pulse generated from neutrino interaction, simulated with the ACoRNE program.

Chapter 1

Interaction and Detection of Neutrinos

In this chapter the origin and the characteristics of cosmic rays (CRs), in particular neutrinos, are described. Measurement techniques and experiments dedicated to the study of CRs are then discussed.

1.1 Characteristics of Cosmic Rays

Cosmic rays are composed by ionized nuclei, mostly relativistic, (about 90% protons, 9% alpha particles and the rest heavier nuclei) that hit the atmosphere with different energies. Their origin and the mechanism by which they are accelerated are not yet fully known. Nearly all of them come from within the galaxy but, as we'll later find out, ultra high energy cosmic rays should have extragalactic origin. The investigation about this particles increases our knowledge both in astrophysical and particle physics fields, and gives also the opportunity to set up a link with cosmology.

As reported in [6], the energy spectrum in fig. 1.1 and fig. 1.2 has a broken power-law behaviour, like $E^{-\gamma}$, with some important features. For $E_{CR} \sim (3-4) \, PeV$ the index of the power law changes from $\gamma \approx 2.7$ to $\gamma \approx 3.1$; this region is called *knee*, and this feature of the spectrum is interpreted as a limit in the containment of CRs due to the galactic magnetic field. If we consider heavier nuclei, the change in the power law is located at higher energies; for example, the iron knee has been found at $80 \, PeV$ [7].

At energy $(0.4 - 0.7) \, EeV$ there is again a change in the energy spectrum, seen in many experiments (see [8]). For $E_{CR} > EeV$ it is visible one another change of the spectrum;
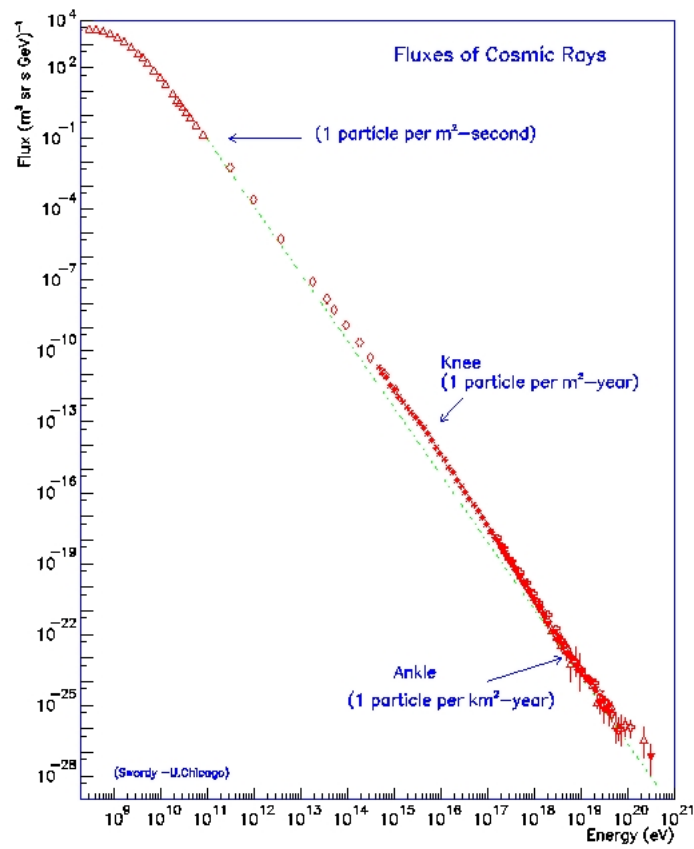
Figure 1.1. Cosmic ray spectrum [4].
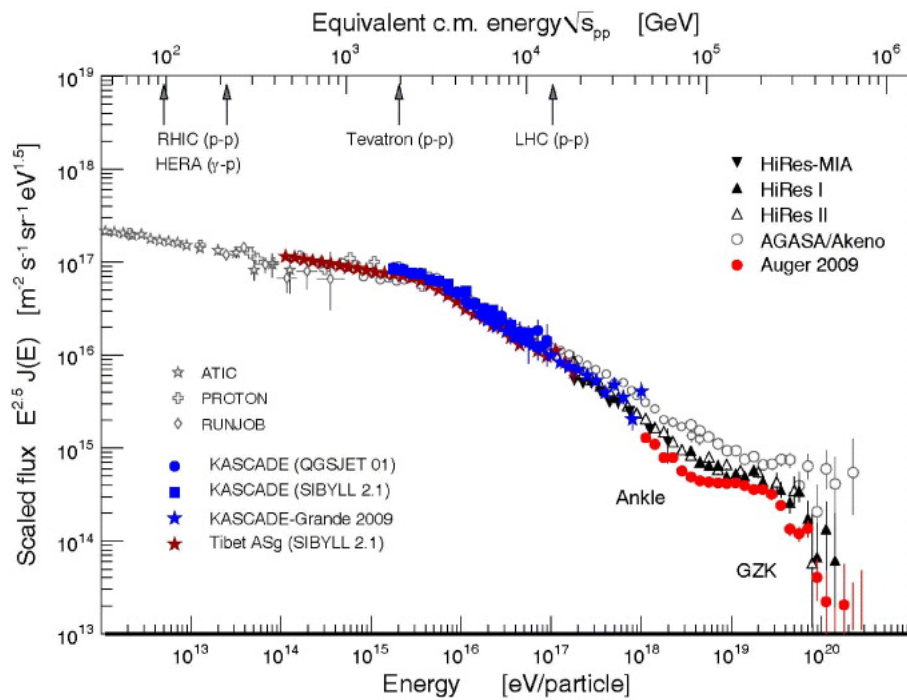
Figure 1.2. All-particle cosmic ray energy spectrum as obtained in direct measurements, multiplied by a factor $E^{2.5}$ [5].

this energy region is often interpreted as the transition from galactic to extragalactic CRs and is referred to as the *ankle*, observed by with HiRes [9], Telescope Array (TA) [10] and the Pierre Auger Observatory (PAO) [11, 12].

The highest energy feature is a steepening, the so-called *cutoff*, of the spectrum and it is found by HiRes [13], TA [14] and PAO [15], though the nature of this cutoff is still questionable. HiRes and TA data agree with theoretical prediction of GZK effect (it will be explained later) at $\approx 50\,EeV$, on the other hand PAO observed the cutoff at $(25.7 \pm 1.2)\,EeV$ [16]; this unexpected result might be explained as nuclei-photodisintegration [6].

1.1.1 High Energy Particle Sources

All sources where protons are accelerated are sources of high energy neutrinos, in fact the interaction of high energy hadrons with photons can generate charged pions that decay into neutrinos, for example through the following process:

$$p + \gamma \rightarrow n + \pi^+ \rightarrow n + \mu^+ + \nu_\mu \rightarrow n + e^+ + \bar{\nu}_\mu + \nu_e + \nu_\mu \qquad (1.1)$$

Dealing with acceleration models, the reference process that explains how particles gain energy through collisions with plasma is the so-called Fermi mechanism; it is still regarded as the fundamental explanation of the cosmic rays acceleration in astrophysical environments. There are two types of Fermi acceleration: first-order Fermi acceleration (concerning shocks waves) and second-order Fermi acceleration (concerning turbulent magnetic fields).

Galactic and extragalactic sources contribute in cosmic ray flux in different region of the spectrum, in particular the extragalactic component contributes maximally to its more energetic part [17, 18]. Galactic sources, actually, cannot contribute to the high energy part of the spectrum because galaxy dimensions and the magnetic field are not sufficient to accelerate particles to energies $> 10^{15}\,eV$.

Galactic Sources

Supernova remnants are, at present, the best candidate as galactic accelerator of cosmic rays. Shock waves can accelerate particles, using the Fermi mechanism, up to energies of about $10^{15}\,eV$ [19].

Particles may be accelerated also by pulsars-driven supernova remnants, reaching higher energies (about $10^{18}\ eV$ [20]).

Furthermore, microquasars have been proposed as sources of high energy neutrinos [21]; microquasars are galactic X-ray binary systems with accretion disk and jet emission, observed in the radio band.

Extragalactic Sources

Turning to high energy extragalactic sources, Active Galactic Nuclei (AGNs) and Gamma-Ray Bursts (GRBs) are the best candidates.

AGNs are supposed to be the most powerful emitters of radiation in the known universe [22]. They are galaxies with a supermassive black hole at their centre, and are characterized by the presence of accretion disk and jet emissions. Matter in the accretion disk feeds the black hole, and particles expelled in jets are accelerated by the Fermi mechanism. Both leptonic and hadronic acceleration processes are predicted, with consequent fluxes of gamma rays and neutrinos. However there are large uncertainties about the expected intensity of the neutrino flux, due to different models of AGNs [23, 24].

GRBs are sources characterized by very short violent gamma rays emissions. They are the brightest electromagnetic events known in the universe (they release $\sim 10^{51} - 10^{53}\ ergs$ in a few seconds), for a complete review check [25]. Observations indicate that GRBs are originated in cosmological sources, and that are produced by the dissipation of the kinetic energy of a relativistic expanding fireball [26].

Top-Down Models

The sources studied above are cosmic accelerators, and they are predicted in bottom-up models, that require an energy increase of CRs through repeated interactions between matter and radiation. On the contrary, top-down models expect that at least part of CRs come from a process of decay or annihilation of very energetic structures, as generally discussed in [27]. Bottom-up models involve standard physics, while top-down models necessitate new physics.

In the top-down scenario neutrinos can be produced from WIMPs (Weakly Interacting Massive Particles) particle-antiparticle annihilation [28]. Magnetic monopoles, massive relic particles and topological defects could decay and originate, like WIMPs, ultra high energy particles [29].

However, in these models there are many unknown parameters, and consequently, a lot of uncertainties in the predictions.

GZK Effect

GZK effect is an important signature of the Ultra High Energy (UHE) cosmic rays propagation through the Cosmic Microwave Background Radiation (CMBR). This theory was developed by Greisen [30], Zatsepin and Kuzmin [31] and states that UHECRs can interact with CMBR photons as follows:

$$p + \gamma_{CMBR} \rightarrow \Delta^+ \rightarrow \begin{cases} p + \pi^0 \\ n + \pi^+ \end{cases} \tag{1.2}$$
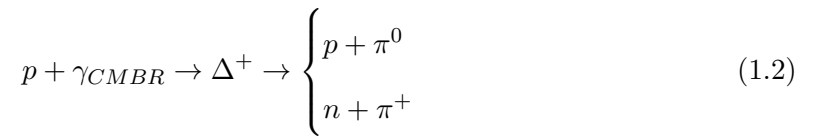
In the first case the final result is the pion decay into photons, but in the second case pions turns into muons and therefore neutrinos are produced.
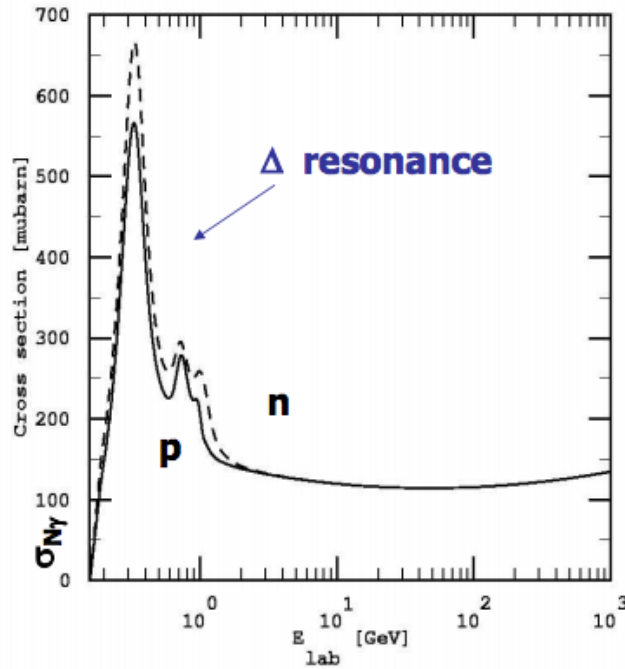
Figure 1.3. Cross section of the interaction between protons and CMBR photons.

This effect can be considered as a source of high energy neutrinos; if UHE neutrinos flux will be identified and proved that this flux agrees with the predictions, this will be a unique proof of the GZK existence and of the extragalactic origin of UHE particles.

1.2 Measurement Techniques

Neutrino is only weakly interacting and then, due to its small interaction cross section, is very difficult to detect. Neutrinos can be detected by identifying the particles (leptons and hadrons) originated in their interactions. Neutrino interactions with matter could be of two types: charged current interaction (CC) and neutral current interaction (NC). In the first case the neutrino converts into the corresponding lepton and generate an hadronic cascade; in the second one the neutrino generates another neutrino and the hadronic cascade.

Because of the very low value of the interaction cross section, we need huge and massive apparatus arranged to intercept as many events as possible. For this reasons natural elements are employed, like mountains, sea or ice. Big mass above the detector is very useful, in fact, to stop atmospheric particles, like muons, that are also produced in atmospheric neutrino charged current interactions and then can mimic a neutrino event. As stated before, the experimental apparatus detects the particles generated by the neutrino interactions: this can be obtained collecting light (Čerenkov and fluorescence techniques) or measuring acoustic or radio pulses . The first technique is widely used for neutrino energy in the interval $(10^8 - 10^{16})\ eV$, the second one, yet not fully exploited, seems to be optimal for $E_\nu > 10^{17}\ eV$.

In the following sections there is an explanation of the varies measurement methods and an overview on the important experiments, including references.

1.2.1 Optical Detection

A wide variety of experiments in physics are based on the optical detection of *Čerenkov radiation*. Čerenkov telescopes look for muons generated in the neutrino interactions in the medium surrounding the apparatus. Those detectors catch photons originated by the muons propagating at velocities greater than the speed of light, in a transparent medium. The apparatus consists of a grid of light collectors, or photomultiplier tubes (PMTs); studying the time of arrival of photons on the PMTs, is possible to reconstruct the particle track. The geometry of the emission depends on the refractive index of the medium; the wavefront is on the surface of a cone. As depicted in fig. 1.4, the aperture of the cone is called *Čerenkov angle*, and is defined by $\cos\varphi = \frac{1}{n\beta}$, where $\beta = \frac{v}{c}$.
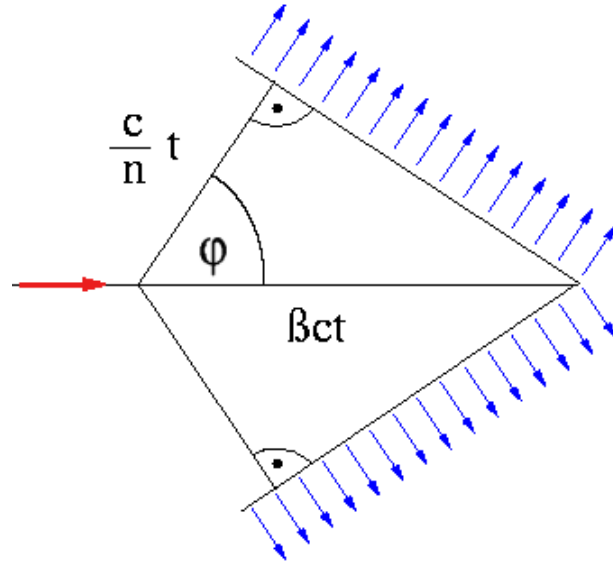
Figure 1.4. Geometry of the Čerenkov radiation. Image from https://commons.wikimedia.org/w/index.php?curid=215825.

The first realization of a Čerenkov telescope has been **Baikal**, located in Siberia [32]. Then **AMANDA** (Antarctic Muon And Neutrino Detector Array) [33] and its extension **IceCube** [34], located in Antarctica, have been built and are in operation about since 2010. IceCube is complemented by the surface array **IceTop** for air shower. In the Mediterranean Sea, after the pioneer attempt made by **NESTOR** to stimulate the construction of a neutrino telescope [35], the **ANTARES** (Astronomy with a Neutrino Telescope and Abyss environmental RESearch) collaboration built and operated the first deep sea Čerenkov detector [36]. Again in the Mediterranean Sea, **NEMO** (NEutrino Mediterranean Observatory) collaboration first [37] and the **KM3NeT** (Km^3 Neutrino Telescope) collaboration later [38], paved the road for the construction of the multi Km^3 abyssal Čerenkov Neutrino Telescope that will be complementary to IceCube.

Hybrid Detectors

Sometimes Čerenkov apparatuses are completed by *fly's eye* detectors, as we can see in fig. 1.5, that measure fluorescence in air. This light is due to the ionization of nitrogen as result of the passage of charged particles through the atmosphere. Fly's eye detection was first used in **HiRes** [39]; then in the hybrid experiments **Pierre Auger Observatory** (PAO) [40] and **Telescope Array** (TA) [41], that are, due to their huge dimensions, two of the most important current experiments for UHECRs and neutrinos.
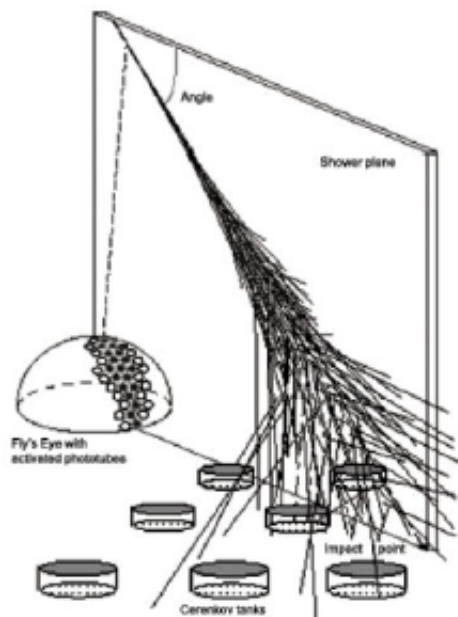
Figure 1.5. Detection techniques at the Pierre Auger Observatory: surface detectors measure Čerenkov light and fly's eyes catch the fluorescence caused by the particles in atmosphere [42].

1.2.2 Sound Detection

The Čerenkov technique is diffusely exploited at present but, since it is based on the detection of light, it would be too expensive to build an apparatus with a detection volume bigger than few km^3. In fact, the fluxes of astrophysical neutrinos follow a power law behaviour according to $E^{-(2.1-2.4)}$ so, for this reason, to detect neutrinos with $E > 10^{17}\,eV$ very big experiments are needed. The absorption length of Čerenkov light in water is $\lesssim 100\,m$, then the distance between PMTs should be of the same scale. In order to build a detector with volume bigger than a few km^3 too many PMTs would be needed, implying an excessive cost. Hence it is necessary to think about alternative techniques, as radio in air and acoustic detection in water (or ice), since sound and radio signals have a large attenuation length (order of kilometres). This means that detectors can be positioned with more spacing between adjacent units and we can have bigger apparatuses with fewer number of detectors.

Radio Detection

This technique is based on the so-called *Askaryan effect* [43], that consists in a coherent radio emission from neutrino interactions in dielectric media, due to negative charge excess. This effect is similar to the Čerenkov, and offers the possibility to use other natural elements, like sand and salt.

One of the most important experiment in this context is **ANITA** (ANtarctic Impulsive Transient Antenna), a balloon-borne radio telescope flying over Antarctica at an altitude of $35 - 40\,km$, monitoring an ice surface of $\sim 10^6\,km^3$ [44]. Another experiment that uses the Askaryan effect is **ARA** (Askaryan Radio Array), a large neutrino detector in the South Pole that detects neutrino pulses in ice [45].

Acoustic Detection

Neutrino interactions in water will be described in detail in the next chapter; however, in a few words, the acoustic detection is based on the *thermo-acoustic effect*, in according to which particles energy loss in the medium, causing a local heating, perturbs the thermal equilibrium and expands the medium, thus resulting in a pressure wave. The interesting aspect is the large value of the attenuation length of sound in water, that enables to have wide instrumented areas, using a relatively low number of sensors. By measuring the acoustic pulse with several sensors, the hydrophones, it is possible to reconstruct the neutrino trajectory.

A pioneering experiment was **SAUND** (Study of Acoustic Ultra high energy Neutrino Detection), in the Atlantic Ocean, that used existing military hydrophones. SAUND experiment used seven hydrophones arranged in a geometrical pattern (see fig. 1.6), and was able to set the first experimental upper limit on the flux of UHE neutrinos with the acoustic detection [46]. A similar experiment is **ACoRNE** (Acoustic Cosmic Ray Neutrino Experiment); similarly to the previous one, it employed military array, but this time in the United Kingdom [47].

Other experimental activities have allowed to improve the knowledge about acoustic signals in the Mediterranean Sea, in particular the **NEMO-OνDE** (Ocean Noise Detection Experiment) [48], **AMADEUS** (ANTARES Modules for the Acoustic Detection Under the Sea) [49] and **SMO** (Submarine Multidisciplinary Observatory) [50] ones.

NEMO-OνDE was a submarine station for real-time monitoring of acoustic background installed by the NEMO Collaboration, 25 km E offshore the port of Catania (Sicily) at a
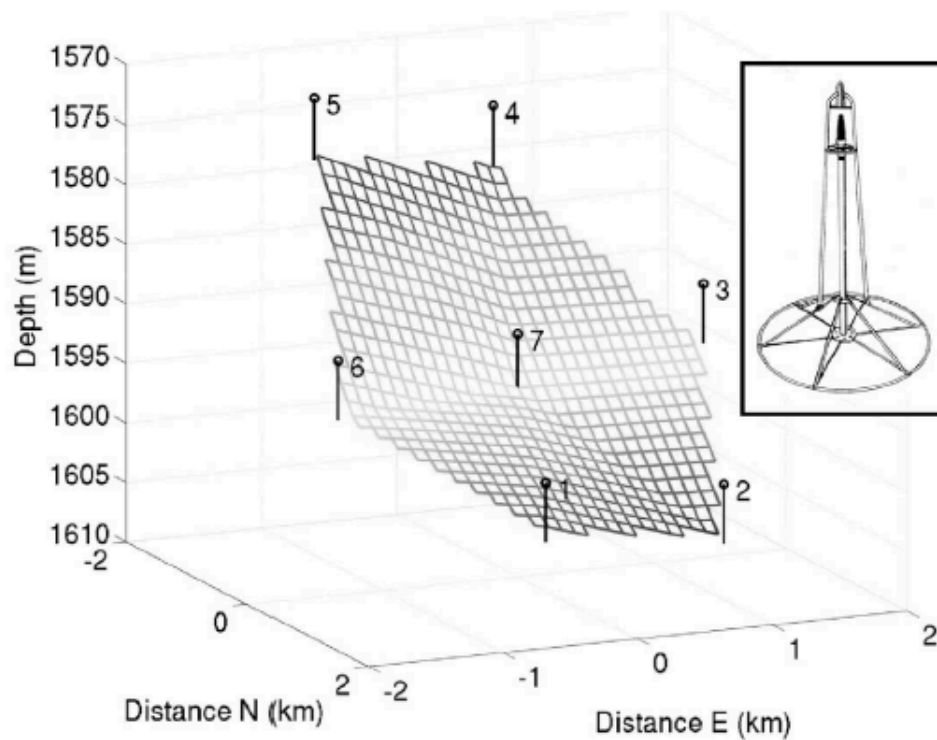
Figure 1.6. Schematic view of the seven SAUND hydrophones. The insert shows the structure that supports the hydrophones [46].

depth of 2000 m. The station was equipped with 4 hydrophones and operated for about two years starting from January 2005, acquiring more than 2000 hours of recordings. NEMO-OνDE have reported the average Power Spectral Noise in deep sea as well as identification of biological signals.

The AMADEUS project is fully integrated into the ANTARES Čerenkov neutrino telescope being part of its acoustic positioning system and it is composed by 18 sensors. Its main goal is to evaluate the feasibility of a future acoustic neutrino telescope in the deep sea operating in the ultra high energy regime. Among other results AMADEUS, during 2008, performed an analysis correlating the ambient acoustic noise level, in different frequency bands, with the surface weather data and performed a directional analysis of transient signals described in [51].

Chapter 2

Techniques and Principles of Acoustic Detection in Water

In this chapter we will describe the properties of neutrino interactions in water and the thermo-acoustic model, that is the basis of the acoustic detection.

2.1 Neutrino Interactions In Water

As hinted before, neutrinos interact with nucleons of the medium in which they are travelling in two ways: charged current interaction (CC) and neutral current interaction (NC). They are, respectively

$$\overset{\leftrightarrow}{\nu}_l + N \rightarrow l^{\pm} + X \tag{2.1}$$

$$\overset{\leftrightarrow}{\nu}_l + N \rightarrow \overset{\leftrightarrow}{\nu}_l + X \tag{2.2}$$

where l indicates the lepton flavour (e, μ, τ), N is the nucleon target, and X is the the hadronic shower generated in the interaction. In the NC interactions the outgoing neutrino cannot be detected, so the only visible part is the hadronic shower. In the case of CC interactions both leptonic and hadronic products can originate showers detectable with the acoustic technique.

Following [52], the differential cross section for neutrino interacting with nucleons is written, as a function of the Bjorken scaling variables $x = \frac{Q^2}{2M\nu}$ and $y = \frac{\nu}{E_\nu}$, as

$$\frac{d^2\sigma}{dxdy} = \frac{2G_F^2 ME_\nu}{\pi}\Big(\frac{M_W^2}{Q^2 + M_W^2}\Big)^2 [xq(x, Q^2) + x\bar{q}(x, Q^2)(1 - y^2)] \tag{2.3}$$

where ν is the hadronic shower energy, $G_F = 1.16632 \times 10^{-5}\, GeV^{-2}$ is the Fermi constant, q and $\bar{q}$ are the quark (and antiquark) distribution functions, M and M_W are the nucleon and intermediate-boson masses, Q is the four-momentum exchanged.

In fig. 2.1 the CC, NC and total cross sections are plotted.
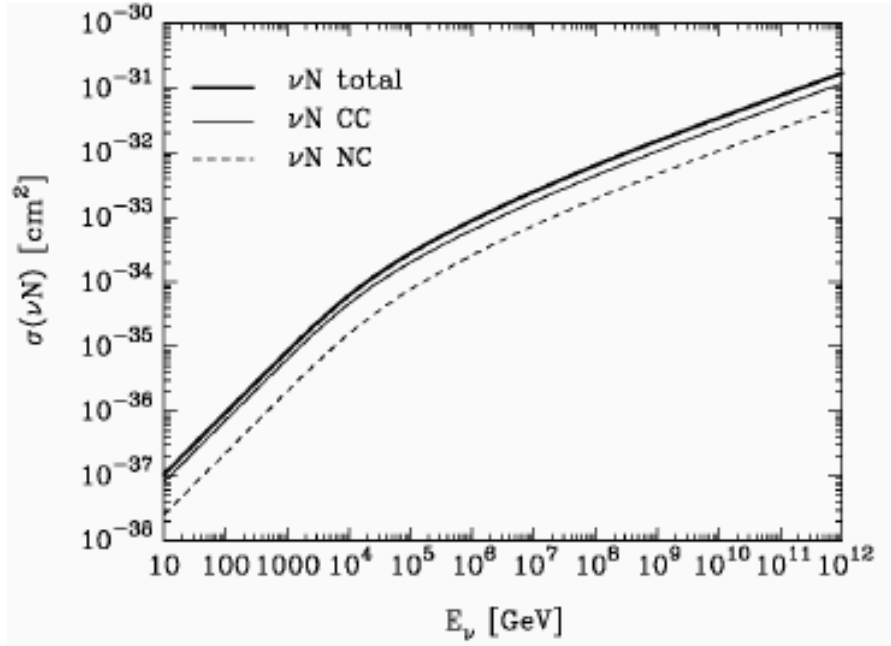
Figure 2.1. Cross sections for νN interactions as a function of the neutrino energy [52].

The ratio of the CC cross section over the total one is

$$\frac{\sigma_{CC}}{\sigma_{CC} + \sigma_{NC}} \approx 0.7 \tag{2.4}$$

then about 70% of the neutrino interactions with nucleons give a charged lepton.

2.1.1   LPM Effect

As has been said earlier, electromagnetic showers produced in CC interactions are the most abundant and retain most of the energy of the incident neutrino. However, when considering very high energy (above $10^{17}\, eV^1$), the *LPM effect* has to be taken into account. This effect alters the shower propagation and its significance increases with the energy of the primary neutrino. It was first noticed by Landau, Pomeranchuk and Migdal [54, 55, 56] and it consists in a suppression process reducing, above a certain energy, the bremsstrahlung (for electrons) and pair production (for photons) cross section. The

---

[1]LPM threshold is the energy at which this effect starts to be significant. For water the order of magnitude is $\sim 10^2\, TeV$ [53].

consequence is that the electromagnetic part of the shower elongates, the deposited energy density decreases and then there is a reduction of the amplitude of the acoustic pulse. In addition, the LPM effect introduces fluctuations on the longitudinal profile of the cascade that cause uncertainties in the modelling of the shower development [57].

The shower expansion and the fluctuations give a weaker and irregular signal, and this would require different positions of the hydrophones for the optimal detection. To avoid these complications, taking into account that the major contribution to the energy density is originated by the propagation of hadronic showers, only the hadronic component of the shower will be investigated when considering neutrino acoustic signals in water. An example of longitudinal profiles is shown in fig. 2.2.
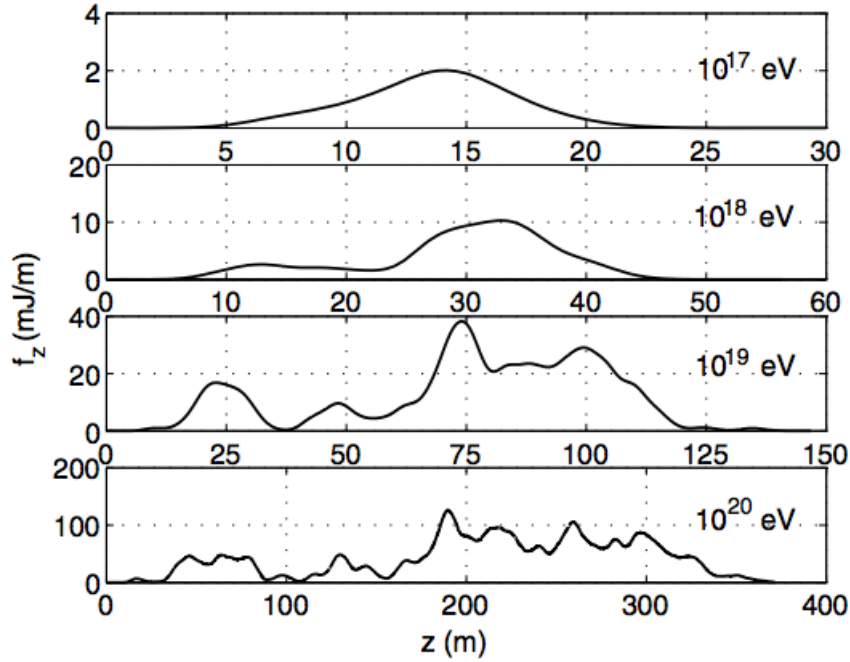
Figure 2.2. Examples of longitudinal distributions of electromagnetic showers at various energies. The cascade energies are indicated on the upper right part of each plot [57].

2.1.2 Thermo-Acoustic Model

As already mentioned in Chapter 1, the thermo-acoustic model describes the pressure wave generated by the energy dissipation[2] of the UHE particles interacting in water, by a deep inelastic scattering. This effect, and the application to the neutrino case, was first suggested by Askaryan [58].

Neutrinos interacting with the nuclei of water molecules, produce hadronic cascades. As the shower develops, the energy is deposited along the shower axis, causing an almost instantaneous heating in the surrounding medium that perturbs the thermal equilibrium and expands as a pressure wave. This effect is described by the following wave equation:

$$\nabla^2 p(\vec{r},t) - \frac{1}{v^2}\frac{\partial^2 p(\vec{r},t)}{\partial t^2} = -\frac{\beta}{C_p}\frac{\partial^2 q(\vec{r},t)}{\partial t^2} \qquad (2.5)$$

where v is the speed of sound in the medium, β is the thermal expansion coefficient, C_p is the specific heat coefficient at constant pressure, $p(\vec{r},t)$ is the pressure signal and finally the source term $q(\vec{r},t)$ is the energy deposition density. In this equation the parameters depend on the water properties (temperature, salinity and hydrostatic pressure). We could consider the Grüneisen coefficient $\gamma = \frac{\beta v^2}{C_p}$, to estimate the efficiency of the thermo-acoustic mechanism. Because of the dependence of this coefficient to the environmental parameters, it changes for different sites as visible in fig. 2.3.
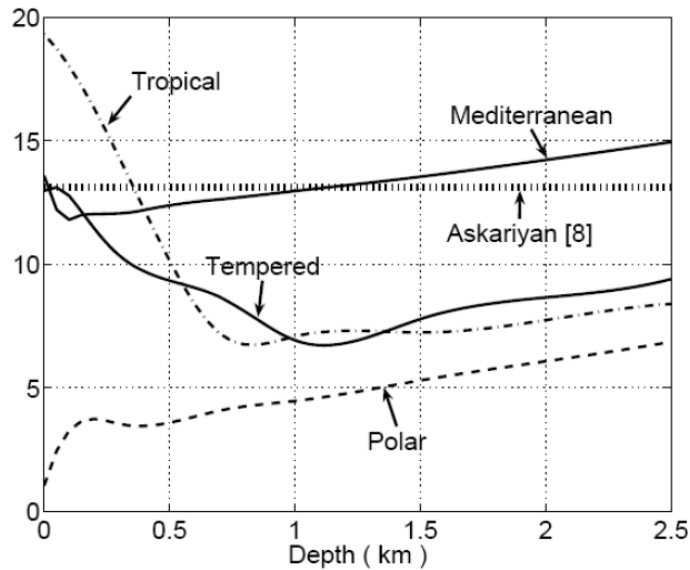
Figure 2.3. Value of the Grüneisen parameter as function of the depth, for different oceans and seas [57].

---

[2]The thermo-acoustic one is not the only dissipation mechanism, but is the most efficient. In fact, heat conduction and viscous friction have characteristic times bigger than that of the pressure wave.

The general solution of the eq. (2.5) is provided by the Kirchhoff integral

$$p(\vec{r}, t) = \frac{\beta}{4\pi \, C_p} \int \frac{1}{|\vec{r} - \vec{r}'|} \frac{\partial^2}{\partial \, t^2} q(\vec{r}', t - \frac{|\vec{r} - \vec{r}'|}{v}) dV' \qquad (2.6)$$

that may be simplified according to the hypothesis of instantaneous energy deposition. With this assumption, the source term can be expressed in such a way that $\dot{q}(\vec{r}, t) = q(\vec{r})\delta(t)$, where $\delta(t)$ is the delta function. As a consequence, the eq. (2.6) reduces to

$$p(\vec{r}, t) = \frac{\gamma}{4\pi} \frac{\partial}{\partial \, R} \int_S \frac{q(\vec{r}')}{R} d\sigma \qquad (2.7)$$

where the integration is computed over spherical surfaces centred on $\vec{r}$, with radius $R = vt$. This integral is the pressure in $\vec{r}$ at the time t as the sum of all contributions, that can reach this point, propagating at the speed of sound. As in evidence in eq. (2.7), the Grüneisen coefficient determines the amplitude of the resulting acoustic pulse.

As described in [59], the hadronic shower deposits the maximal part of the energy along the axis of the cascade in a cylindrical volume, typically of some tens centimetres radius and some tens metres length. This feature is visible in fig. 2.4 and fig. 2.5; these simulations are computed with CORSIKA[3] and then compared to the GEANT4[4] simulations. The shapes of the distributions are similar but differences appear increasing the energy, due to the physics models used in these programs.

---

[3]CORSIKA (COsmic Ray SImulation for Kaskade) is a program for simulations of extensive air showers that has been adapted to work in water or ice.

[4]GEANT4 (GEometry ANd Tracking) is a platform for simulations of the passage of particles through matter, developed by CERN.

Each element along the shower axis behaves as a point-like source; the resulting interference figure is called *acoustic pancake* and it lies in the plane perpendicular to the axis, as shown in fig. 2.6.
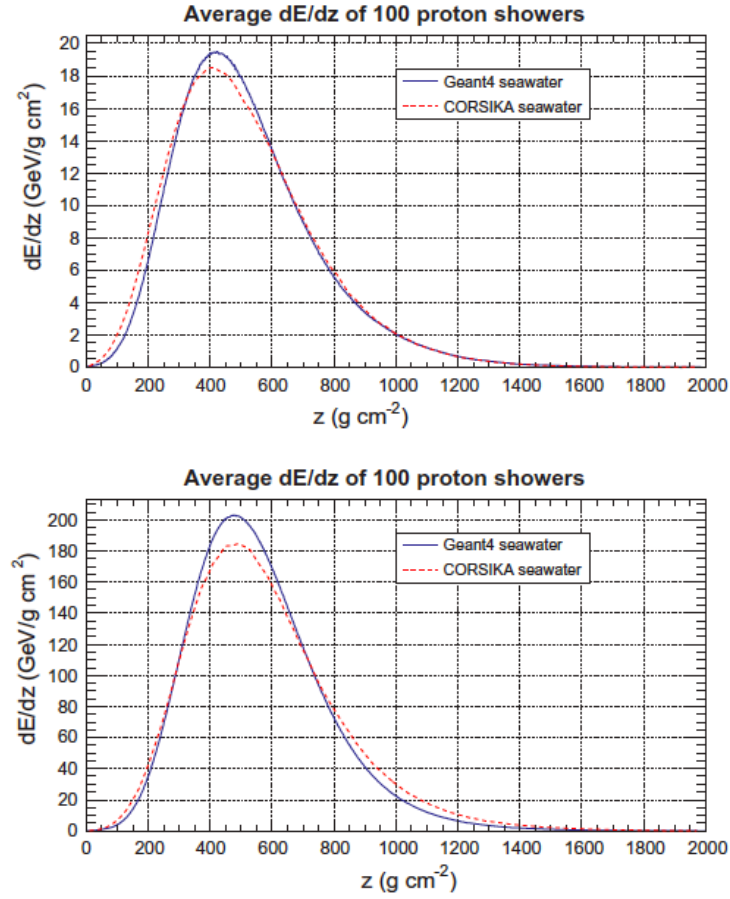
Figure 2.4. Averaged longitudinal energy deposited per unit path length of 100 proton showers at energy $10^4 \ GeV$ and $10^5 \ GeV$, respectively for the upper plot and lower plot, versus depth in the sea water [60].
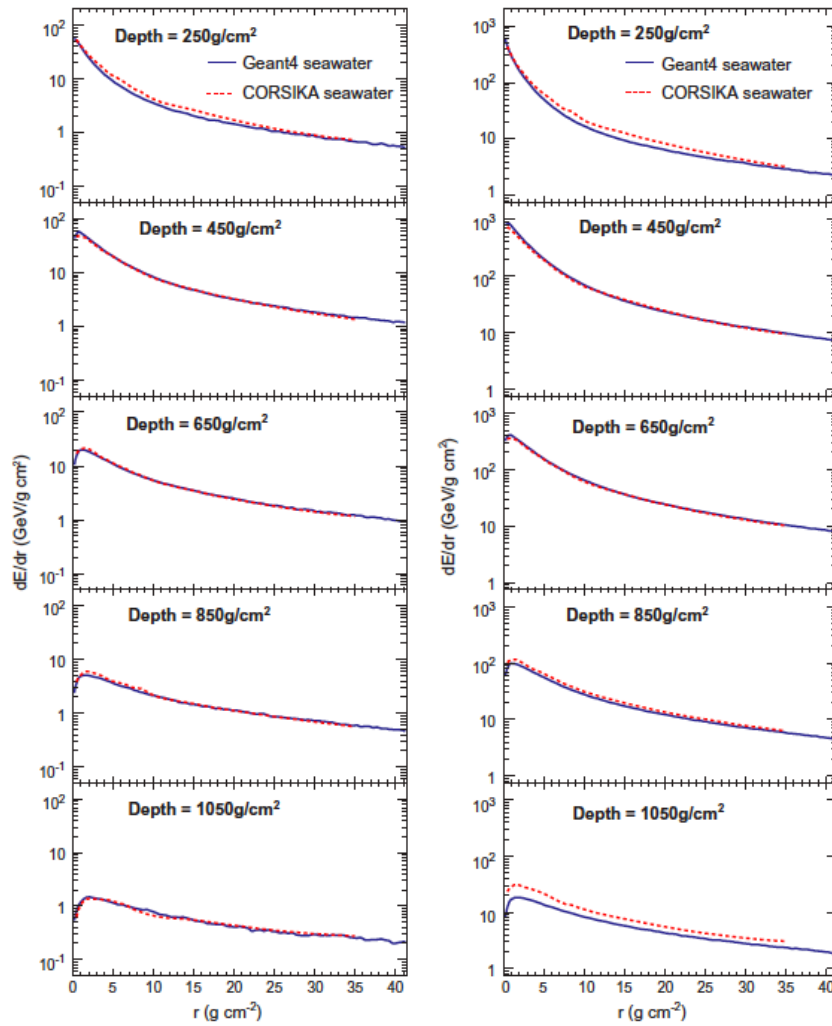
Figure 2.5. Averaged radial energy deposited per unit radial distance for 100 proton showers in sea $10^4\ GeV$ and $10^5\ GeV$, respectively for the left hand plots and right hand plots, versus distance from the axis in the water for different depths of the shower [60].
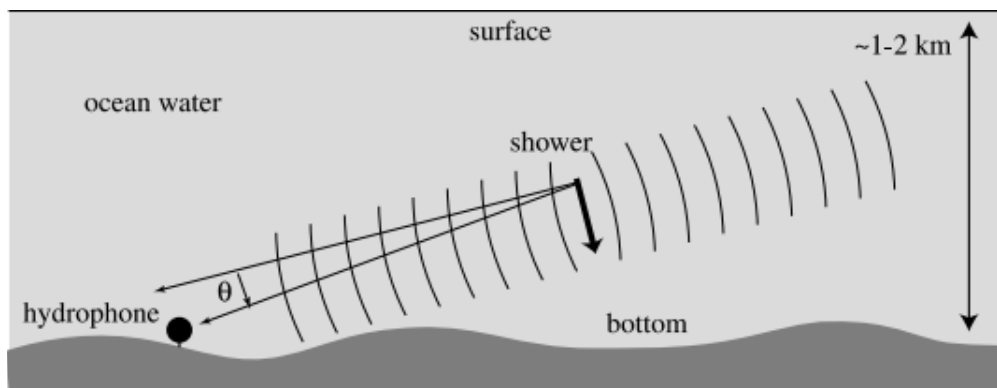
Figure 2.6. Geometrical configuration of a shower in water and of the consequent acoustic pulse produced [59].

2.2   Sound Propagation in Water

As mentioned above, sound propagation depends on environmental parameters and it is also characterized by absorption phenomena.

2.2.1   Sound Velocity

The nominal value of the speed of sound in water is $\approx 1500\ m/s$ and varies with environmental conditions, especially pressure, temperature and salinity. It is important to know the accurate value of velocity to correlate in time signals from different sensors. We can use this simplified version of the Wilson formula [61]:

$$v = 1449 + 4.6T - 0.055T^2 + 0.0003T^3 + (1.39 - 0.012T)(S - 35) + 0.017Z \qquad (2.8)$$

where T [℃] is the water temperature, S [PSU] is the water salinity[5], and Z [m] is the depth. A seasonal variability of these parameters is obviously present, but we cannot take account of these changes. In fact, the sea is a stratified medium and these effects are visible only in the upper layers; in the deepest layers of the sea there is no seasonal variation of environmental parameters (see fig. 2.7), then the main variation of the sound speed is due to the pressure changes with depth.

2.2.2   Sound Attenuation

The amplitude of the sound wave is affected principally by geometric attenuation. Geometric attenuation does not depends on the frequency of the propagating wave and derives from the energy conservation. In fact, as energy is conserved, the intensity decreases proportionally to the inverse of the surface. Considering the simplest case of pressure wave radiating in all directions, the energy spreads over spheres; then the intensity decreases $\propto r^{-2}$ and the signal amplitude decreases r^{-1}.

Moreover, sea water is not an ideal fluid, it is characterized by absorption and scattering phenomena, that overall determine the sound attenuation.

Absorption is related to shear viscosity mechanisms. Scattering is due to the inhomogeneities existing in water, like bubbles, plankton or particulate matter.

---

[5]PSU stands for Practical Salinity Unit, the official scale for salinity. Standard value of salinity in sea water is 35, and in fresh water is around 0.
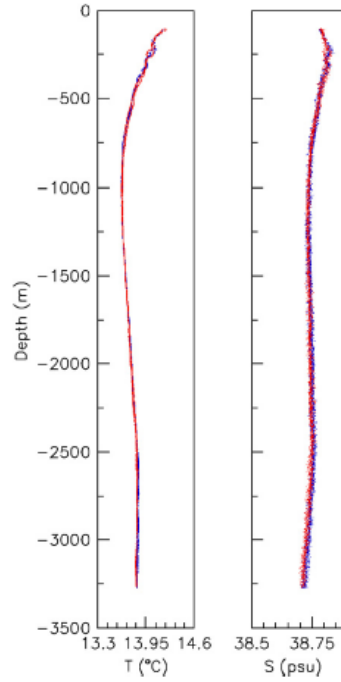
Figure 2.7. Temperature and salinity as a function of depth measured by the NEMO Collaboration in the KM4 site, in the Ionian Sea [62].

The variation of the signal intensity is described by the following exponential law:

$$I = I_0 \, e^{-cR} \tag{2.9}$$

where I is the intensity of the acoustic wave, R is the distance from the source and c is the attenuation coefficient. The attenuation can be expressed also in $\left[\frac{dB}{km}\right]$ and represent how much the sound is reduced compared to the initial value. The attenuation is function of the frequency and of environmental parameters and, in a very simplified model, $\alpha \propto f^2$ (see fig. 2.8).

Following the Learned's solution [63], we can introduce the attenuation in eq. (2.5), that becomes

$$\nabla^2 \left(p(\vec{r}, t) - \frac{1}{\omega_0} \frac{\partial \, p}{\partial \, t} \right) - \frac{1}{v^2} \frac{\partial^2 p(\vec{r}, t)}{\partial \, t^2} = -\frac{\beta}{C_p} \frac{\partial^2 q(\vec{r}, t)}{\partial \, t^2} \tag{2.10}$$

with $\omega_0 \approx 10^{12} \, Hz$ is the characteristic attenuation frequency.

A useful approach to the solution of the wave equation foresees the use of its Fourier transform.
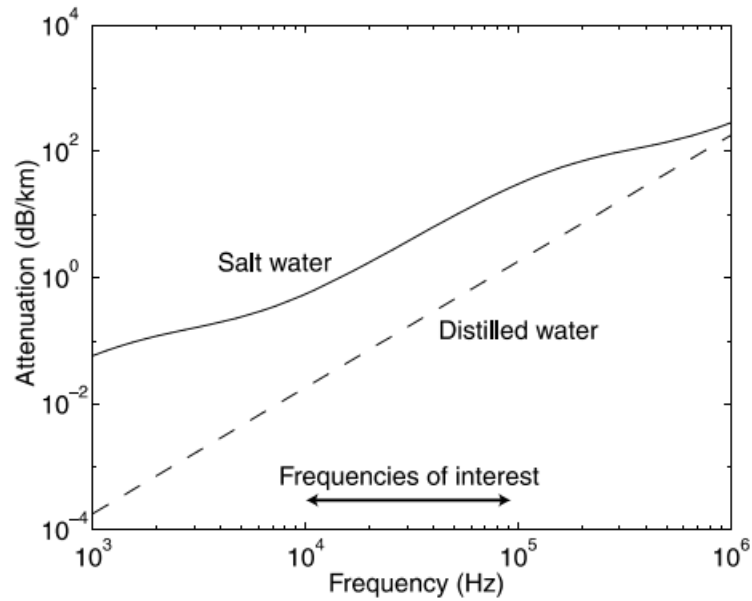
Figure 2.8. Sound attenuation coefficient at 25 ℃, in the sea and in distilled water, as a function of frequency [59].

2.2.3 Acoustic Signal

As already mentioned above, the signal generated by neutrino interaction is "pancake-shaped". In the pressure pulse, shown in fig. 2.9, is visible the almost symmetric bipolar shape, in the time domain.
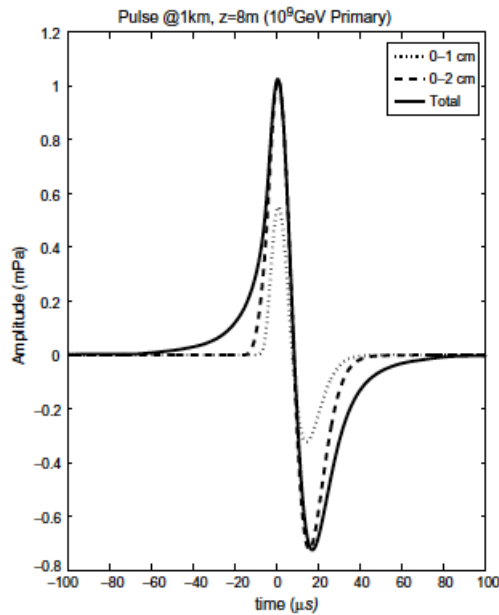
Figure 2.9. Acoustic signal in sea water at a distance of $1 \ km$ from the axis, from a shower with $10^9 \ GeV$ primary energy. The curves represent the signals computed from the deposited energies within cores of different radius [60].

Acoustic pulses in sea water with the relative power spectrum, for three different parametrisations, are shown in fig. 2.10. The results are similar but not coincident and this fact is due to the different calculation methods used.
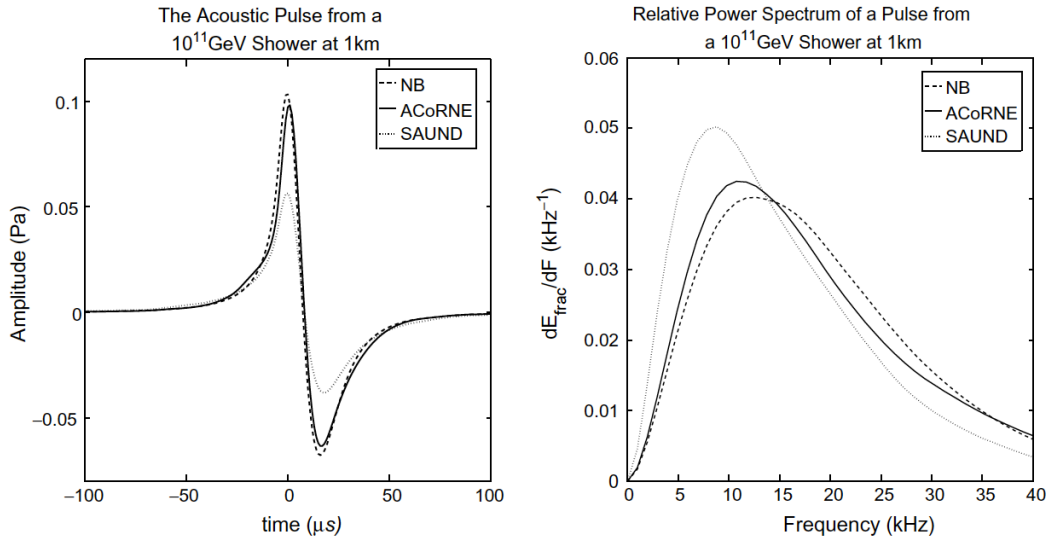
Figure 2.10. Acoustic pulses (on the left panel) and its power spectrum (on the right panel), from a 10^{11} GeV shower, generated from different parametrisations, 1 km distant from an acoustic detector [60].

2.3   Detection Technique

The acoustic detection is based on the usage of hydrophones; they are underwater pressure sensors that convert the pressure variation in voltage signal, using the piezoelectric effect. These sensors employ piezoelectric materials (crystals or ceramics) that, submitted to a mechanical stress, show electric charge due to their deformation. In fig. 2.11 is displayed the hydrophone used in this thesis.

Figure 2.11. Hydrophone RESON TC4034. Image from http://www.teledynemarine.com/reson-tc-4034.

As visible in fig. 2.12 the shape of the acoustic signal depends on the detector position, from whom the importance of the calibration and the placement of the hydrophone.
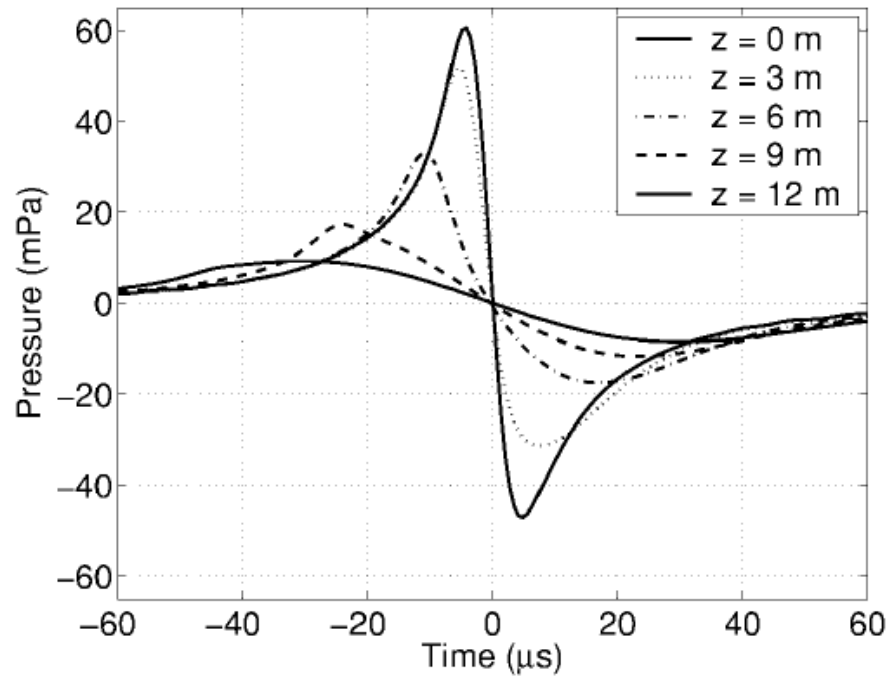
Figure 2.12. Simulated acoustic pressure signals due to hadronic shower of 10^{20} eV, for different longitudinal distances from the shower maximum [46].

Chapter 3

Characterization of the Parametric Acoustic Source

As we have seen in the previous chapter we do expect, as the result of the interaction of a high energy neutrino in sea water, a bipolar signal in the time domain and a quite well defined geometrical definition of the pressure wave propagation. These issues can be used to select neutrino signals out of the most intense natural background. Once a detector will be placed in water it will be very useful to have the possibility to simulate acoustic signals similar to the ones expected by neutrino interactions. For such a reason a dedicated device has been developed and realized. This device, based on a set of piezoelectric cells used as voltage-to-sound transducers, allows to generate a large variety of signals in water according to a well defined parametrization of the amplitudes and the relative phases of the input (voltage) signals. We will define this device *parametric acoustic source*. In order to calibrate and fully understand the behaviour of this source, a sequence of tests in water have been performed.

In this chapter the apparatus, the data acquisition and the relative analysis will be described. The data acquisition was performed in August 2017, at the Institute of Acoustics and Sensors "Orso Mario Corbino" (IDASC) of the National Researches Council (CNR), in the research area of Roma-Tor Vergata [1].

3.1   The Instrumentation

The acoustic source is made by eight piezoelectric ceramic transducers, with their axis separated by a distance of $4\,cm$ (fig. 3.1). The ceramics convert electric signals in pressure signals that propagate in the surrounding water volume, as described in Chapter 2.

The source was immersed in a pool of dimensions $6\,m \times 5.5\,m \times 4\,m$, at $228\,cm$ of depth, as visible in fig. 3.2. It was supported by a pole, that can rotate clockwise and anticlockwise around its axis.

Figure 3.1. Acoustic source consisting of eight transducers.
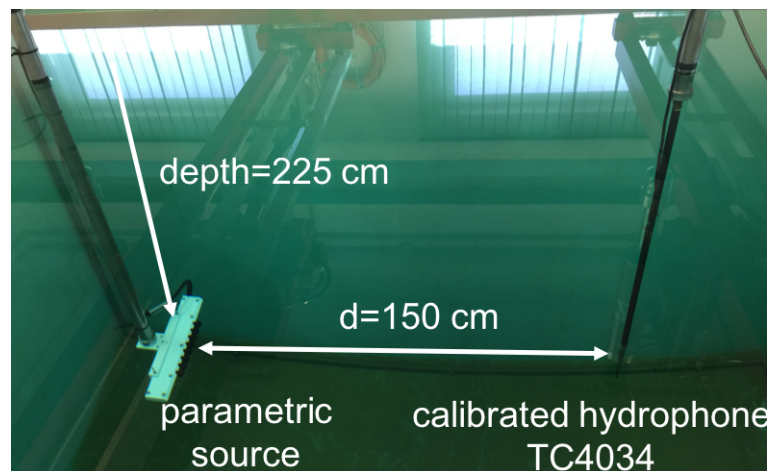
Figure 3.2. Underwater apparatus into the pool of the laboratory.

The acoustic signal generated by the parametric source was then acquired by a calibrated hydrophone: a RESON TC4034 (see fig. 2.11) located at the same depth of the ceramics and aligned with the centre of the source. The distance between the source and the hydrophone was initially $200\,cm$, then shifted at $150\,cm$ for the whole experiment. A schematic representation is shown in fig. 3.3, where there are the lateral view and the overhead view, respectively on the left side and on the right side.
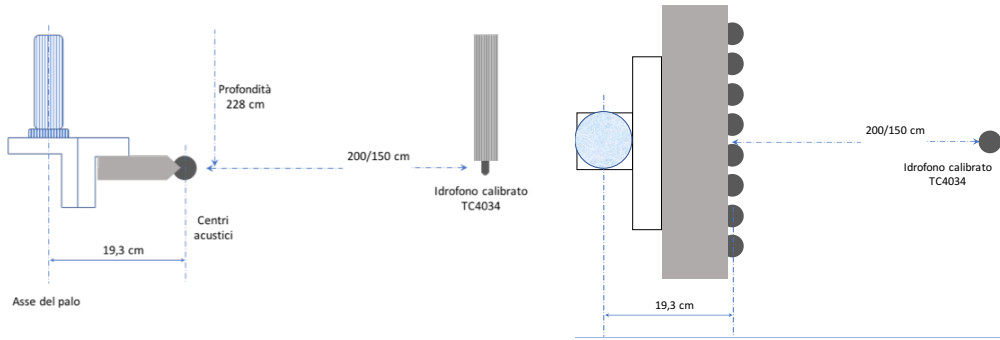
Figure 3.3. Depiction of the apparatus from side and from above.
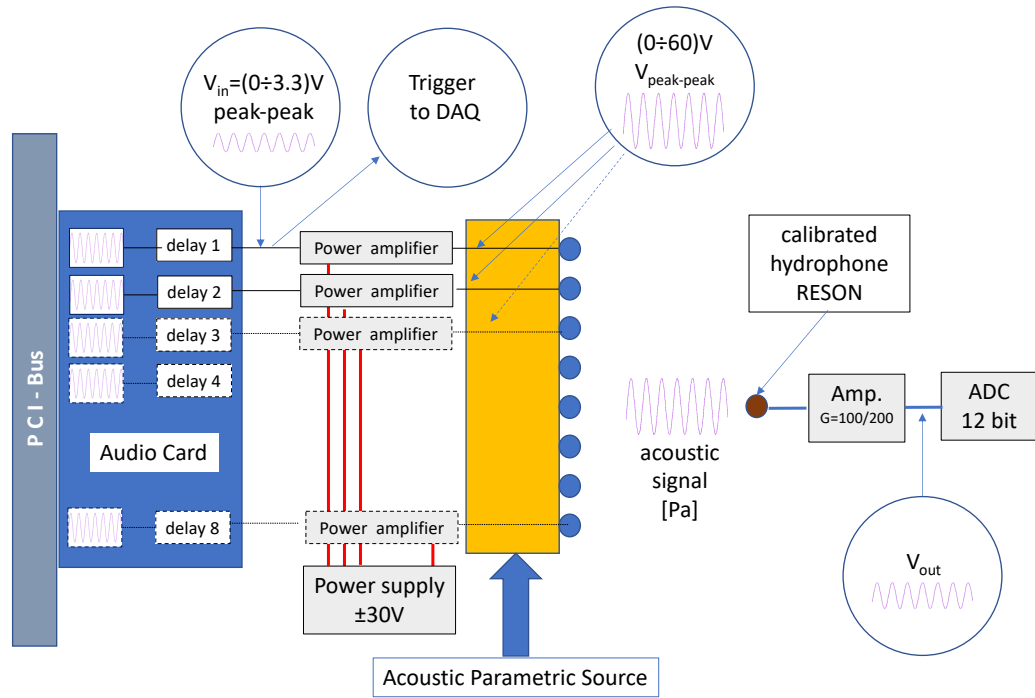
Figure 3.4. Apparatus scheme in terms of electronics.

3.1.1   Apparatus Setup

The fig. 3.4 shows the schematics of the apparatus used to characterize the parametric source. For each one of the eight piezoelectric transducers we generated a sinusoidal input signal with peak-to-peak amplitude $0\,V < V_{peak-to-peak} < 60\,V$. The apparatus allows to change the relative phases between the signals used to stimulate the piezoelectric. The duration of the sinusoidal input signal was fixed to $10\,ms$. The piezoelectric input signal amplitude was obtained by amplifying the output of a commercial signal generator, the *audio card*; this card can generate a large variety of signals such as, for example, sinusoidal, triangular, step, and delta functions. The audio card was limited in frequency at $96\,kHz$

and this means that the Nyquist frequency was $48\,kHz$. Also for this reason, we decided the frequency interval to examine.

The acoustic signal transmitted in water was then the result of the interference between the eight individual ones. It was acquired by using a calibrated hydrophone (RESON TC4034) that transforms the acoustic signal into an electric one. This signal, after an amplification, is digitized by using a $12\,bit\ Analog\ to\ Digital\ Converter$ (ADC). The gain of the amplifier, $100\,dB$ or $200\,dB$, was selected in order to use properly the dynamics $(0 - 4\,V)$. The ADC conversion was started only when the signal produced by the audio card was bigger than the threshold level $V_{th} = 0.5\,V$. The ADC sampling frequency was fixed to $1\,Msample$, such that for each acquisition we collected about 10000 samples. Due to the trigger conditions, all series of 10000 samples were "in phase" so, in order to reduce the experimental fluctuation and the amount of data in output we decided to store, as n-th sample, the average over the n-th sample of 30 consecutive signals.

The first measurements have been performed in order to study the ceramics behaviour for different frequencies (from $10\,kHz$ to $40\,kHz$). The acquisition procedure was based on the software *LabVIEW*; a screenshot of the interface is reported in fig. 3.5, where the upper panel is the input signal and the lower is the measured one, and the settings are also visible.
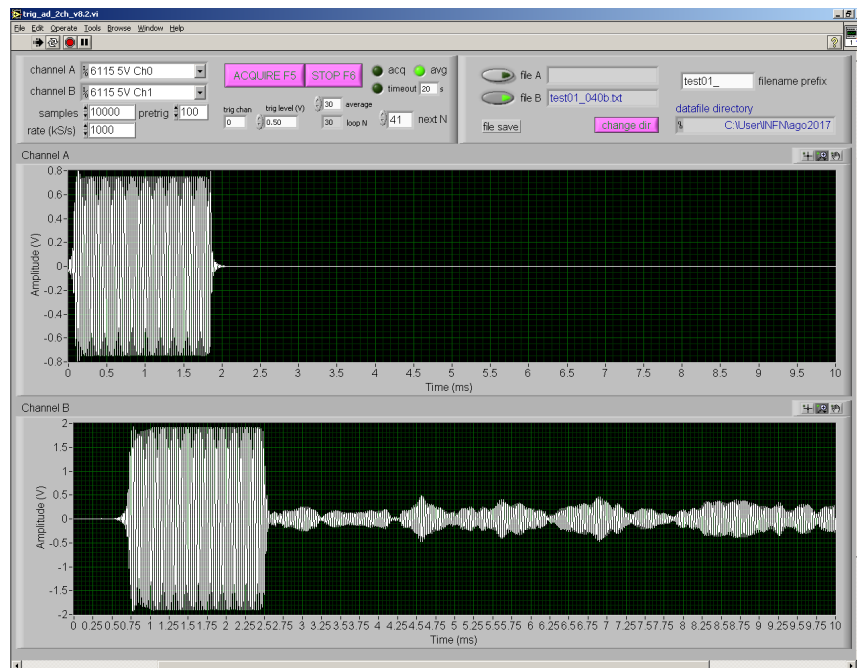
Figure 3.5. Screenshot of the acquisition program *LabVIEW*.

3.2   Data Acquisition and Analysis

In this section the data acquisition with the relative analysis are described. Measures concern the characterization of the single ceramics and the study of the directivity of the source. The data analysis is performed by using the programming language *MATLAB* [2].

Environmental parameters that can affect the measurements (room and water temperature) were continuously monitored and recorded.

3.2.1   Characterization in Frequency

The first series of data acquired had the purpose of characterizing every ceramic as a function of the frequency.

In the first sequence of measurements the amplifier gain was $G = 200\,dB$. The distance between the hydrophone and the source was initially set to $200\,cm$, but in order to reduce the background due to the reflections, the distance was reduced to $150\,cm$ for the rest of the experiment. Every ceramic was individually excited by using sinusoidal input signals with frequencies between $10\,kHz$ and $40\,kHz$, with steps of $2.5\,kHz$. The sampled signal, for a $22.5\,kHz$ sinusoidal input signal, is displayed in fig. 3.6; only a part of the signal appears less affected by the background and non linear effects, approximately between the $1500th$ sample and the $2400th$ sample. This part of the signal, well represented by a sinusoidal function, will be analysed.

We have to consider the regular part of the signal and neglect the initial and the final parts. The selected range is the same for the whole data, and goes from $1.5\,ms$ to $2.4\,ms$ of the sampling time. The data included in this interval shall be represented by a sinusoidal function

$$y = a\sin[2\pi f(t - t_0) + \eta] \tag{3.1}$$

where a, f, η are the unknown factors and they are respectively the amplitude, the frequency and the phase of the signal. The quantity t_0 is the propagation time, intended as the time needed for the signal to arrive on the hydrophone; this initial transition is visible in fig. 3.6. It can be estimated calculating the envelope of our data, by the use of MATLAB. After obtaining the envelope curves for several series of data, we have gotten the propagation time $t_0 = 1.13 \times 10^{-3}\,s$, i.e. the $1300th$ sample, as the abscissa corresponding to the half maximum of the envelope. An example of sinusoidal interpolation, on the data included in the range mentioned above, is provided by fig. 3.7, where the experimental data

are the blue dots with the related error bars, and the red line is the curved produced by the interpolation. The uncertainty is calculated as a thousandth of the full-scale, divided the square root of the sampling number.
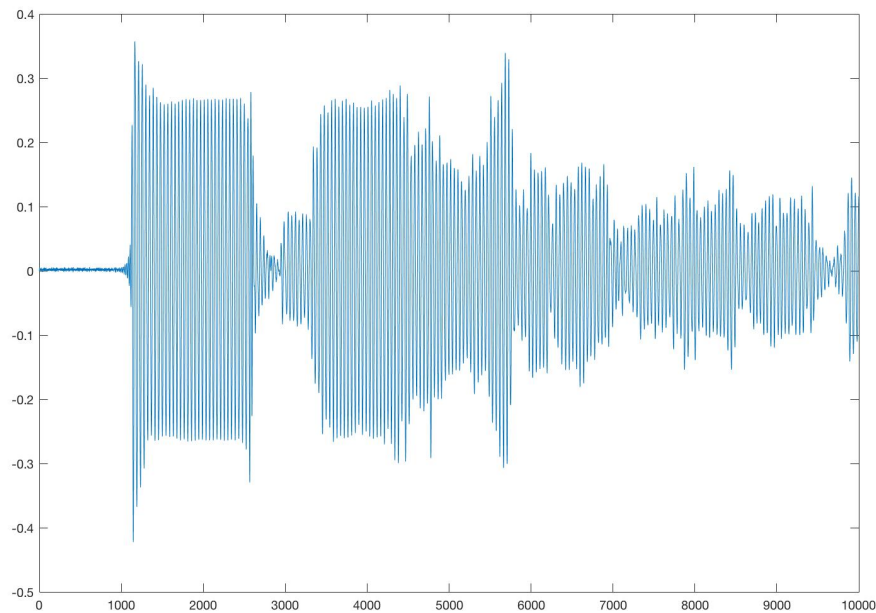
Figure 3.6. Example of signal acquired for the fourth ceramic at frequency $22.5\,kHz$.
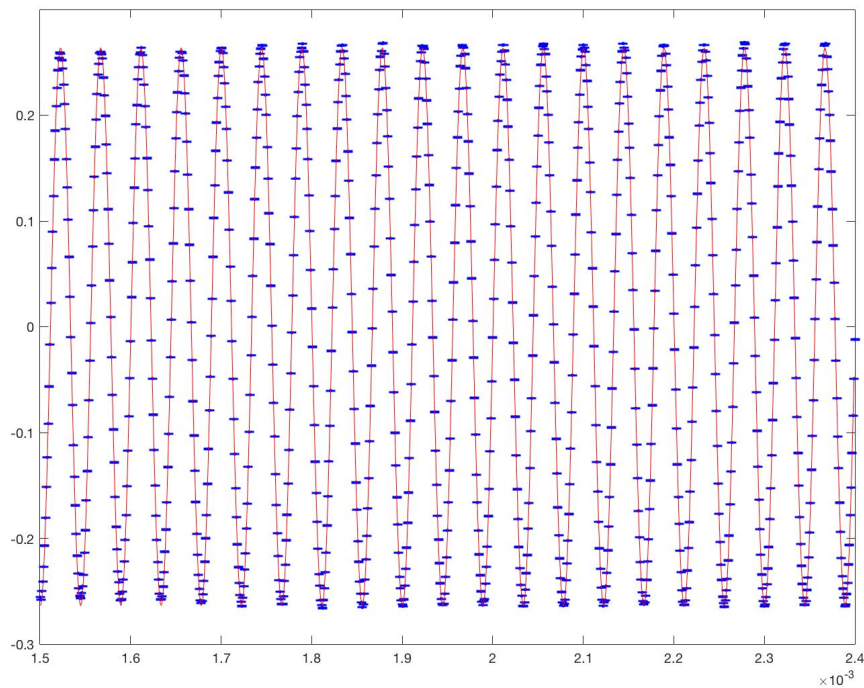
Figure 3.7. Example of interpolation, with a sinusoidal function, on the data selected, for the fourth ceramic at frequency $22.5\,kHz$.

Initially, we characterized each ceramic by stimulating it singularly with a sinusoidal input signal, with frequencies spanning from $10\,kHz$ to $40\,kHz$. The results is summarized in fig. 3.8, where are reported the amplitudes as a function of the frequency, for every ceramic.
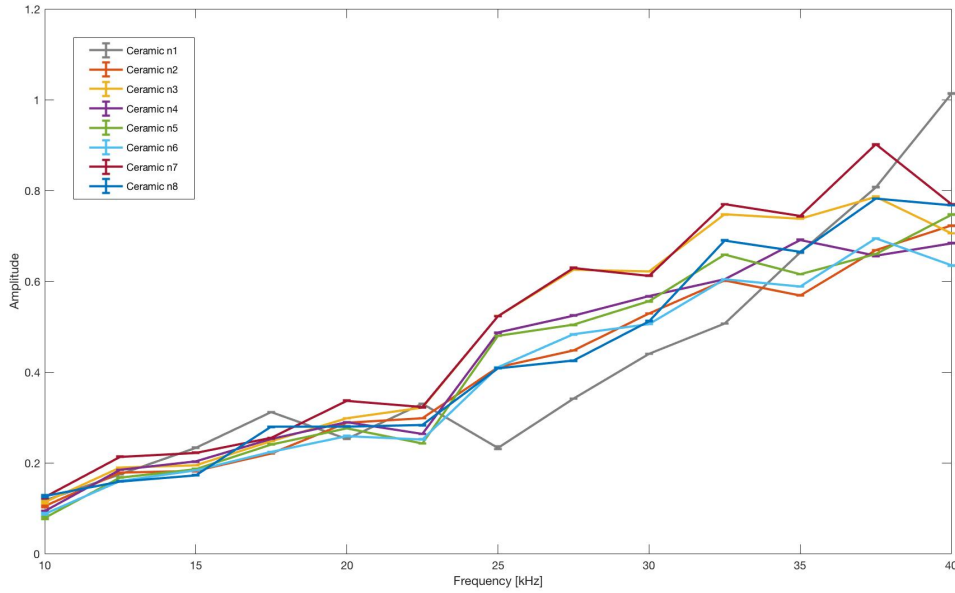
Figure 3.8. Amplitude of the signal with the related uncertainties, for every ceramic, as a function of frequency.

From this data the values of the phases can be obtained, for each ceramic, as function of the frequency. We decided to characterize the phases of the different ceramics by comparing the phase of each of them with the phase of the fourth ceramic, taken as reference because of its central position. In the following plots (fig. 3.9 and fig. 3.10) the phase differences are plotted respectively as a function of the number of the ceramic and as a function of the frequency.

These differences are the sum of two component: the phase difference attributable to the different acoustic path and the phase difference due to the feedback of the specific ceramic. The first component can be evaluated considering the geometrical pattern of the apparatus; in fact, the real distance between each ceramic and the hydrophone is not exactly $150\,cm$. We have to consider the position of each ceramic along the source and compute its real distance with the detector. In this calculations the delays related to the different emission time of the ceramics has been taken into account, obtaining the effective distance between each ceramic and the hydrophone.
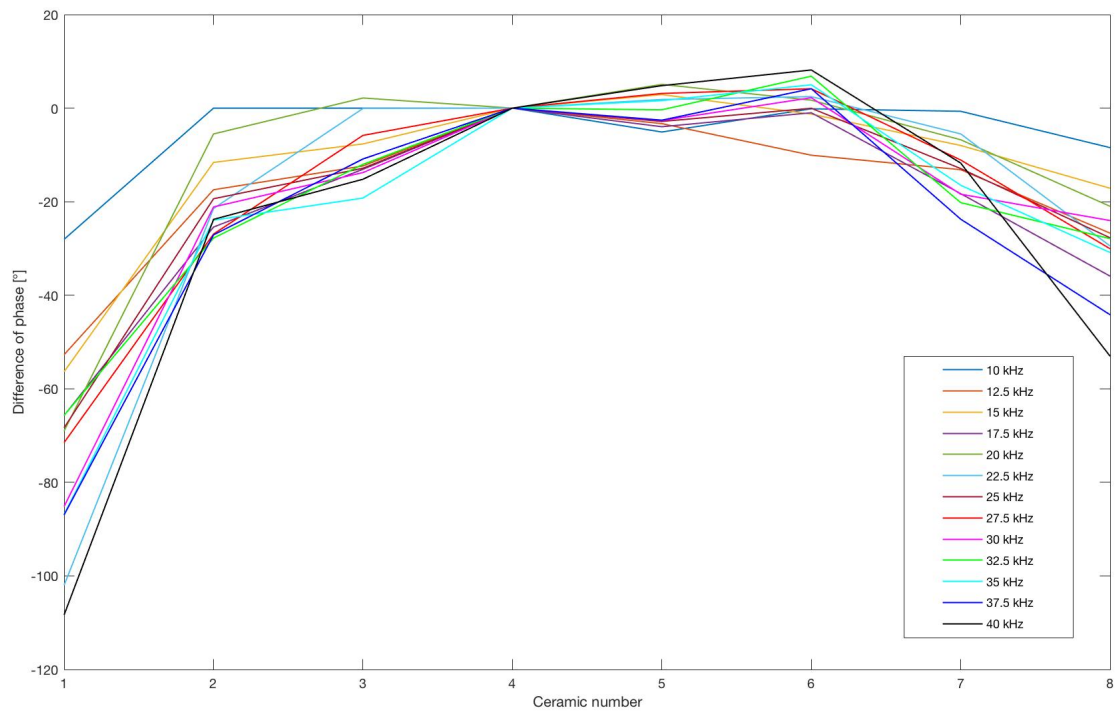
Figure 3.9. Difference in phase between every ceramic and the fourth ceramic, for various frequencies, as a function of the ceramic.
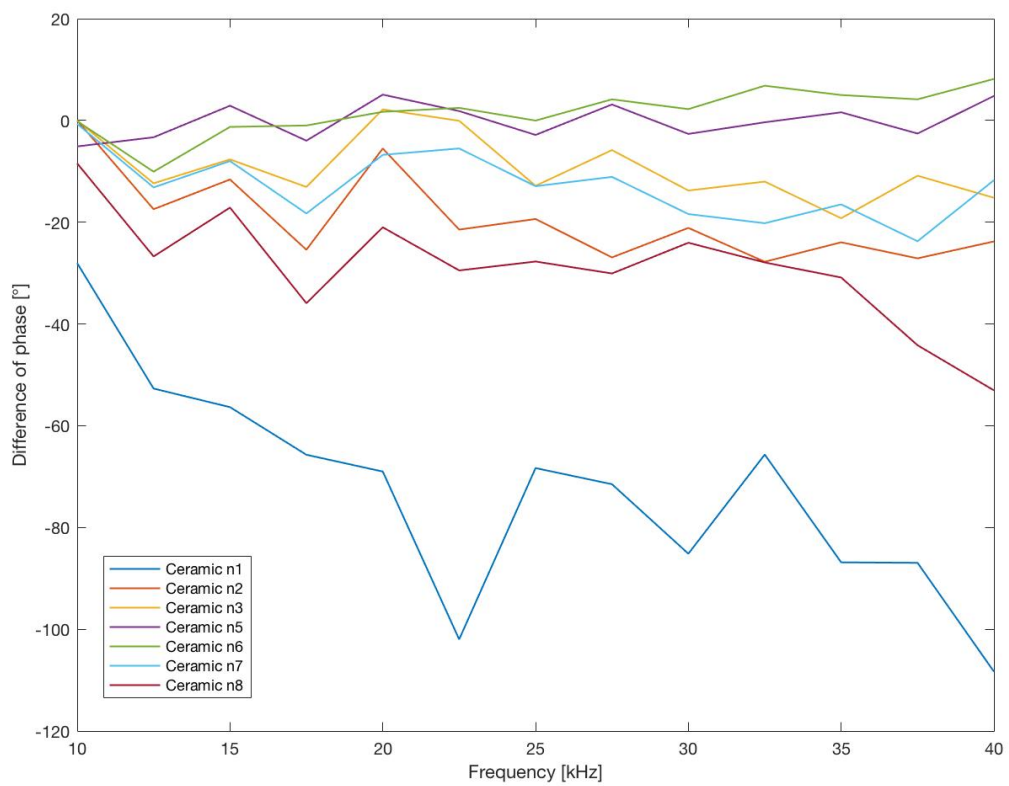
Figure 3.10. Difference in phase calculated for every ceramic and the fourth ceramic, as a function of the frequency.

The delays included are those listed in table 3.2, converted from time to distance, and added to the nominal distance. The nominal and the effective distance are reported in table 3.1.

Ceramic number	Nominal distance [cm]	Effective distance [cm]
1	150.65	148.86
2	150.33	149.68
3	150.12	149.87
4	150.01	150.01
5	150.01	150.18
6	150.12	150.27
7	150.33	150.01
8	150.65	149.67

Table 3.1. Nominal distances and effective distances calculated between every ceramic and the hydrophone. The delays in the emission time of the ceramics have been taken into account to calculate the effective distances.

We want then evaluate the theoretical phase difference between the ceramics and the fourth one, for all the frequency. In order to perform this calculation, taking also into account the real distances emitter-receiver, we had to evaluate the sound speed in the water pool. We calculated the sound propagation velocity in water using eq. (2.8), where the temperature is that one measured at the beginning of the measurement activities and the salinity has been neglected.

Then for each frequency the acoustic path from each ceramic to the hydrophone, in units of wavelength, has been computed. This calculation allowed us to evaluate the geometrical correction that we have to apply to the measured values of the phase differences, in order to extract the real different response in phase of the several ceramics. These corrections are shown fig. 3.11.

Taking into account this correction, we can then evaluate how the response in phase of each ceramic, relative to the fourth one, changes as a function of the frequency. These behaviours are shown in fig. 3.12.

In all these figures that show the behaviour of the phases, the uncertainties are not reported because of their small values.
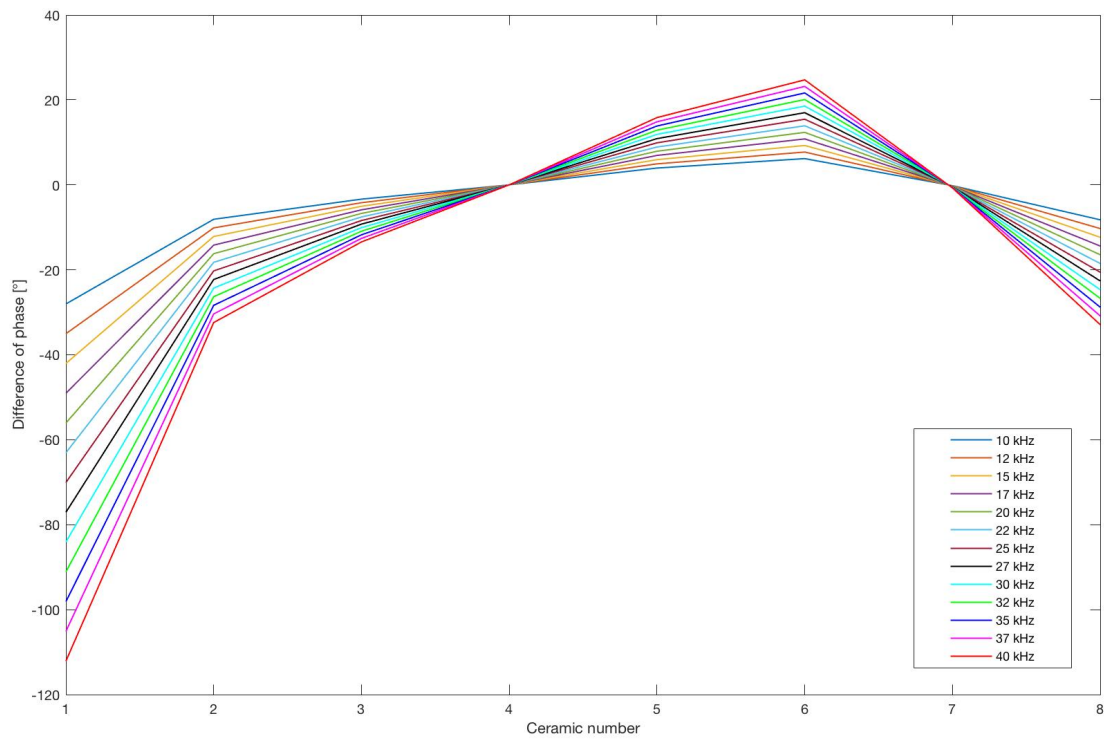
Figure 3.11. Phase differences, due to the acoustic path, in function of the ceramic number, calculated between each ceramic and the fourth one.
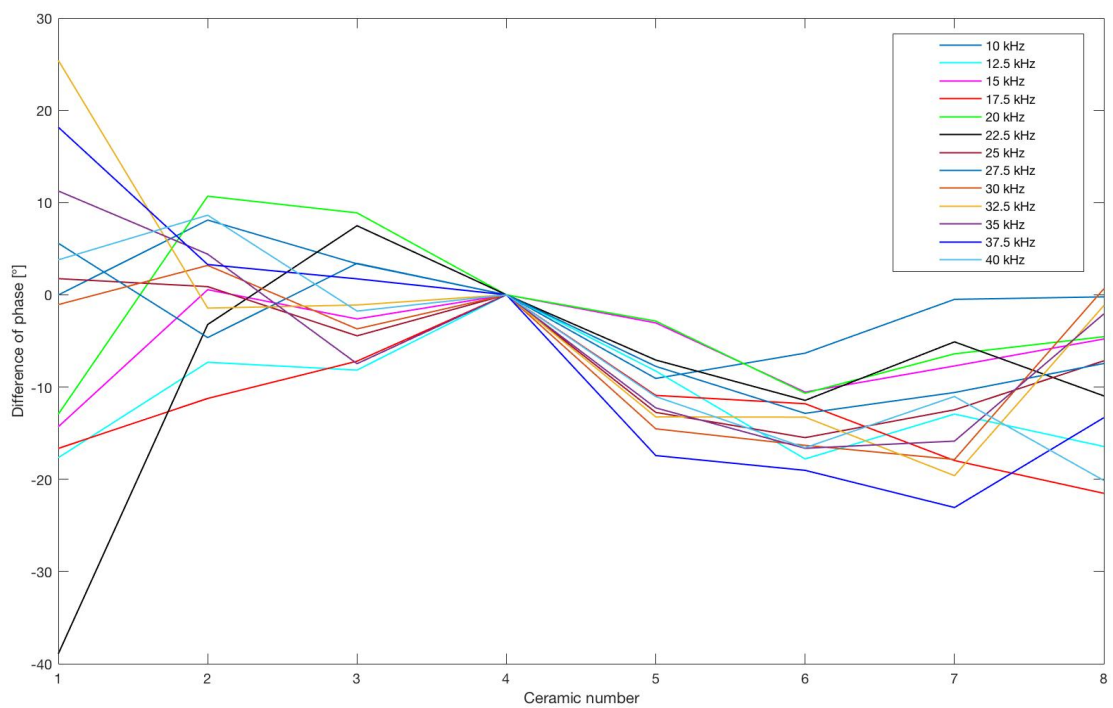
Figure 3.12. Phase differences due only to the feedback of the ceramics, in function of the ceramic number, calculated between each ceramic and the fourth one.

3.2.2 Study of the Directivity of the Source

The next set of measurement concerns the study of the directivity of the source. This study is possible analysing data collected changing the position of the parametric source, namely by rotating the pole around its axis.

The angle ϕ is defined into the plane where the ceramics lay, as the angle between the line orthogonal to the source and the line that links the source and the hydrophone (see fig. 3.13). The angle ϕ is in the range of $-90°$ to $90°$.
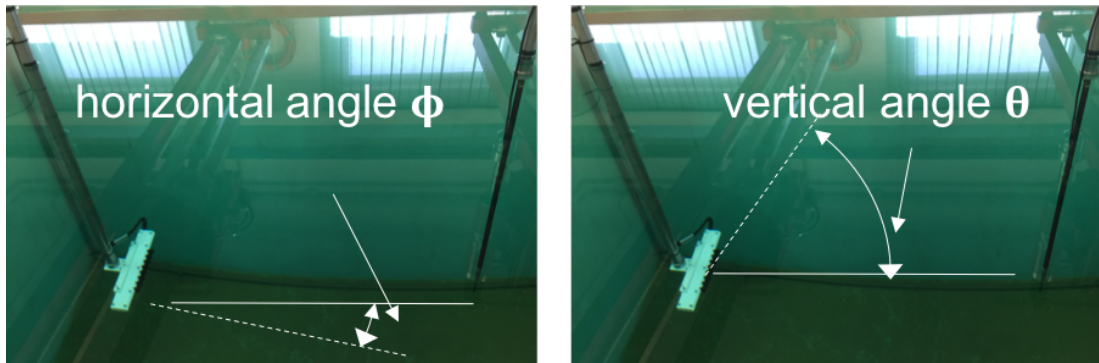
Figure 3.13. Horizontal and vertical angles, respectively ϕ and θ, between the source and the hydrophone.

In this sequence of measures the first ceramic (that is the nearest to the entry point of the cables) is excluded, because of its irregular response in frequency (see fig. 3.10). Now the frequencies considered are 15, 20, 25, 35, 40 kHz, and the angle varies with steps of 15°. After having reduced the averaging procedure to 20 samples, instead of 30, being sure that the resulting fluctuations are not affecting the results, it was decided to vary the angle ϕ from $-15°$ to 15°, with 1° steps.

Even in this case we must consider the geometrical layout of the apparatus. We have defined the angle ϕ above, as the angle between the line orthogonal to the source and the line that links the source and the hydrophone. Actually, the real angle between each ceramic and the receiver hydrophone does not correspond to the nominal one, so it is necessary to estimate the right angle using geometrical calculations.

The amplitude of the signal, for every angle, is extracted from the interpolation of the regular part of the taken data as explained in section 3.2.1. The amplitudes and the angles (nominal and real) are reported in tables A.1 to A.6. These amplitudes are plotted as a function of the real angle, for the several frequencies in figs. 3.14 to 3.19. In all these figures the error on the amplitude is reported but not visible. From these figures is visible,

especially for $15\,kHz$ or $35\,kHz$, the beampatterns with the main lobe and the side lobes. Undoubtedly, they could be more visible if we had more points.

To complete this analysis we have compared these data to the theoretical beampatterns, calculated at different frequencies varying the emission angle in the range $[-90°; 90°]$. The MATLAB code used is enclosed in appendix B. The amplitude is computed as the sum of every amplitude due to each ceramic arriving on the hydrophone. The beampatterns are shown in figs. 3.20 to 3.25 (solid blue line) and compared to the data (red crosses), where the amplitude is expressed in $[dB]$. Is clearly visible the presence of many theoretical side lobes, not visible in our data. In fact, the position of the secondary lobes is influenced by many factors, as our apparatus and instruments, and cannot be accurate. What is important is the position and the width of the main lobe, that seem to be in agreement with the theoretical beampatterns.
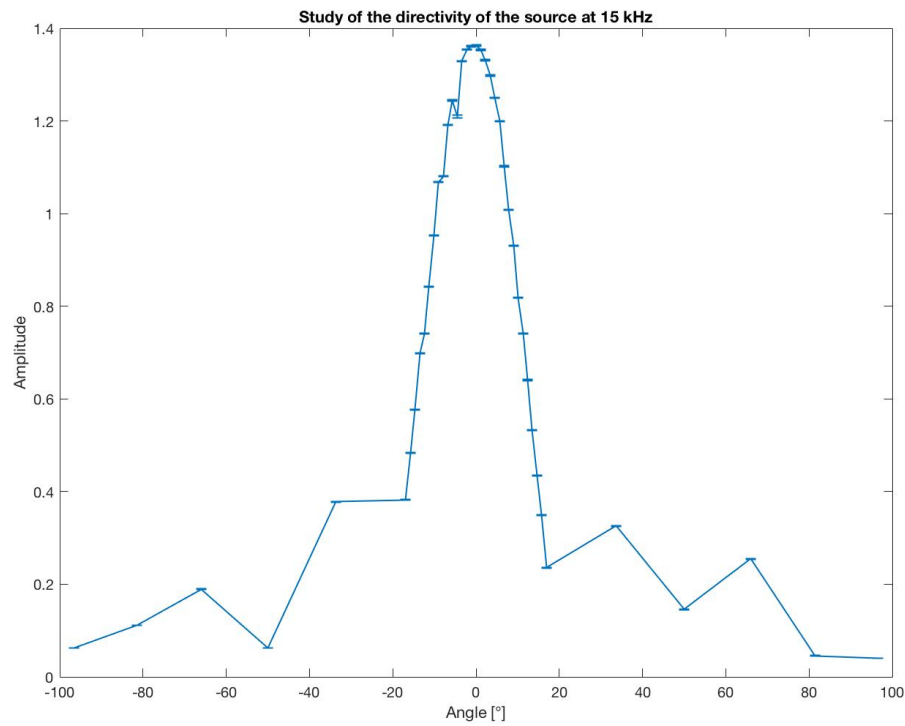
Figure 3.14. Amplitude, with related uncertainties, as a function of the right angle of emission, at $15\,kHz$.
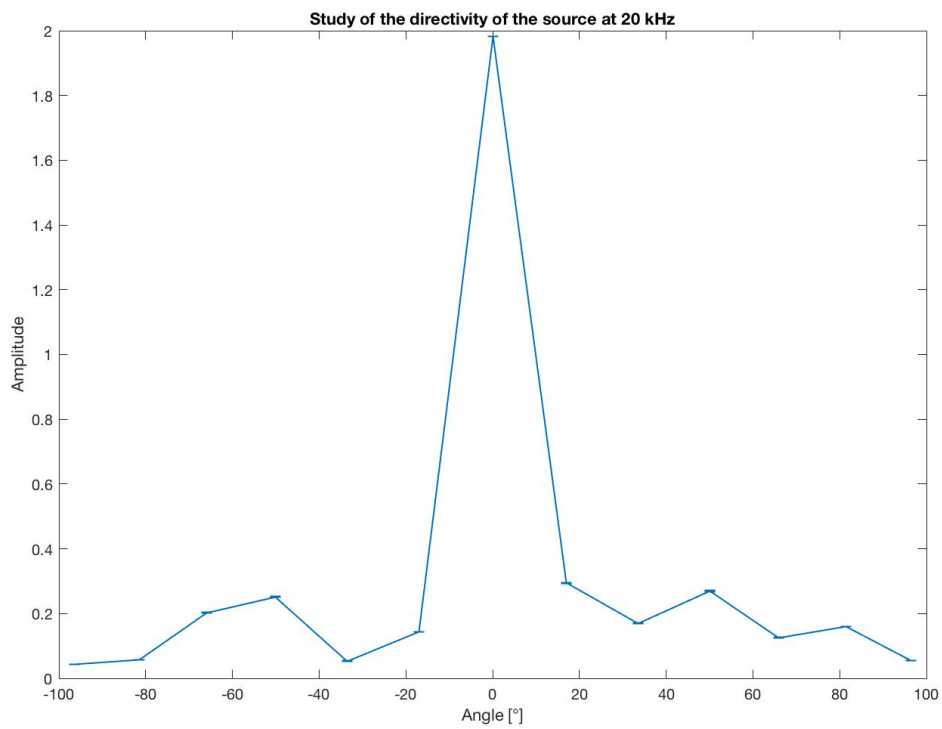
Figure 3.15. Amplitude, with related uncertainties, as a function of the right angle of emission, at $20\,kHz$.
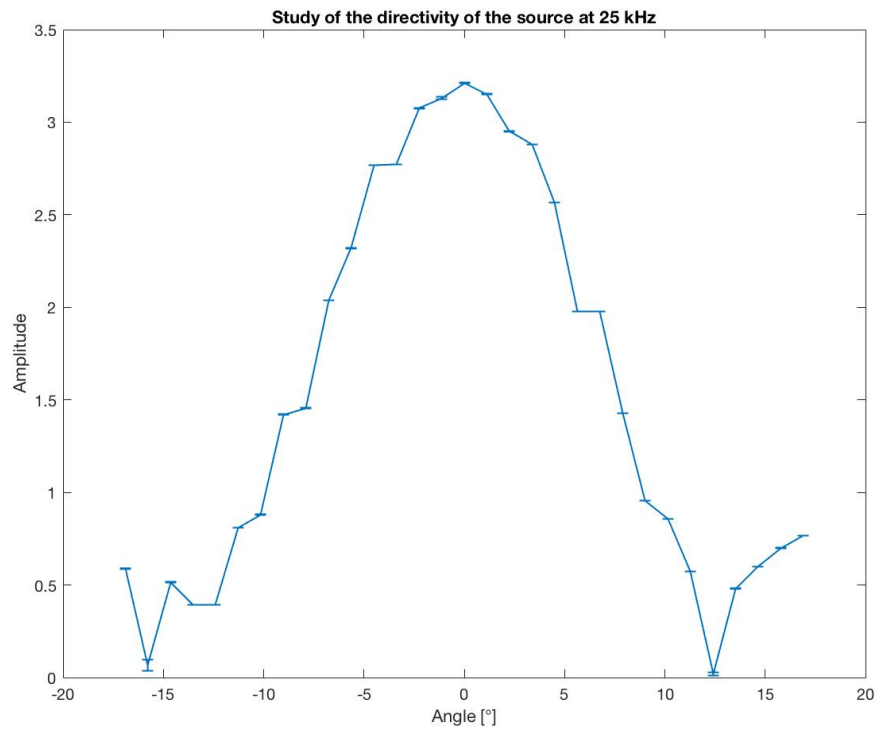
Figure 3.16. Amplitude, with related uncertainties, as a function of the right angle of emission, at $25\,kHz$.
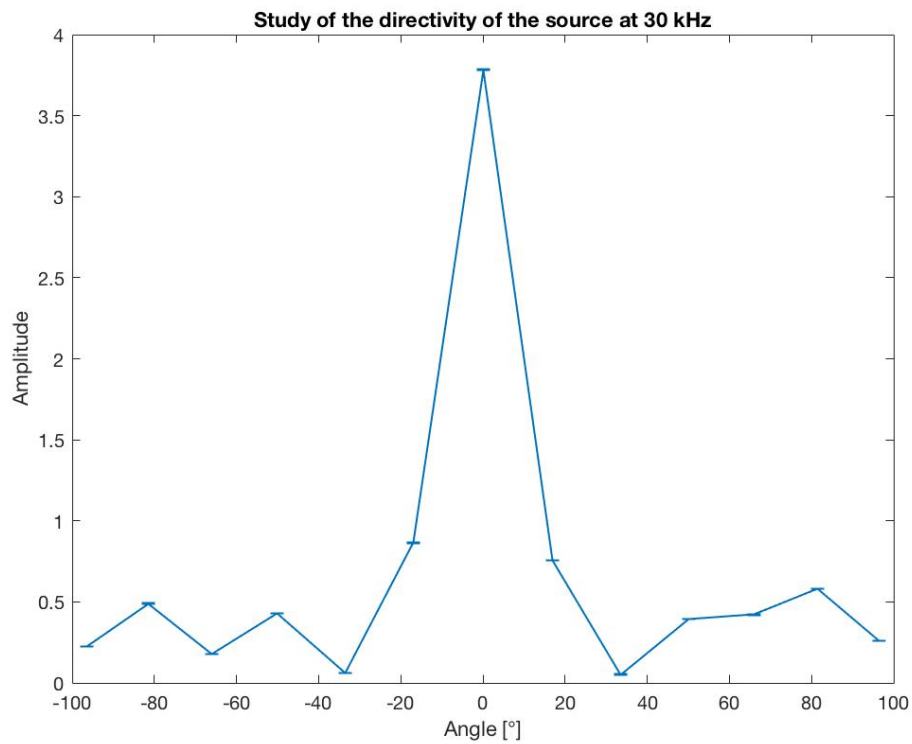
Figure 3.17. Amplitude, with related uncertainties, as a function of the right angle of emission, at $30\,kHz$.
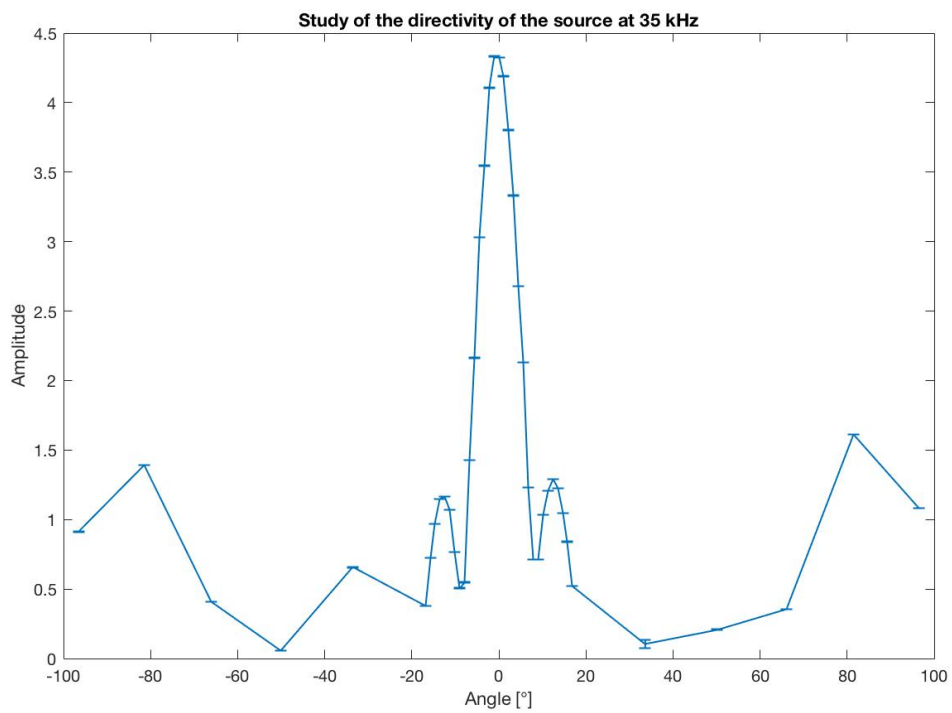
Figure 3.18. Amplitude, with related uncertainties, as a function of the right angle of emission, at $35\,kHz$.
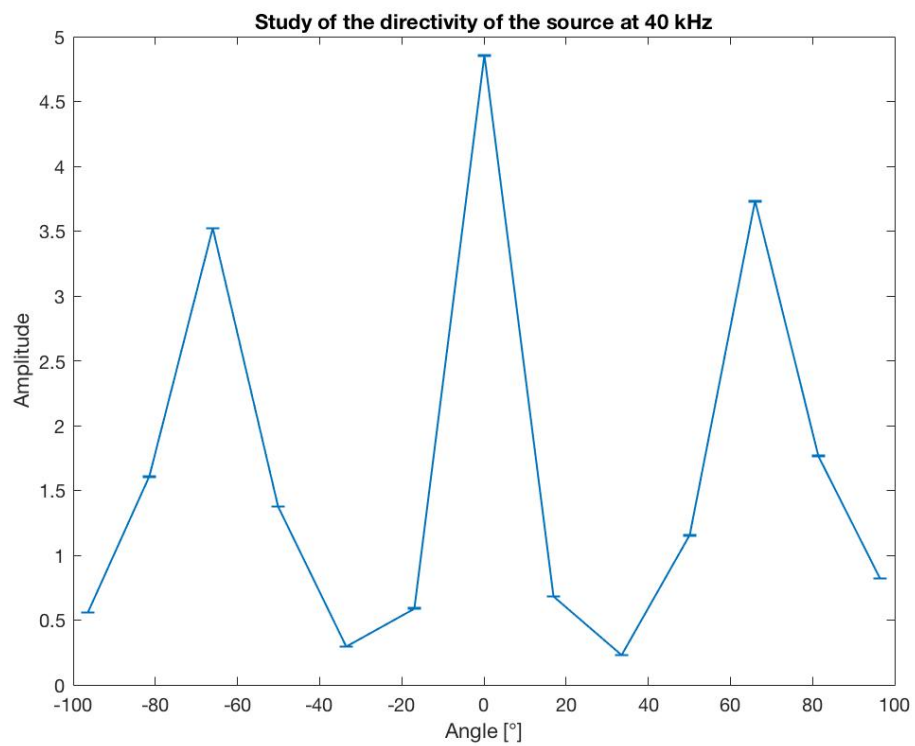
Figure 3.19. Amplitude, with related uncertainties, as a function of the right angle of emission, at $40\,kHz$.
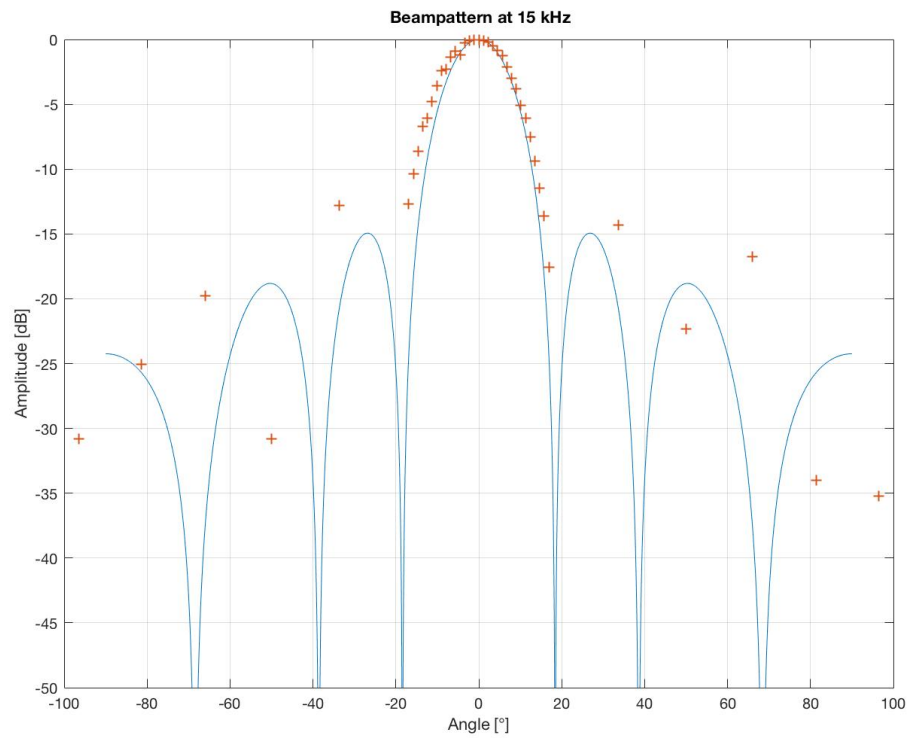
Figure 3.20. Beampattern expressed in $[dB]$, as a function of the angle, at $15\,kHz$.
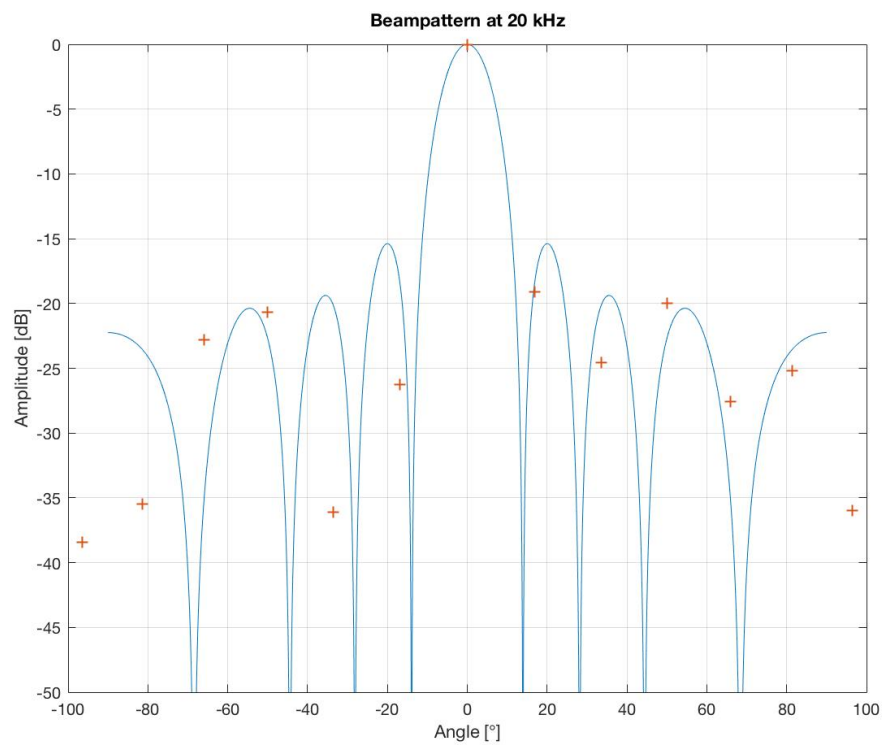
Figure 3.21. Beampattern expressed in $[dB]$, as a function of the angle, at $20\,kHz$.
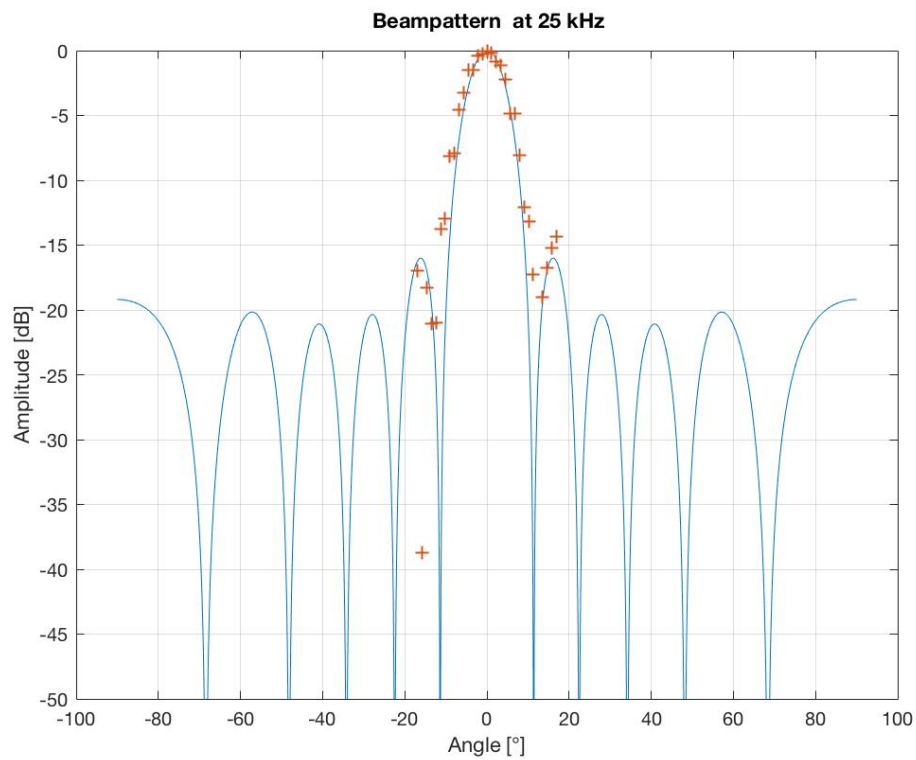
Figure 3.22. Beampattern expressed in $[dB]$, as a function of the angle, at $25 \, kHz$.
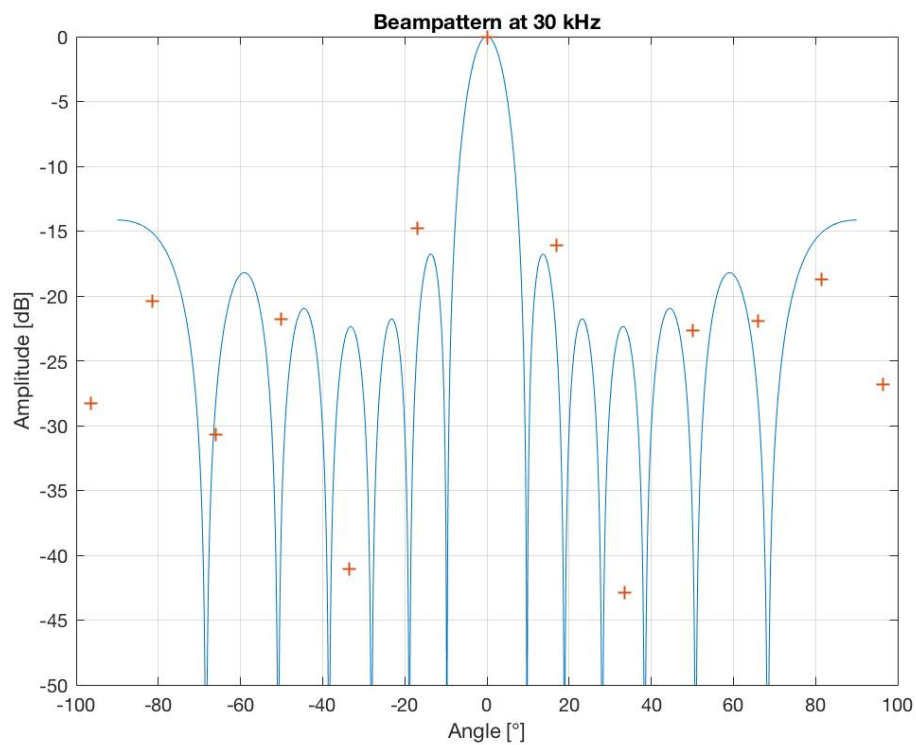
Figure 3.23. Beampattern expressed in $[dB]$, as a function of the angle, at $30 \, kHz$.
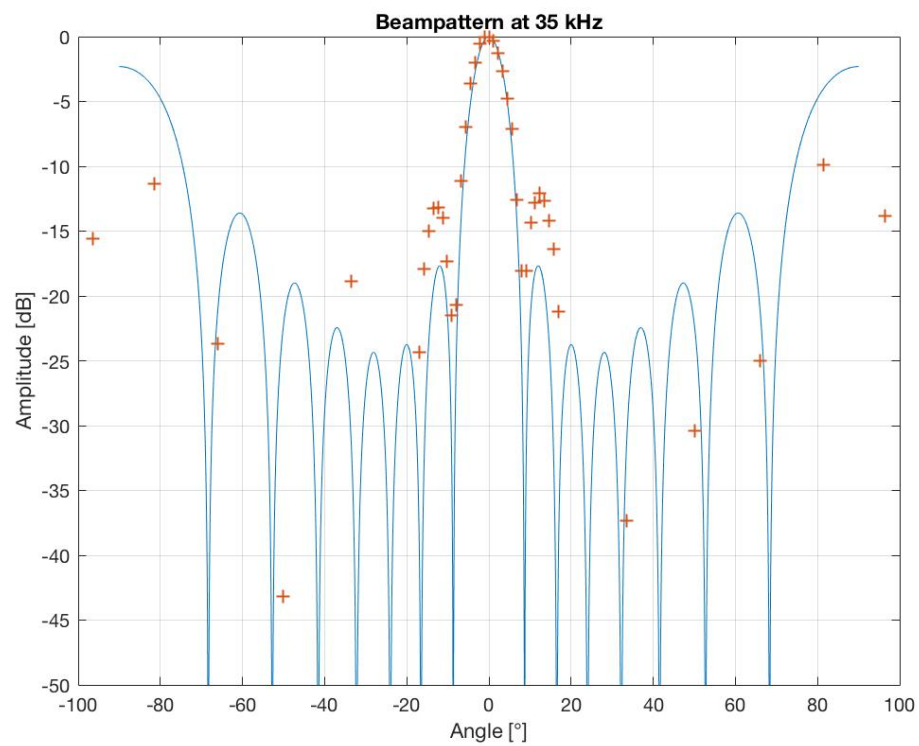
Figure 3.24. Beampattern expressed in $[dB]$, as a function of the angle, at $35\,kHz$.
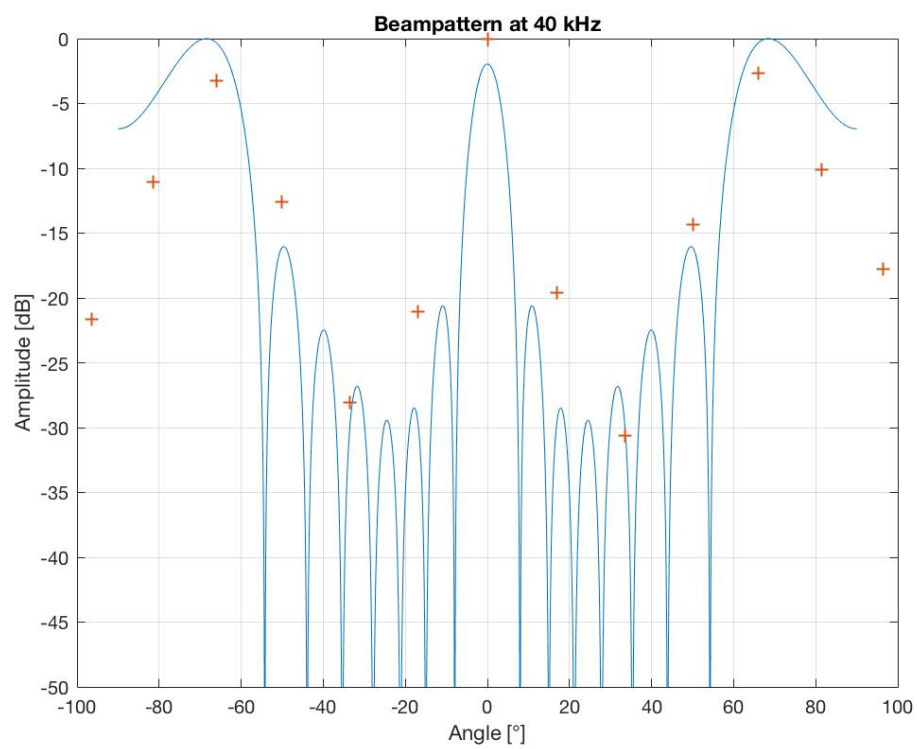
Figure 3.25. Beampattern expressed in $[dB]$, as a function of the angle, at $40\,kHz$.

3.2.3   Angular Beamsteering Analysis

The following session of measures concerns the *angular beamsteering*, that is the possibility of changing the direction of the acoustic signal by sending in input of the ceramics a well defined pattern of signals. The central direction of the acoustic signal can be changed by setting, for each ceramic, a proper delay calculated in order to have the superposition of all the acoustic signals, with the same phase, at a chosen position. Again the input to the ceramics were sinusoidal signals, all with the same frequency. The amplifier gain for these set of data samples was $G = 100\,dB$, the sampling frequency was $10\,Msample/s$, and the ceramic number one was also included in the excited ceramics. Each ceramic was stimulated with a $40\,kHz$ sinusoidal signal, the delays between the input signals have been computed in order to vary the horizontal angle ϕ in the interval $-15° \leq \phi \leq 15°$, with steps of 0.5°.

A depiction of the ceramics emitting at different time is visible in fig. 3.26.
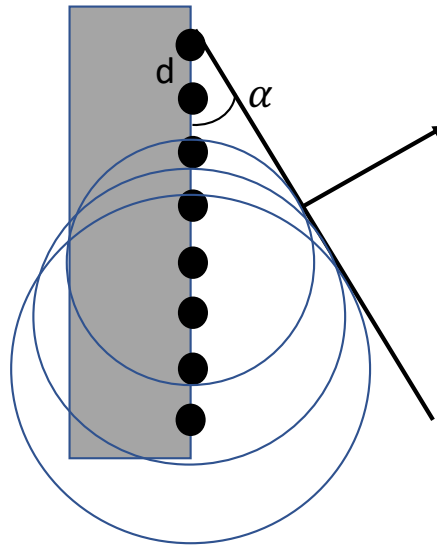
Figure 3.26. Scheme of the ceramics excited with a proper delayed signal, in order to change the direction of the acoustic signal.

Of course, due to the different distances between each ceramic and the hydrophone and due to the different response of each ceramic to the exciting input signal, in order to superimpose in phase all the signals on the hydrophone, a proper delay had to be applied to each input signal. As an example, in table 3.2 are shown the delays applied to each input signal, in order to focus the acoustic signal on the hydrophone placed at $1.5\,m$ distance from the centre of the parametric source. Then, to change the horizontal angle ϕ, these delays have been properly changed.

Ceramic number	Delay $[\mu s]$
1	-12.08
2	-4.40
3	-1.65
4	0.00
5	1.10
6	1.00
7	-2.20
8	-6.58

Table 3.2. Delay introduced for every ceramics. Ceramic number 4 does not have any delay because it has been chosen as benchmark.

Then a new set of delays was used to focus the acoustic signal on an hypothetical hydrophone placed at $1\,km$ distance $\phi = 0$ (we have named this position "infinity"). A new sample of data have been collected varying the direction of acoustic signal with the horizontal angle $-15° \leq \phi \leq 15°$, with steps of $1°$ (we are still considering the signal at $40\,kHz$). Data acquired are reported in table A.7 and table A.8 and are plotted respectively in fig. 3.28 (focus at $1.5\,m$) and fig. 3.29 (focus at "infinity"). These figures show the amplitude of the signal acquired by the hydrophone, as a function of the nominal horizontal deviation ϕ, realized by applying the proper delays to the ceramic input signals. The delays calculated for each ceramic for the focus at $150\,cm$ at $40\,kHz$ are reported, as an example, in table 3.3. They have been calculated using the expression

$$\Delta t = \frac{d \cdot sin\alpha}{v_s} \tag{3.2}$$

where d is the distance among the ceramics, α is the angle between the source and wavefront (see fig. 3.26) and $v_s = 1489\,m/s$ is the sound velocity.

The measures, for the two different focus, are repeated for the frequency $25\,kHz$, but with the angular interval $-20° \leq \phi \leq 20°$, with steps of $1°$ or $2°$. These data are reported in table A.9 and table A.10.

Figure 3.27 shows the result obtained with $25\,kHz$ input signal during the data acquisition session. Figure 3.30 and fig. 3.31 show the results obtained with this analysis.

Angle [°]	Delays [μs]							
	C1	**C2**	**C3**	**C4**	**C5**	**C6**	**C7**	**C8**
-15	20.86	13.91	6.95	0	-6.95	-13.91	-20.86	-27.81
-14	19.50	13.00	6.50	0	-6.50	-13.00	-19.50	-26.00
-13	18.13	12.09	6.04	0	-6.04	-12.09	-18.13	-24.17
-12	16.76	11.17	5.59	0	-5.59	-11.17	-16.76	-22.34
-11	15.38	10.25	5.13	0	-5.13	-10.25	-15.38	-20.50
-10	13.99	9.33	4.66	0	-4.66	-9.33	-13.99	-18.66
-9	12.61	8.40	4.20	0	-4.20	-8.40	-12.61	-16.81
-8	11.22	7.48	3.74	0	-3.74	-7.48	-11.22	-14.95
-7	9.82	6.55	3.27	0	-3.27	-6.55	-9.82	-13.10
-6	8.42	5.62	2.81	0	-2.81	-5.62	-8.42	-11.23
-5	7.02	4.68	2.34	0	-2.34	-4.68	-7.02	-9.37
-4	5.62	3.75	1.87	0	-1.87	-3.75	-5.62	-7.50
-3	4.22	2.81	1.41	0	-1.41	-2.81	-4.22	-5.62
-2	2.81	1.88	0.94	0	-0.94	-1.88	-2.81	-3.75
-1	1.41	0.94	0.47	0	-0.47	-0.94	-1.41	-1.88
0	0	0	0	0	0	0	0	0
1	-1.41	-0.94	-0.47	0	0.47	0.94	1.41	1.88
2	-2.81	-1.88	-0.94	0	0.94	1.88	2.81	3.75
3	-4.22	-2.81	-1.41	0	1.41	2.81	4.22	5.62
4	-5.62	-3.75	-1.87	0	1.87	3.75	5.62	7.50
5	-7.02	-4.68	-2.34	0	2.34	4.68	7.02	9.37
6	-8.42	-5.62	-2.81	0	2.81	5.62	8.42	11.23
7	-9.82	-6.55	-3.27	0	3.27	6.55	9.82	13.10
8	-11.22	-7.48	-3.74	0	3.74	7.48	11.22	14.95
9	-12.61	-8.40	-4.20	0	4.20	8.40	12.61	16.81
10	-13.99	-9.33	-4.66	0	4.66	9.33	13.99	18.66
11	-15.38	-10.25	-5.13	0	5.13	10.25	15.38	20.50
12	-16.76	-11.17	-5.59	0	5.59	11.17	16.76	22.34
13	-18.13	-12.09	-6.04	0	6.04	12.09	18.13	24.17
14	-19.50	-13.00	-6.50	0	6.50	13.00	19.50	26.00
15	-20.86	-13.91	-6.95	0	6.95	13.91	20.86	27.81

Table 3.3. Delays [μs] applied to each ceramic in order to vary the emission angle. The table refers to the focus at $150\,cm$ at $40\,kHZ$. Ceramic number 4 does not have any delay because it has been chosen as benchmark.
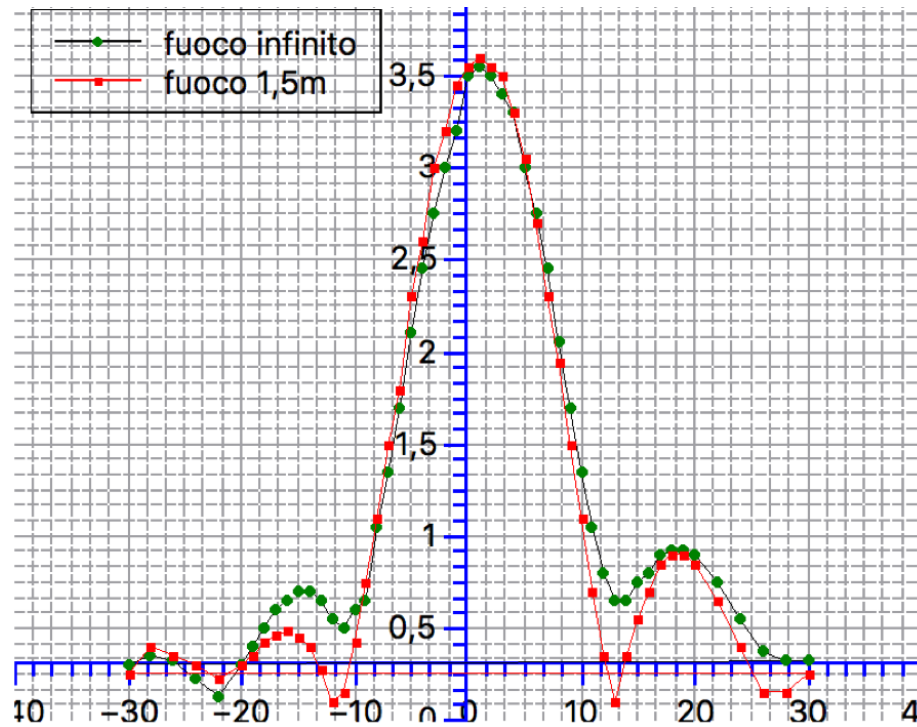
Figure 3.27. Pattern obtained at $25\,kHz$, for two different focus. The shifted peak is visible for each curves at 1°.

An on-line data analysis performed in order to test the parametric antenna setting, did reveal that the resulting direction of acoustic signal was shifted by 1° with respect to the antenna-receiver axis. This is visible in fig. 3.27 obtained with the on-line data analysis.

We can make some remarks on the data shown in figs. 3.28 to 3.31; the graphs are shifted by 1° to the left (this offset is visible also in fig. 3.27). To ensure that the angle corresponding to the peak was the right one, we have interpolated the central part of the distribution with a Gaussian curve and then we have extracted the coordinates of the peak, that results to be at 1°. In these plots is noticeable the highest position of the secondary maxima for the focus at infinity, respect to the focus at $150\,cm$, for both frequencies. We see that with the parametric source is possible to obtain a very narrow acoustic beam: when it is focused at the proper distance, the acoustic beam is well contained in $\pm10°$; therefore, we can obtain a signal very similar to the one induced by an high energy neutrino interacting in water.
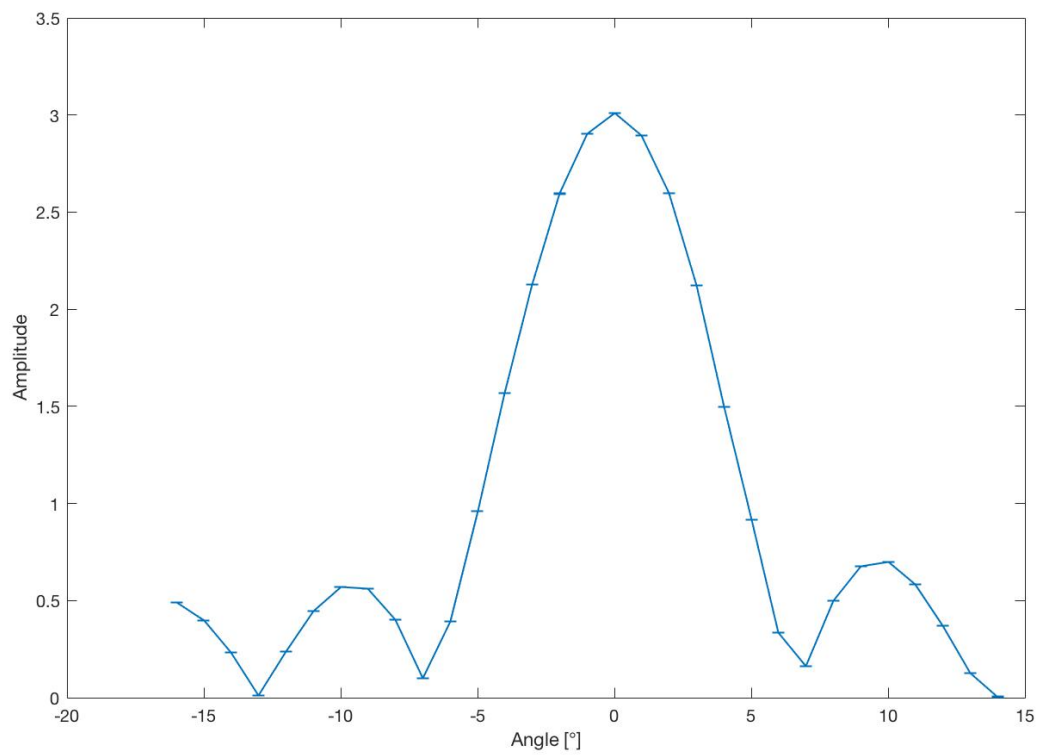
Figure 3.28. Amplitude, with related uncertainties, for the focus at $150\,cm$ at $40\,kHz$.
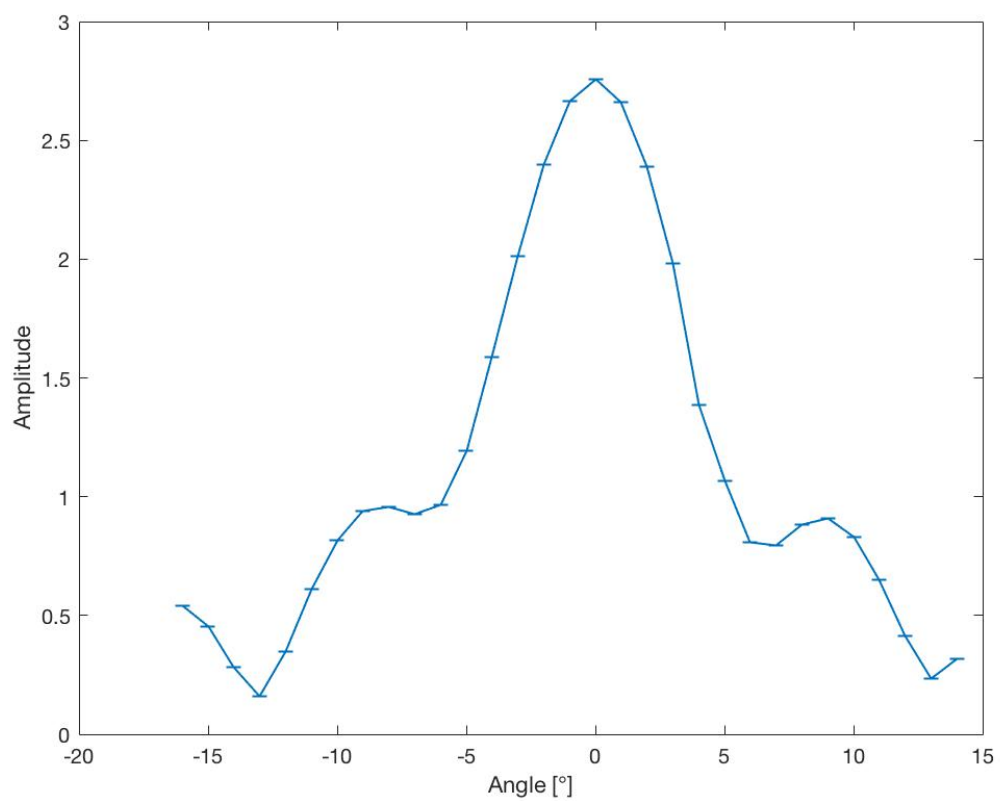
Figure 3.29. Amplitude, with related uncertainties, for the focus at infinity at $40\,kHz$.
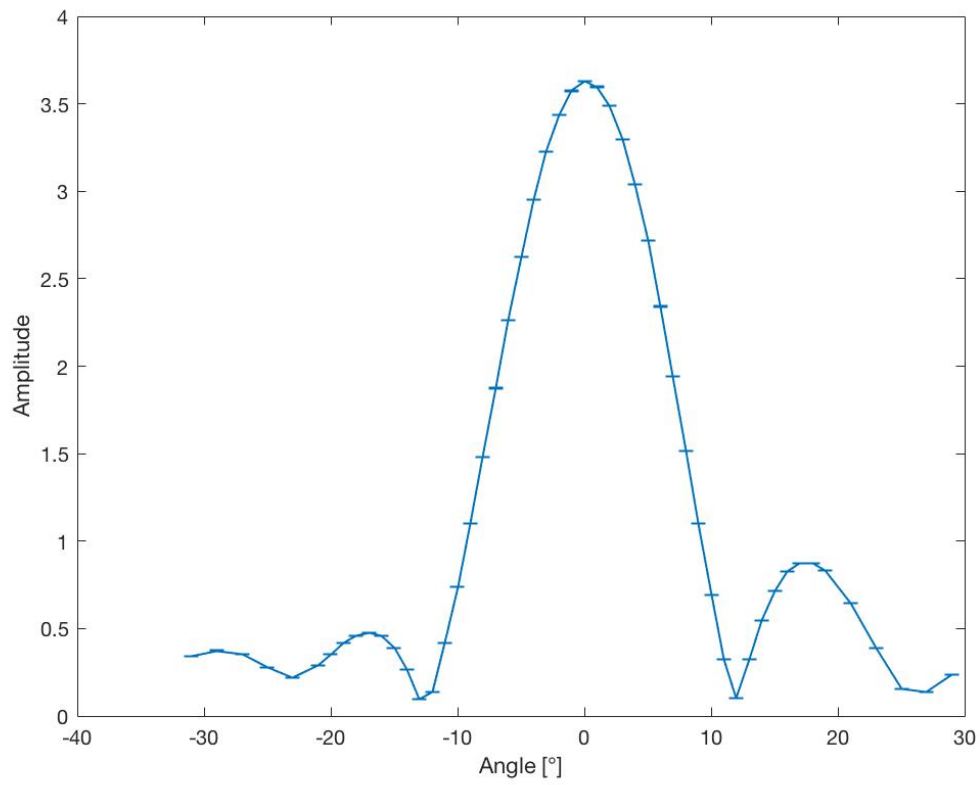
Figure 3.30. Amplitude, with related uncertainties, for the focus at $150\,cm$ at $25\,kHz$.
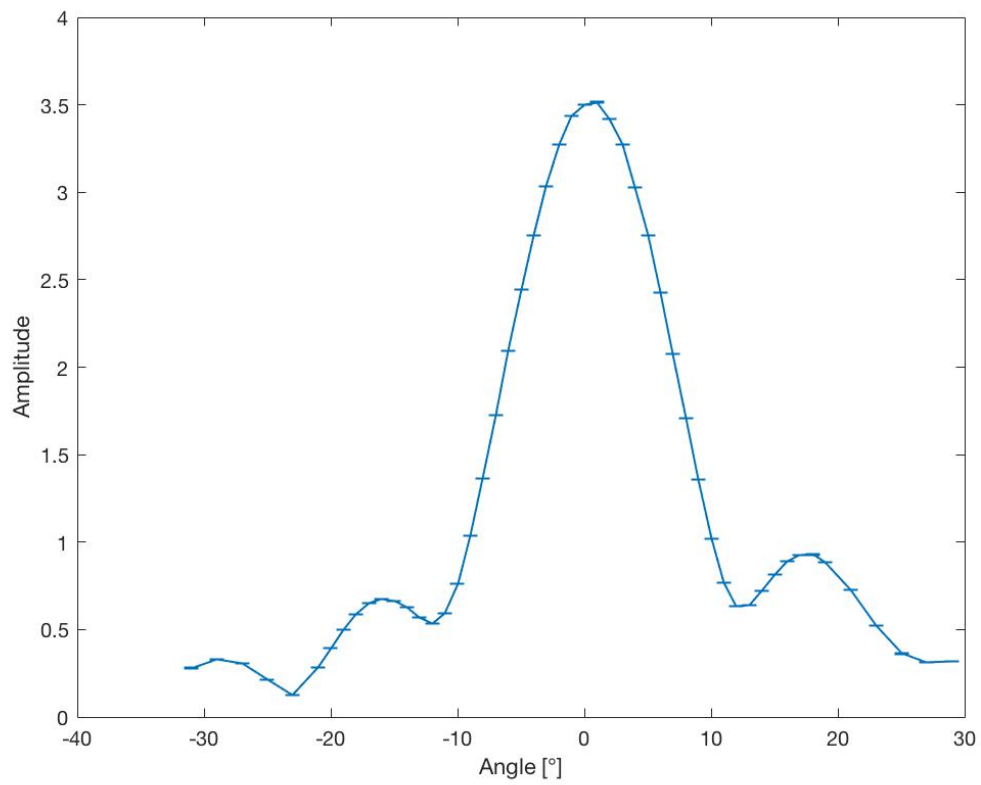
Figure 3.31. Amplitude, with related uncertainties, for the focus at infinity at $25\,kHz$.

3.2.4   Study of the Directivity of the Source on a Vertical Plane

The following set of measures had the purpose of studying the signal distribution in the plane orthogonal to the source plane. To acquire this set of data, the parametric antenna was rotated and aligned to a vertical plane. In this condition a rotation of the supporting pole was creating an angle θ between the plane defined by the antenna and the receiving hydrophone (see fig. 3.13). Data have been collected for $-90° \leq \theta \leq 90°$, with 5° or 10° steps. Now data are mediated on 10 sampling, the gain is $G = 100$ and the supply voltage is setted at $1.5\,V$. Tests are made for these frequencies: $15\,kHz$, $25\,kHz$, $35\,kHz$ and $40\,kHz$. Data acquired are reported in tables A.11 to A.14.

This type of analysis is similar to the analysis made for the source laid on the horizontal plane (see section 3.2.2). Even in this case, in fact, we have calculated the right distance between every ceramic and the hydrophone and then the right angle corresponding to nominal one. The amplitudes for the four frequency examined, as a function of the right angle, are summarised in fig. 3.32.

As a final outcome, we can say that the acoustic signal generated by the parametric source is narrow on the horizontal angle ϕ, while is nearly uniformly distributed all around the source (on the angle θ). This is what is expected for the acoustic signal generated by a high energy neutrino interaction in water.
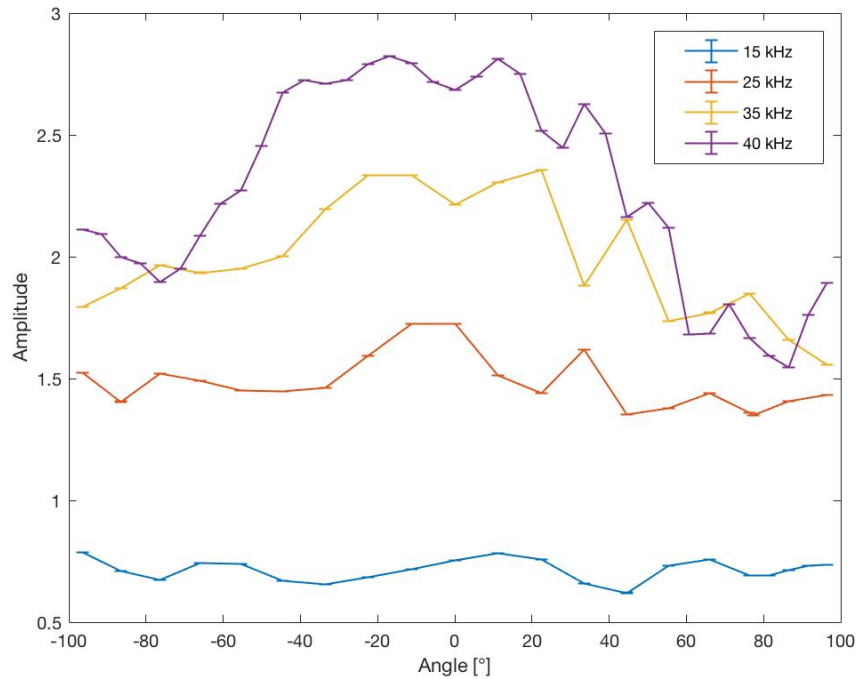
Figure 3.32. Amplitude, with related uncertainties, as a function of the real angle of emission, for the source laid on a vertical plane, at various frequencies.

3.2.5 Linearity of Response of the Parametric Acoustic Source Varying the Input Voltage

The hydrophone used to acquire the acoustic signals is calibrated and can provide the absolute measure of the acoustic signal pressure. To complete the calibration of the parametric source, a sample of data has been collected for different values of the amplitude of the input signal generated by the audio card: $V_{in} = \{0.50; 0.75; 1.00; 1.25; 1.50; 1.75; 2.00\}\, V$. For $V_{in} = 2.25\, V$ the output signal, i.e. the hydrophone signal, did show a distortion due to the saturation of the ceramics.

The calibration data sample was collected with the angular beamsteering set in order to have the maximum at 1°, with $25\, kHz$ sinusoidal input, and its amplitude in the interval $0.50\, V \leq V_{in} \leq 2.0\, V$.

Knowing the conversion factor from $[V]$ to $[Pa]$, for the calibrated hydrophone, we can obtain the acoustic pulse in pressure. At $25\, kHz$ the conversion factor is $344\, Pa/V$. Both amplitudes, in terms of voltage and pressure, are reported in table 3.4. The amplitudes are also shown, as a function of the input voltage, in fig. 3.33.

V_{in} [V]	**Amplitude** [V]	**Amplitude** [kPa]
0.5	$1.16 \pm (0.12 \cdot 10^{-3})$	$0.40 \pm (0.04 \cdot 10^{-3})$
0.75	$1.75 \pm (0.15 \cdot 10^{-3})$	$0.60 \pm (0.05 \cdot 10^{-3})$
1.00	$2.33 \pm (0.17 \cdot 10^{-3})$	$0.80 \pm (0.06 \cdot 10^{-3})$
1.25	$2.91 \pm (0.21 \cdot 10^{-3})$	$1.00 \pm (0.07 \cdot 10^{-3})$
1.50	$3.50 \pm (0.24 \cdot 10^{-3})$	$1.20 \pm (0.08 \cdot 10^{-3})$
1.75	$4.10 \pm (0.28 \cdot 10^{-3})$	$1.41 \pm (0.10 \cdot 10^{-3})$
2.00	$4.65 \pm (1.09 \cdot 10^{-3})$	$1.60 \pm (0.37 \cdot 10^{-3})$

Table 3.4. Amplitude of the signal both in terms of voltage and pressure, for different values of input voltage signal.
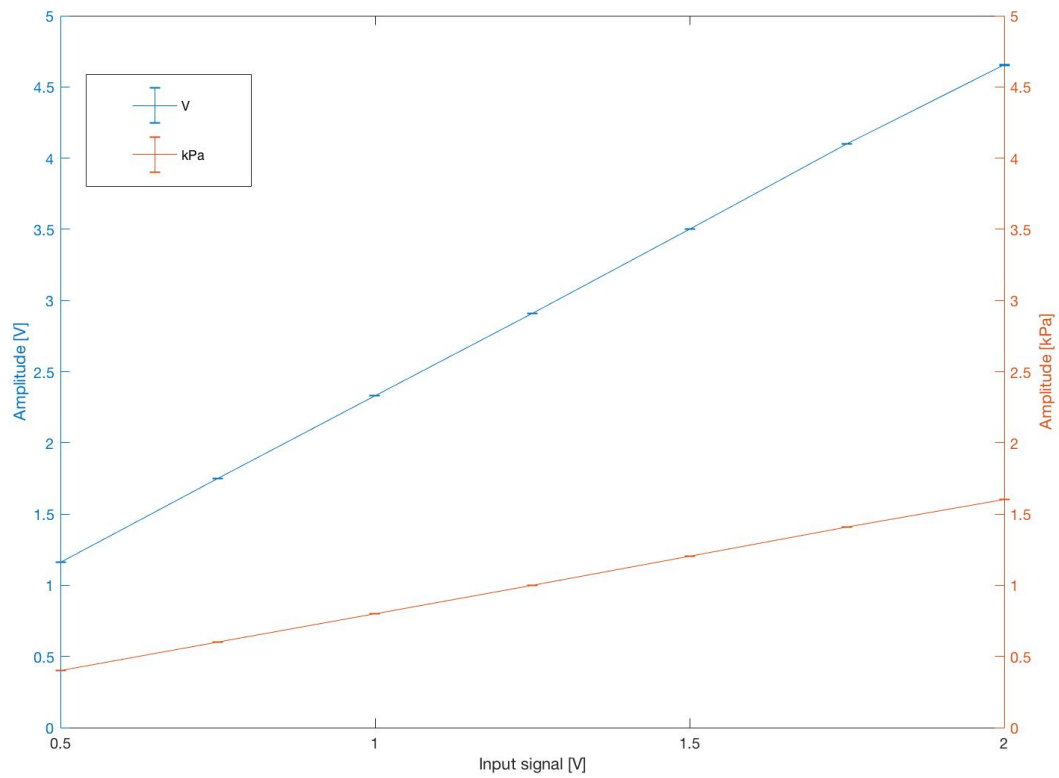
Figure 3.33. Amplitude of the signal in terms of voltage [V] and pressure [kPa] at $25\,kHz$, with related uncertainties, as a function of the amplitude peak-peak of the input signal.

Chapter 4

Acoustic Signal Simulation

In this chapter we will use the results achieved with the calibration of the parametric source to define how it will be possible to simulate, in water, the acoustic signal induced by high energy neutrino interactions. The characteristics of the neutrino induced acoustic signal have been obtained from the ACoRNE Collaboration. From the simulation of the pressure signal, available at the website [3], we get its angular distribution and its time dependence.

We have seen in chapter 3 that the parametric source can generate a pressure signal with the angular characteristics very similar to the one expected by a neutrino interaction. We have now to evaluate which kind of signal, in the time domain, should be used as input to the ceramics in order to have a bipolar signal similar to the one due to neutrino interactions in water. Both the signal generated by the parametric source and the transmission in water of the acoustic signal are function of the frequency; to describe how the source transforms the time profile of an input voltage signal, following the results described in chapter 3, we can define its time-frequency transfer function.

In the following sections the calculation process will be described. In a few words, we have generated a MATLAB code in order to evaluate the transfer function of the apparatus. The absorption in water of the acoustic pulse has been parametrized, as a function of the frequency, with a generally used formula provided by Ainslie and McColm [64]. The knowledge of this two functions and of the ACoRNE simulated bipolar pulses are the starting point to evaluate the input signal, in the time domain, necessary to simulate the neutrino acoustic signal with our device. In fact, using the ACoRNE pulses and reversing the propagation process in water we can get the signal not propagated, i.e. when it is just generated, and therefore, using the transfer function of the apparatus, get the input.

4.1   ACoRNE Simulation Program

Thanks to the ACoRNE simulation program, we have obtained the time dependence of the acoustic wave induced by UHE ($10^{17} - 10^{21}\ eV$) neutrino interactions in water. This simulation program comes from the modification of a Monte Carlo written to simulate high energy cosmic rays air showers, $CORSIKA$. The ACoRNE group has modified it in order to work in a water or ice medium (see [60] for a complete description). The code used is attached and described in appendix C. The output of the simulation represents the amplitude and the time profile of the acoustic signal sampled in a fixed position at a defined distance from the deposited energy; the pulse so simulated has a characteristic bipolar shape that is due to the transverse dimension of the density energy released by the neutrino interaction in water. We have used this code to simulate bipolar pulses, due to neutrinos with different energies, in order to know the real neutrino signal and to reproduce it with our parametric source.

An example of hadronic shower in water produced by neutrino and its Fourier transform, obtained with this code, are shown in fig. 4.1 and fig. 4.2. It represents the bipolar pressure pulse due to the interaction of a neutrino with $10^{11}\ GeV$ energy, $1\ km$ distant from a detector. The attenuation has been calculated with the Ainslie and McColm formula.
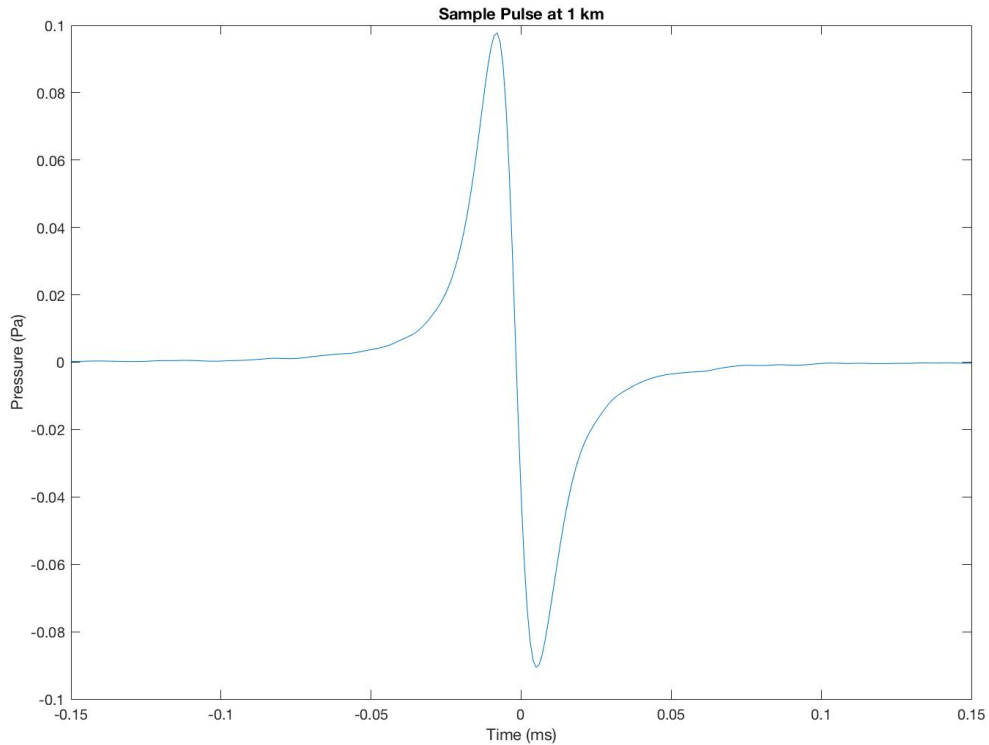
Figure 4.1. Simulated bipolar pulse at $1\ km$, with $10^{11}\ GeV$ primary energy, obtained with the ACoRNE simulation program, attenuated with the Ainslie and McColm method.
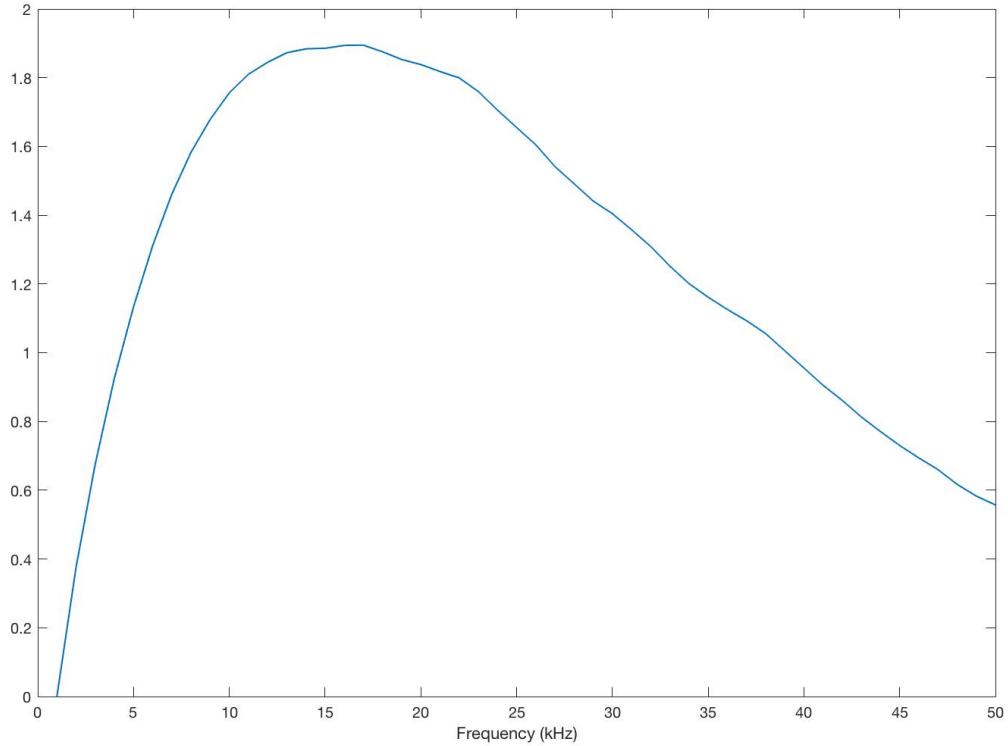
Figure 4.2. Fourier transform of the simulated bipolar pulse at $1\,km$, with $10^{11}\,GeV$ primary energy, obtained with the ACoRNE simulation program, attenuated with the Ainslie and McColm method.

As visible from fig. 4.1, we have an almost symmetric bipolar pressure pulse $0.1\,Pa$ high with a duration of about $0.1\,ms$. In general, the amplitude is proportional to the deposited shower energy density: in first approximation we assume that hadronic showers induced by neutral current interactions of any kind of neutrino will originate the same energy density profile expected by a ν_e charged current interaction. We will not make a distinction on the kind of neutrino and we will simulate hadronic showers due to the interactions of UHE neutrinos a few kilometres distant from the hydrophone. The simulated bipolar pulse takes already into account the attenuation due to the propagation in water.

The calibration in amplitude obtained in the last paragraph of chapter 3 will give us also the possibility to reconstruct the neutrino energy. What we really need to know is the time profile and the amplitude of the signal that we should send in input to the ceramics of our parametric source in order to simulate the neutrino signal sampled by the acoustic detector. Since the propagation of the acoustic wave in water is affected by an attenuation process that is frequency dependent, we decided to perform our analysis in the frequency domain.

What we get from the simulation program is a bipolar pulse as a function of the time $V_{H\_out}(t)$ (see fig. 4.1), that can be also described by its Fourier transform $V_{H\_out}(\omega)$ (see fig. 4.2). This pulse has been simulated at $1\,km$ distance from the energy deposition, and takes already into account the attenuation. If we define $P_{Shower\_out}(\omega)$ the signal generated by the shower, we can write

$$V_{H\_out}(\omega) = P_{Shower\_out}(\omega) \cdot Att(\omega) \tag{4.1}$$

where $Att(\omega)$ describes the total attenuation due to $1\,km$ path in water. Inverting the equation above we can extract the signal not attenuated $P_{Shower\_out}(\omega)$, and then get it as a function of the time, using the inverse Fourier transform. It is clear that $P_{Shower\_out}(\omega)$ is, in the frequency domain, what we want to get as output from the parametric source, i.e. $P_{Source\_out}(\omega)$.

The knowledge of the parametric source transfer function $H(\omega)$ give us the possibility to relate the output $P_{Source\_out}(\omega)$ with the signal, in the time domain $V_{Source\_in}(t)$, that should be used as input to the parametric source, as follows

$$V_{Source\_in}(t) = \mathcal{F}^{-1}\Big[\frac{P_{Source\_out}(\omega)}{H(\omega)}\Big]. \tag{4.2}$$

4.2   Linear Time-Invariant System

From now on we will use the Laplace transform instead of the Fourier transform to take into account the amplitude and phase evolution of the signal during the propagation into the system (parametric source and water). The acoustic source that we are considering is a linear time-invariant (LTI) system. It is characterized, in the frequency domain, by the transfer function $H(s)$, that links the Laplace transform of the input $X(s) = \mathcal{L}\{x(t)\}$ with the Laplace transform of the output $Y(s) = \mathcal{L}\{y(t)\}$, by the formula

$$Y(s) = H(s) \cdot X(s). \tag{4.3}$$

The transfer function $H(s)$ itself is the Laplace transform of the response of the system to a Dirac delta pulse $\delta(t)$; this means that eq. (4.3) becomes a convolution in the time domain

$$y(t) = \delta(t) * x(t). \tag{4.4}$$

The Laplace transform of a function $f(t)$ is a function of the complex variable $s = \sigma + i\omega$ and is defined by

$$F(s) = \int_0^\infty f(t)e^{-st}dt. \tag{4.5}$$

When $s = i\omega$, and $\sigma = 0$, the Laplace transform coincides with the Fourier transform with real argument ω. This simplification is consistent with our case, and this is the reason why we mention only the Fourier transform during the thesis.

If the signal $A(\omega)$ is sent in input to a system obtaining in output $B(\omega)$, the transfer function can be expressed, with a ratio of polynomials, as follows

$$H(\omega) = \frac{B(\omega)}{A(\omega)} = \frac{b_0 + b_1\omega + ... + b_n\omega^n}{a_0 + a_1\omega + ... + a_m\omega^m} \tag{4.6}$$

that can be written also by highlighting the zeros z_i and the poles p_i

$$H(\omega) = \frac{(\omega - z_1)(\omega - z_2)...(\omega - z_n)}{(\omega - p_1)(\omega - p_2)...(\omega - p_m)} = \frac{\prod_{i=1}^{n}(\omega - z_i)}{\prod_{i=1}^{m}(\omega - p_i)}. \tag{4.7}$$

This expression is particularly convenient since MATLAB expresses the transfer function with polynomials.

4.3   Attenuation Formula

As described in section 2.2.2 the attenuation in water is well represented by the formula $I(x) = I_0 e^{-\alpha x}$ where α is the attenuation. To calculate the attenuation of the sound in water we may use the simplified formula suggested by Ainslie and McColm [64], that is valid in the Mediterranean Sea between $100\,Hz$ and $1\,MHz$. This formula is a function of the frequency $[kHz]$ and it depends on intrinsic water parameters like temperature T $[°C]$, salinity S $[PSU]$, depth z $[km]$ and pH. It is also function of the relaxation frequencies $[kHz]$ of the boric acid (f_1) and magnesium sulphate (f_2)

$$f_1 = 0.78\left(\frac{S}{35}\right)^{\frac{1}{2}} e^{\frac{T}{26}} \tag{4.8}$$

$$f_2 = 42 e^{\frac{T}{17}}. \tag{4.9}$$

Using these expressions we obtain

$$\alpha = 0.106\frac{f_1 f^2}{f_1^2 + f^2} e^{\frac{pH-8}{0.56}} + 0.52\left(1 + \frac{T}{43}\right)\left(\frac{S}{35}\right)\frac{f_2 f^2}{f_2^2 + f^2} e^{-\frac{z}{6}} + 0.00049 f^2 e^{-\left(\frac{T}{27} + \frac{z}{17}\right)} \tag{4.10}$$

where α is the attenuation in dB/km. To perform the calculations we have assumed $pH = 8$, $T = 14\,°C$ and $S = 38\,PSU$, the last two given in [62] by the NEMO Collaboration.

Having in mind this formula, we can obtain from α the ratio between the initial (at the shower level) and final (close to the hydrophone) amplitudes, that quantifies the attenuation at the various frequencies, as a function of the distance. The attenuation due to the propagation in water, as well as the geometrical attenuation, allow us to estimate the shape of the pressure wave after it travelled in the water medium, along a certain distance.

4.4 Driving the Parametric Source to Obtain a Bipolar Pulse on an Acoustic Detector

Our purpose is to define an input signal that should be sent to the parametric source to generate a bipolar pulse that simulates a neutrino event. In order to get this result we have used the characterization of the parametric source, in amplitude and in the frequency domain, obtained in chapter 3. With a code developed in MATLAB, attached and commented in appendix D, we have evaluated the transfer function both for the amplitudes and phases, as a functions of the frequencies. To get this transfer function we have used only the data collected with the parametric source oriented perpendicular to the source-hydrophone direction (angle $\phi = 0$) for all the frequency interval (see figs. 3.14 to 3.19 in section 3.2.2). As described in section 3.1, we fed the parametric source with sinusoidal input signals, so we can evaluate the complex transfer function, at different frequencies, as

$$y(\omega) = r(\omega)e^{i\theta(\omega)} \qquad (4.11)$$

where $r(\omega)$ is the amplitude and $\theta(\omega)$ is the phase measured. Since we know the input signal $x(\omega)$ we can evaluate the complex transfer function, expressed in the form

$$H(\omega) = \frac{y(\omega)}{x(\omega)} = \frac{B(\omega)}{A(\omega)} = \frac{b_0 + b_1\omega + ... + b_n\omega^n}{a_0 + a_1\omega + ... + a_m\omega^m} \qquad (4.12)$$

having used the expression in eq. (4.6).

Hence, using the MATLAB mathematical tools, from the results obtained in chapter 3 that are reported in table 4.1, we are able to evaluate the coefficients of the transfer function $B(\omega)$ and $A(\omega)$. MATLAB allows to define the order of the polynomials; we have chosen them in order to avoid the divergence due to the zeros and poles. We care about the zeros of the transfer function, since they could induce divergences when, eventually, we will evaluate the result of the inversion of the transfer function.

The coefficients b_i and a_i allow to get an analytical function that describes the transfer function. The amplitude and the phase of the transfer function are shown in fig. 4.3, where the red circles are the experimental data of amplitudes and phases and the blue lines describe the results of the interpolations.

Frequency $[kHz]$	Amplitude $[V]$	Phase $[rad]$
15	1.36	-0.60
20	1.98	-0.78
25	3.21	-0.67
30	3.78	-0.91
35	4.32	-1.20
40	4.86	-2.03

Table 4.1. Amplitudes and phases at angle $\phi = 0$, obtained in chapter 3, used to estimate the parametric source transfer function, at various frequencies.
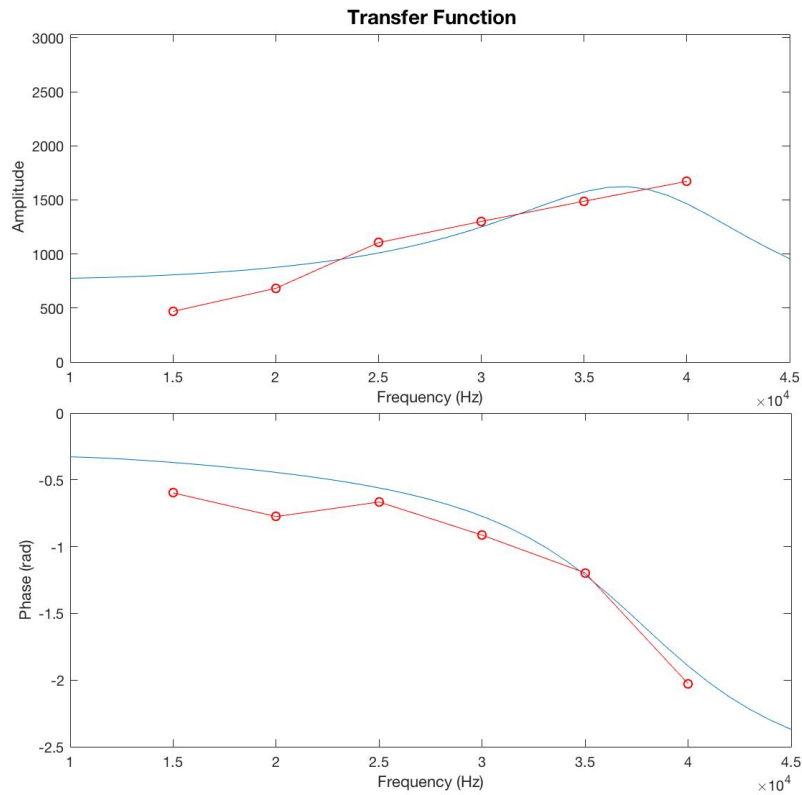
Figure 4.3. Amplitude and phase of the transfer function. Amplitudes and phases measured are the red circles, and the blue lines are the polynomials produced by the interpolation.

As previously stated, the attenuation in water is due to two effects. One effect is geometrical and the other is due to the absorption and diffusion of sound in water (see section 2.2.2 and section 4.3). The attenuation in water has been evaluated according to eq. (4.10), as a function of the frequency and of the distance travelled by the sound wave. The geometrical attenuation, is a quantity that depends only on the inverse of the distance and acts on the amplitude of the signal, reducing it. Concerning the attenuation due to the interactions in water, we have evaluated its effects only on the amplitude of the signal, and

not on its phase. We decided to neglect the frequency dependency of the speed of sound (few cm/s in the range $0 - 100\,kHz$), to be compatible with the ACoRNE evaluation of the pressure signal. The attenuation value has been derived from the attenuation calculated in $[dB/km]$, using eq. (4.10): it quantifies the ratio between the amplitude of the propagated signal and its initial value. In table 4.2 we report, for few values of the frequency the expected attenuation of the sound wave amplitude, calculated for a distance of $1\,km$. A more complete description of this attenuation in visible in fig. 4.4. From the figure is clearly visible that the low frequencies are not much attenuated; on the contrary, the high frequencies are increasingly attenuated.

Frequency $[kHz]$	Attenuation
1	0.99
5	0.96
10	0.90
15	0.80
20	0.69
30	0.46
50	0.15
100	0.01

Table 4.2. Attenuation values for various frequencies, calculated for a distance of $1\,km$. The values in table represent the ratio between the amplitude of the propagated signal in water and its initial value.
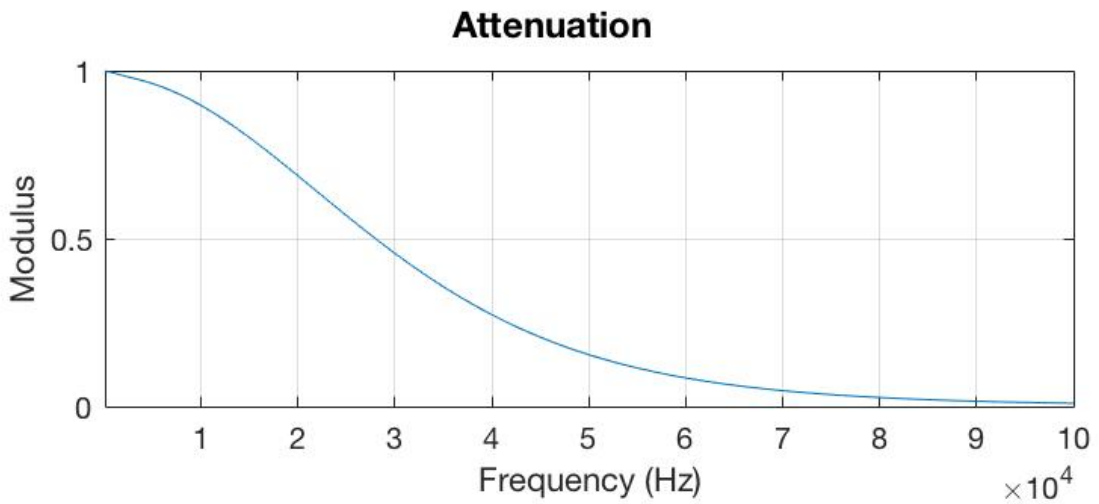
Figure 4.4. Attenuation in water, as a function of the frequency, calculated for a distance of $1\,km$. It quantifies the ratio between the amplitude of the propagated signal and the initial amplitude.

In our case, starting from the knowledge of the bipolar pulse $V_{H\_out}(t)$, expected to be measured by an acoustic detector (hydrophone), we have evaluated its Fourier transform $V_{H\_out}(\omega)$. Then we have connected $V_{H\_out}(\omega)$ with the signal produced by the neutrino induced shower close to the interaction region $P_{Shower\_out}(\omega)$ as follows

$$V_{H\_out}(\omega) = P_{Shower\_out}(\omega) \cdot Att(\omega). \tag{4.13}$$

Then, we can write $P_{Shower\_out}(\omega)$ as

$$P_{Shower\_out}(\omega) = \frac{V_{H\_out}(\omega)}{Att(\omega)}. \tag{4.14}$$

Our parametric source has to produce a signal in pressure $P_{Source\_out}(\omega)$, as similar as possible to $P_{Shower\_out}(\omega)$. To obtain this result we chose a proper function of the time for the signal that we have to send to the parametric source, $V_{Source\_in}(t)$. If $H(\omega)$ is the parametric source transfer function that represents how the device transform, in the frequency domain, a voltage input signal into pressure wave ($V_{Source\_in}(\omega)$ to $P_{Source\_out}(\omega)$), we want that

$$P_{Source\_out}(\omega) = V_{Source\_in}(\omega) \cdot H(\omega) = V_{Source\_in}(\omega) \cdot \frac{b_0 + b_1\omega + ... + b_n\omega^n}{a_0 + a_1\omega + ... + a_m\omega^m} \tag{4.15}$$

having used eq. (4.6).
Finally we can obtain $V_{Source\_in}(\omega)$, by inverting eq. (4.15), as

$$V_{Source\_in}(\omega) = \frac{P_{Source\_out}(\omega)}{H(\omega)} = P_{Source\_out}(\omega) \cdot \frac{a_0 + a_1\omega + ... + a_m\omega^m}{b_0 + b_1\omega + ... + b_n\omega^n} \tag{4.16}$$

and then we can obtain $V_{Source\_in}(t)$ by using the inverse Fourier transform of $V_{Source\_in}(\omega)$. In such a way, knowing the neutrino pressure pulse from the simulations, as a function of the time, we can figure out the input signal, as a function of time, that we have to send to the parametric source to simulate it. The calculations have been made in the frequency domain, using MATLAB functions that implement the Fast Fourier Transform (FFT) and its inverse (IFFT).

Using the ACoRNE code we have simulated the charge current interaction, in water, of a neutrino with $10^{11}\ GeV$ energy. From the hadronic shower so generated, the code allows to evaluate the pulse measured by an acoustic detector $1\ km$ distant from the interaction. The bipolar pulse so obtained is shown in fig. 4.1.

Figure 4.5 shows the inverse Fourier transform of $P_{Source\_out}(\omega)$, while fig. 4.6 shows $V_{Source\_in}(t)$, i.e. the inverse Fourier of the $V_{Source\_in}(\omega)$. The first is the pulse not propagated in Pa, i.e. just got out from the source, reconstructed from the ACoRNE simulation. The second is the input signal, in $Volt$, that we have to apply to the parametric source to obtain in output the pressure wave shown in fig. 4.5. This pressure wave, after $1\,km$ propagation, will give the signal in fig. 4.1. Figure 4.5 and fig. 4.6 show an high frequency component that is clearly not evident in fig. 4.1. This is the result of the eq. (4.14), that evaluate the pressure wave not propagated from the simulated ACoRNE pulse: the attenuation in water (represented by the transfer function $Att(\omega)$) is more effective at high frequency so, dividing by $Att(\omega)$, we increase the contribution of the high frequency components. Just reversing this statement we can say that the presence of an high frequency component in input to the parametric source would not influence the final pressure pulse because it would be attenuated.
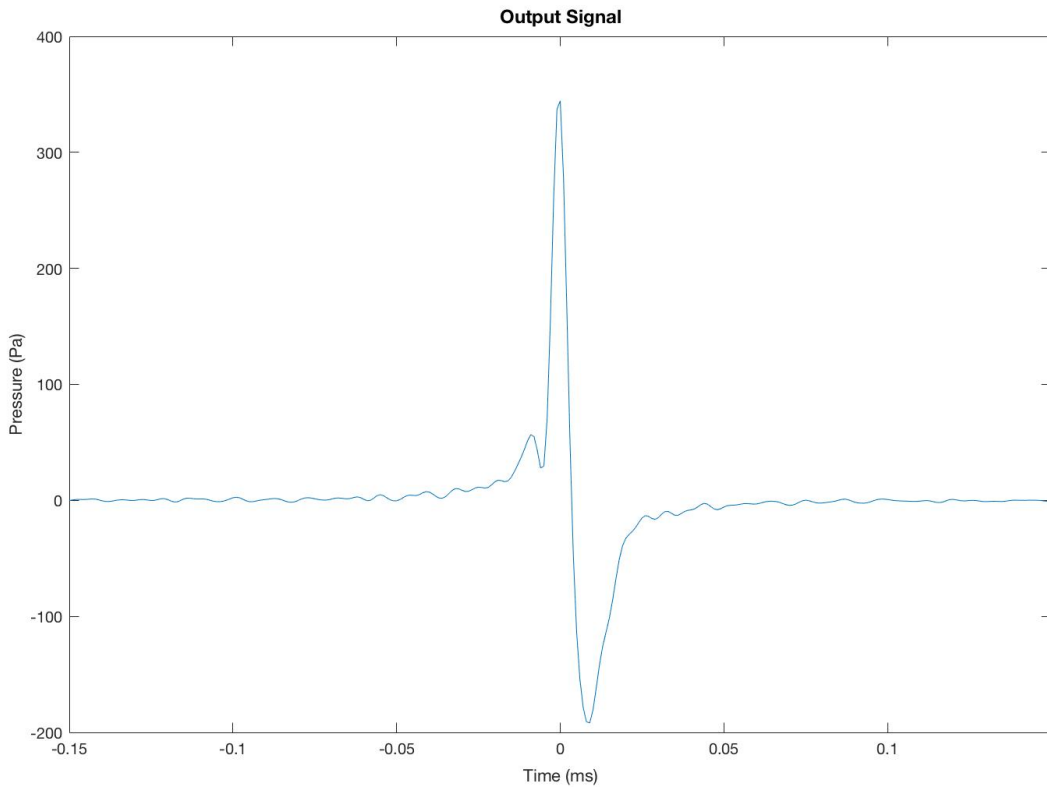
Figure 4.5. Simulated output signal not propagated, reconstructed from a simulated bipolar pulse at $1\,km$, with $10^{11}\,GeV$ primary energy, obtained with the ACoRNE simulation program.
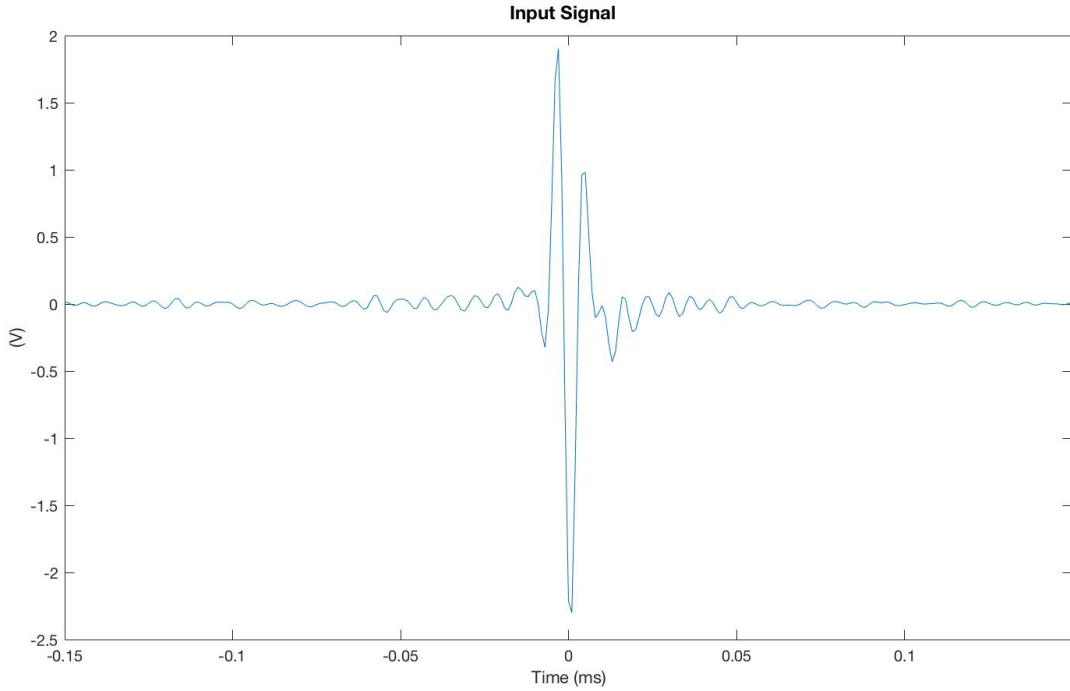
Figure 4.6. Simulated input signal reconstructed from a simulated bipolar pulse at $1\,km$, with $10^{11}\,GeV$ primary energy, obtained with the ACoRNE simulation program.

In the calculations, that allowed us to obtain fig. 4.5 and fig. 4.6, (see appendix D) we have reduced the high frequency content using a low-pass filter with the cutoff frequency setted to $48\,kHz$. In fact, knowing the features of the apparatus, it is meaningless to examine frequencies above the Nyquist frequency. In this way, we are allowed to set the attenuation coefficient at a constant above $160\,kHz$, in order to avoid divergences in the computation. Indeed, it is very significant at high frequencies, and the multiplication between the signal and this factor can caused divergences.

Chapter 5

Conclusions

The present work concerns the characterization of a parametric acoustic source to be used to calibrate an apparatus for the acoustic detection of UHE neutrinos. It consists in the data analysis of acoustic signals generated by a parametric source and collected by a calibrated hydrophone. This analysis is supplemented by the study of the parametric source transfer function that, using the ACoRNE simulation of neutrino pulse in water, enables us to compute the input voltage signal to apply to the source in order to obtain a bipolar pressure pulse.

The first chapter is an overview of ultra high energy cosmic rays and the various detection techniques.

The second chapter contains the descriptions of neutrino interactions in water and of sound wave propagating in water, including attenuation phenomena.

The third chapter focuses on the characterization of the parametric acoustic source, by analysing the data acquired at the IDASC. The parametric source, that could rotate around its axis, was excited with sinusoidal input signals at various frequency. Initially we characterized each ceramic by stimulating it singularly. Then we studied the directivity of the parametric source changing its position, by rotating the pole around its axis. We compared these data to the theoretical beampatterns, for various frequencies, and their main lobes seem to be in agreement. The succeeding session of measure concerns the angular beamsteering, i.e. the possibility of changing the direction of the acoustic signal by sending in input a proper signal. We seen that using the parametric source, focusing at a proper distance, is possible to obtain a narrow acoustic beam, contained in $\pm 10°$, which is a signal very similar to the one induced by an UHE neutrino interacting in water.

To complete the study of the directivity of the source, we studied the signal distribution in the plane orthogonal to the source plane. We can conclude that the signal generated by the parametric source is narrow on the horizontal angle, while is nearly uniformly distributed all around the source. To complete the calibration we collected a sample of data for different values of the amplitude of the voltage input signal. Knowing the conversion factor from $[V]$ to $[Pa]$, we obtained the acoustic pulse in pressure.

Lastly, the fourth chapter concerns the simulation of the acoustic signal in water, induced by UHE neutrino interactions, using the ACoRNE program. After the estimation of the parametric source transfer function and of the attenuation in water, we could reconstruct the input signal that we have to apply to the source to obtain the bipolar pressure pulse; the voltage input signal obtained is shown in fig. 4.6.

The analyses described in Chapter 3 and Chapter 4 have been made using MATLAB. The data acquired and the codes used are reported in the appendices included.

Appendices

Appendix A

Beampattern Data

This appendix includes the data acquired at the IDASC.

Data in tables A.1 to A.6 concern the study of the directivity of the parametric source, that could rotate in the plan where the ceramics lay.

Tables A.7 to A.10 include the data of the angular beamsteering analysis, i.e. the possibility of changing the direction of the acoustic signal by sending in input to the source proper signals.

Thirdly, tables A.11 to A.14 contain data about the study of the directivity of the source, in the plane orthogonal to the source plane.

15 kHz				
Nominal angle [°]	**Real angle (±0,2) [°]**	**Amplitude [mV]**		
-90	-96,5	62,7	±	0,3
-75	-81,5	111,2	±	0,5
-60	-66,0	189,1	±	0,6
-45	-50,0	62,6	±	0,6
-30	-33,6	378,2	±	0,8
-15	-16,9	382,1	±	0,5
-14	-15,8	483,1	±	0,4
-13	-14,7	576,8	±	0,4
-12	-13,5	698,8	±	0,5
-11	-12,4	740,7	±	1,0
-10	-11,3	842,5	±	0,6
-9	-10,2	953,2	±	0,5
-8	-9,0	1068,0	±	0,8
-7	-7,9	1080,6	±	0,9
-6	-6,8	1190,8	±	0,9
-5	-5,6	1244,4	±	1,2
-4	-4,5	1209,5	±	2,5
-3	-3,4	1329,0	±	0,9
-2	-2,3	1353,7	±	0,9
-1	-1,1	1361,8	±	1,5
0	0,0	1362,7	±	1,1
1	1,1	1352,7	±	1,7
2	2,3	1331,5	±	1,8
3	3,4	1298,5	±	1,5
4	4,5	1250,0	±	0,8
5	5,6	1199,3	±	0,8
6	6,8	1102,0	±	1,6
7	7,9	1008,4	±	0,7
8	9,0	931,1	±	0,8
9	10,2	818,3	±	0,8
10	11,3	741,4	±	0,7
11	12,4	640,9	±	1,1
12	13,5	533,0	±	0,6
13	14,7	433,9	±	0,7
14	15,8	349,4	±	1,0
15	16,9	235,8	±	0,4
30	33,6	326,1	±	0,9
45	50,0	145,8	±	0,7
60	66,0	254,7	±	0,5
75	81,5	45,5	±	0,4
90	96,5	40,4	±	0,4

Table A.1. Nominal angle [°] and real angle [°] between the parametric source and the hydrophone, and amplitude [mV] measured rotating the source at $15\,kHz$.

20 kHz				
Nominal angle [°]	**Real angle (±0,2) [°]**	**Amplitude [mV]**		
-90	-96,5	42,4	±	0,4
-75	-81,5	57,2	±	0,5
-60	-66,0	203,0	±	0,5
-45	-50,0	251,6	±	0,8
-30	-33,6	53,6	±	0,9
-15	-16,9	143,8	±	0,6
0	0,0	1983,1	±	0,5
15	16,9	294,2	±	0,9
30	33,6	170,3	±	0,5
45	50,0	269,2	±	1,6
60	66,0	125,7	±	0,4
75	81,5	159,4	±	0,3
90	96,5	54,4	±	0,3

Table A.2. Nominal angle [°] and real angle [°] between the source and the hydrophone, and amplitude [mV] measured rotating the source at 20 kHz.

25 kHz				
Nominal angle [°]	Real angle (±0,2) [°]	Amplitude [mV]		
-15	-16,9	588,5	±	0,8
-14	-15,8	66,7	±	31,8
-13	-14,7	515,3	±	0,3
-12	-13,5	391,4	±	0,3
-11	-12,4	392,5	±	0,3
-10	-11,3	809,1	±	0,6
-9	-10,2	880,2	±	0,4
-8	-9,0	1421,0	±	0,6
-7	-7,9	1455,3	±	1,3
-6	-6,8	2037,6	±	1,1
-5	-5,6	2319,7	±	1,4
-4	-4,5	2767,6	±	0,8
-3	-3,4	2771,2	±	0,9
-2	-2,3	3075,7	±	1,5
-1	-1,1	3129,7	±	5,8
0	0,0	3211,5	±	1,2
1	1,1	3151,9	±	1,3
2	2,3	2950,5	±	0,9
3	3,4	2878,4	±	0,7
4	4,5	2565,9	±	0,6
5	5,6	1978,7	±	0,4
6	6,8	1978,5	±	0,4
7	7,9	1429,3	±	0,4
8	9,0	956,6	±	0,4
9	10,2	857,5	±	0,7
10	11,3	572,7	±	0,8
11	12,4	19,2	±	9,7
12	13,5	480,5	±	1,1
13	14,7	600,1	±	0,6
14	15,8	699,2	±	0,8
15	16,9	767,8	±	0,7

Table A.3. Nominal angle [°] and real angle [°] between the parametric source and the hydrophone, and amplitude $[mV]$ measured rotating the source at $25\,kHz$.

30 kHz				
Nominal angle [°]	Real angle (±0,2) [°]	Amplitude [mV]		
-90	-96,5	223,5	±	0,3
-75	-81,5	490,1	±	0,6
-60	-66,0	175,7	±	0,5
-45	-50,0	428,6	±	0,6
-30	-33,6	62,4	±	0,4
-15	-16,9	865,2	±	1,6
0	0,0	3782,9	±	2,5
15	16,9	757,1	±	0,7
30	33,6	51,9	±	1,1
45	50,0	393,1	±	1,0
60	66,0	420,5	±	1,3
75	81,5	580,6	±	0,6
90	96,5	258,8	±	0,4

Table A.4. Nominal angle [°] and real angle [°] between the parametric source and the hydrophone, and amplitude $[mV]$ measured rotating the source at $30\,kHz$.

35 kHz				
Nominal angle [°]	**Real angle (±0,2) [°]**	**Amplitude [mV]**		
-90	-96,5	912,3	±	0,7
-75	-81,5	1392,9	±	0,5
-60	-66,0	407,1	±	0,8
-45	-50,0	57,7	±	0,5
-30	-33,6	655,9	±	0,7
-15	-16,9	379,6	±	0,5
-14	-15,8	722,4	±	0,5
-13	-14,7	968,9	±	0,6
-12	-13,5	1148,7	±	0,4
-11	-12,4	1163,8	±	0,8
-10	-11,3	1071,3	±	1,0
-9	-10,2	764,1	±	0,6
-8	-9,0	506,3	±	1,0
-7	-7,9	548,3	±	0,9
-6	-6,8	1428,9	±	1,0
-5	-5,6	2164,4	±	1,2
-4	-4,5	3030,2	±	1,3
-3	-3,4	3545,2	±	1,4
-2	-2,3	4107,5	±	1,3
-1	-1,1	4334,7	±	2,5
0	0,0	4325,0	±	1,5
1	1,1	4189,2	±	1,4
2	2,3	3801,2	±	2,9
3	3,4	3332,9	±	1,2
4	4,5	2681,2	±	0,9
5	5,6	2128,9	±	0,8
6	6,8	1232,1	±	0,7
7	7,9	713,5	±	0,8
8	9,0	713,9	±	1,0
9	10,2	1036,2	±	0,8
10	11,3	1207,7	±	1,0
11	12,4	1291,5	±	1,0
12	13,5	1224,8	±	0,8
13	14,7	1046,7	±	0,8
14	15,8	840,2	±	0,5
15	16,9	521,9	±	0,4
30	33,6	103,8	±	30,0
45	50,0	208,0	±	0,9
60	66,0	355,4	±	0,8
75	81,5	1611,8	±	0,5
90	96,5	1083,2	±	0,4

Table A.5. Nominal angle [°] and real angle [°] between the parametric source and the hydrophone, and amplitude [mV] measured rotating the source at 35 kHz.

40 kHz				
Nominal angle [°]	**Real angle (±0,2) [°]**	**Amplitude [mV]**		
-90	-96,5	558,2	±	0,3
-75	-81,5	1606,0	±	0,4
-60	-66,0	3519,7	±	0,8
-45	-50,0	1376,5	±	0,7
-30	-33,6	293,4	±	0,6
-15	-16,9	590,9	±	0,5
0	0,0	4856,3	±	2,4
15	16,9	682,9	±	0,5
30	33,6	227,8	±	1,0
45	50,0	1153,6	±	0,8
60	66,0	3730,7	±	1,4
75	81,5	1766,3	±	0,5
90	96,5	820,5	±	0,5

Table A.6. Nominal angle [°] and real angle [°] between the parametric source and the hydrophone, and amplitude [mV] measured rotating the source at $40\,kHz$.

40 kHz at 150 cm			
Nominal angle [°]	**Amplitude [mV]**		
-15	488,6	±	0,1
-14	397,3	±	0,1
-13	231,4	±	0,1
-12	11,5	±	0,1
-11	236,4	±	0,1
-10	446,9	±	0,1
-9	570,3	±	0,1
-8	561,2	±	0,1
-7	403,2	±	0,1
-6	98,3	±	0,1
-5	393,0	±	0,1
-4	962,3	±	0,1
-3	1567,0	±	0,1
-2	2125,3	±	0,1
-1	2595,1	±	0,1
0	2904,0	±	0,1
1	3009,0	±	0,2
2	2896,2	±	0,2
3	2595,4	±	0,1
4	2123,1	±	0,1
5	1497,8	±	0,1
6	917,6	±	0,1
7	334,7	±	0,1
8	162,3	±	0,1
9	499,7	±	0,1
10	678,4	±	0,1
11	697,9	±	0,1
12	583,3	±	0,1
13	371,9	±	0,1
14	126,5	±	0,1
15	4,0	±	2,8

Table A.7. Amplitude $[mV]$ measured varying the beamsteering angle $[°]$ at $40\,kHz$ for the focus at $150\,cm$.

40 kHz at infinity			
Nominal angle [°]	**Amplitude [mV]**		
-15	542,6	±	0,1
-14	451,7	±	0,1
-13	282,5	±	0,1
-12	159,9	±	0,1
-11	349,9	±	0,1
-10	612,6	±	0,1
-9	817,9	±	0,1
-8	937,5	±	0,1
-7	957,9	±	0,1
-6	925,7	±	0,1
-5	966,0	±	0,1
-4	1195,2	±	0,1
-3	1585,7	±	0,1
-2	2013,4	±	0,1
-1	2399,3	±	0,1
0	2665,4	±	0,1
1	2757,4	±	0,2
2	2659,4	±	0,2
3	2388,1	±	0,1
4	1980,0	±	0,1
5	1385,4	±	0,1
6	1068,2	±	0,1
7	806,9	±	0,1
8	794,0	±	0,1
9	880,4	±	0,1
10	910,3	±	0,1
11	831,3	±	0,1
12	650,4	±	0,1
13	412,2	±	0,1
14	236,3	±	0,1
15	319,1	±	0,1

Table A.8. Amplitude $[mV]$ measured varying the beamsteering angle $[°]$ at $40\,kHz$ for the focus at infinity.

25 kHz at 150 cm			
Nominal angle [°]	**Amplitude [mV]**		
-30	341,7	±	0,1
-28	373,7	±	0,1
-26	351,9	±	0,1
-24	279,3	±	0,1
-22	220,0	±	0,1
-20	288,3	±	0,1
-19	355,0	±	0,1
-18	417,8	±	0,1
-17	460,9	±	0,1
-16	476,6	±	0,1
-15	456,2	±	0,1
-14	385,9	±	0,1
-13	267,9	±	0,1
-12	95,7	±	0,1
-11	136,0	±	0,1
-10	418,8	±	0,1
-9	739,3	±	0,1
-8	1102,9	±	0,1
-7	1480,1	±	0,1
-6	1874,5	±	0,1
-5	2261,9	±	0,1
-4	2626,8	±	0,2
-3	2953,5	±	0,2
-2	3225,5	±	0,2
-1	3435,7	±	0,2
0	3573,8	±	0,2
1	3629,8	±	0,3
2	3597,0	±	0,3
3	3488,1	±	0,3
4	3298,3	±	0,3
5	3040,7	±	0,3
6	2716,0	±	0,2
7	2341,5	±	0,2
8	1941,9	±	0,2
9	1515,3	±	0,2
10	1100,8	±	0,2
11	691,2	±	0,1
12	324,6	±	0,1
13	103,7	±	0,1
14	323,6	±	0,1

15	547,9	±	0,1
16	713,6	±	0,1
17	824,1	±	0,1
18	874,9	±	0,1
19	875,5	±	0,2
20	830,6	±	0,2
22	643,5	±	0,1
24	390,1	±	0,1
26	154,3	±	0,1
28	137,2	±	0,1
30	238,7	±	0,1

Table A.9. Amplitude $[mV]$ measured varying the beamsteering angle [°] at $25\,kHz$ for the focus at $150\,cm$.

25 kHz at infinity			
Nominal angle [°]	Amplitude [mV]		
-30	280,2	±	0,1
-28	329,2	±	0,1
-26	308,2	±	0,1
-24	211,1	±	0,1
-22	124,4	±	0,1
-20	282,6	±	0,1
-19	394,1	±	0,1
-18	500,4	±	0,1
-17	587,2	±	0,1
-16	651,0	±	0,1
-15	673,3	±	0,1
-14	665,1	±	0,1
-13	626,1	±	0,1
-12	568,4	±	0,1
-11	533,1	±	0,1
-10	590,7	±	0,1
-9	763,3	±	0,1
-8	1036,4	±	0,1
-7	1362,5	±	0,1
-6	1725,0	±	0,1
-5	2092,4	±	0,1
-4	2445,0	±	0,2
-3	2755,8	±	0,2
-2	3034,3	±	0,2
-1	3275,1	±	0,2
0	3436,9	±	0,3
1	3503,0	±	0,3
2	3515,3	±	0,3
3	3416,7	±	0,3
4	3271,0	±	0,3
5	3026,9	±	0,2
6	2754,6	±	0,2
7	2426,3	±	0,2
8	2077,7	±	0,2
9	1710,5	±	0,2
10	1358,2	±	0,2
11	1021,1	±	0,2
12	769,6	±	0,1
13	634,9	±	0,1
14	638,5	±	0,1

15	720,7	±	0,1
16	814,5	±	0,1
17	891,8	±	0,1
18	928,1	±	0,1
19	928,5	±	0,1
20	887,4	±	0,1
22	726,6	±	0,1
24	523,7	±	0,1
26	362,1	±	0,1
28	310,7	±	0,1
30	319,0	±	0,1

Table A.10. Amplitude $[mV]$ measured varying the beamsteering angle $[°]$ at $25\,kHz$ for the focus at infinity.

15 kHz				
Nominal angle [°]	Real angle (±0,2) [°]	Amplitude [mV]		
-90	-96,5	786,0	±	0,3
-80	-86,5	708,6	±	0,3
-70	-76,4	672,5	±	0,3
-60	-66,0	742,3	±	0,3
-50	-55,4	740,1	±	0,4
-40	-44,6	668,7	±	0,4
-30	-33,6	654,6	±	0,4
-20	-22,5	684,4	±	0,4
-10	-11,3	716,1	±	0,4
0	0,0	752,4	±	0,4
10	11,3	781,7	±	0,4
20	22,5	756,3	±	0,4
30	33,6	658,5	±	0,4
40	44,6	620,4	±	0,4
50	55,4	732,3	±	0,4
60	66,0	757,3	±	0,3
70	76,4	690,1	±	0,3
75	81,5	692,4	±	0,3
80	86,5	714,1	±	0,3
85	91,5	732,7	±	0,3
90	96,5	734,2	±	0,3

Table A.11. Nominal angle [°] and real angle [°] between the parametric source and the hydrophone, and amplitude [mV] measured rotating the source on a vertical plane at 15 kHz.

25 kHz				
Nominal angle [°]	**Real angle (±0,2) [°]**	**Amplitude [mV]**		
-90	-96,5	1524,1	±	0,1
-80	-86,5	1405,1	±	0,1
-70	-76,4	1520,7	±	0,1
-60	-66,0	1489,3	±	0,1
-50	-55,4	1449,8	±	0,1
-40	-44,6	1448,0	±	0,1
-30	-33,6	1462,8	±	0,1
-20	-22,5	1594,4	±	0,1
-10	-11,3	1723,1	±	0,1
0	0,0	1725,6	±	0,1
10	11,3	1511,6	±	0,1
20	22,5	1439,6	±	0,1
30	33,6	1620,3	±	0,1
40	44,6	1352,6	±	0,1
50	55,4	1377,1	±	0,1
60	66,0	1440,5	±	0,1
70	76,4	1360,9	±	0,1
71	77,4	1349,6	±	0,1
80	86,5	1406,2	±	0,1
90	96,5	1431,2	±	0,1

Table A.12. Nominal angle [°] and real angle [°] between the parametric source and the hydrophone, and amplitude [mV] measured rotating the source on a vertical plane at 25 kHz.

35 kHz				
Nominal angle [°]	**Real angle (±0,2) [°]**	**Amplitude [mV]**		
-90	-96,5	1794,2	±	0,1
-80	-86,5	1869,7	±	0,1
-70	-76,4	1965,5	±	0,1
-60	-66,0	1934,3	±	0,1
-50	-55,4	1951,5	±	0,1
-40	-44,6	2000,6	±	0,1
-30	-33,6	2195,7	±	0,1
-20	-22,5	2334,9	±	0,1
-10	-11,3	2333,1	±	0,1
0	0,0	2213,8	±	0,1
10	11,3	2304,6	±	0,1
20	22,5	2356,8	±	0,1
30	33,6	1881,8	±	0,1
40	44,6	2151,9	±	0,1
50	55,4	1734,7	±	0,1
60	66,0	1770,1	±	0,1
70	76,4	1849,3	±	0,1
80	81,5	1657,2	±	0,1
90	86,5	1556,5	±	0,1

Table A.13. Nominal angle [°] and real angle [°] between the parametric source and the hydrophone, and amplitude [mV] measured rotating the source on a vertical plane at 35 kHz.

40 kHz				
Nominal angle [°]	**Real angle (±0,2) [°]**	**Amplitude [mV]**		
-90	-96,5	2112,8	±	0,1
-85	-91,5	2094,7	±	0,1
-80	-86,5	1997,9	±	0,1
-75	-81,5	1972,9	±	0,1
-70	-76,4	1895,3	±	0,1
-65	-71,2	1950,7	±	0,1
-60	-66,0	2086,0	±	0,1
-55	-60,7	2215,5	±	0,1
-50	-55,4	2271,5	±	0,1
-45	-50,0	2454,3	±	0,1
-40	-44,6	2672,5	±	0,1
-35	-39,1	2726,2	±	0,1
-30	-33,6	2711,4	±	0,1
-25	-28,1	2724,3	±	0,1
-20	-22,5	2789,3	±	0,2
-15	-16,9	2824,4	±	0,1
-10	-11,3	2794,1	±	0,1
-5	-5,6	2716,0	±	0,1
0	0,0	2685,3	±	0,1
5	5,6	2738,7	±	0,1
10	11,3	2810,9	±	0,1
15	16,9	2750,7	±	0,1
20	22,5	2518,0	±	0,1
25	28,1	2446,0	±	0,1
30	33,6	2625,1	±	0,1
35	39,1	2503,9	±	0,1
40	44,6	2161,1	±	0,1
45	50,0	2220,3	±	0,1
50	55,4	2117,0	±	0,1
55	60,7	1681,2	±	0,1
60	66,0	1685,2	±	0,1
65	71,2	1805,9	±	0,1
70	76,4	1665,8	±	0,1
75	81,5	1592,8	±	0,1
80	86,5	1544,4	±	0,1
85	91,5	1762,3	±	0,1
90	96,5	1890,6	±	0,1

Table A.14. Nominal angle [°] and real angle [°] between the parametric source and the hydrophone, and amplitude [mV] measured rotating the source on a vertical plane at 40 kHz.

Appendix B

Computation of the Theoretical Beampattern

The following listing has been used to calculate the theoretical beampattern, as a function of the emission angle, for various frequencies. The computation is made by a function specifically defined, *beampattern.m*, that return the simulated amplitude, as the sum of the amplitudes (of every ceramic) arriving on the hydrophone, all over the chosen angular interval.

```
1   %This function takes in input these parameters:
    %f=frequency [Hz]
3   %alfa=angular interval [degree]
    %r=distance source-receiver [cm]
5   %vs=sound velocity in water [m/s]
    %num=mumber of ceramics
7   %delta=distance between ceramics [cm]

9   %The function returns the parameter simulated_amplitude all over
    %the angular interval.
11  %This is the module of the amplitude, calculated as the sum of
    %the amplitude of every ceramic arriving on the hydrophone.

13

15  function [simulated_amplitude] = beampattern(f,alfa,r,vs,num,delta)
```

```matlab
17
    %Check the accuracy of the input parameters
19
    %too few parameters
21  if nargin<2
        error('Insert␣at␣least␣two␣parameters');
23  end

25  %if the parameters are less than 3 add the third
    if nargin<3
27      r=150;
    end
29
    %if the parameters are less than 4 add the fourth
31  if nargin<4
        vs=1489;
33  end

35  %if the parameters are less than 5 add the fifth
    if nargin<5
37      num=8;
    end
39
    %if the parameters are less than 6 add the sixth
41  if nargin<6
        delta=4;
43  end

45  %too many parameters
    if nargin>6
47      error('Insert␣at␣most␣six␣parameters');
    end
49


51  x=-((num-1)*delta/2):delta:((num-1)*delta/2); %ceramics positions
    simulated_amplitude=zeros(1,length(alfa));
53  t0=(r/100)/vs; %propagation time from the centre of the source [s]
```

```matlab
55  %loop on every angle
    for k=1:length(alfa)
57          a=alfa(k)*pi/180;
            xr=r*sin(a);
59          yr=r*cos(a);

61  %loop on every ceramic
    for i=1:num
63          d=sqrt((x(i)-xr)^2+yr^2); %distance source-hydrophone [cm]
            t=(d/100)/vs; %arrival time on the hydrophone s
65          simulated_amplitude(k)=simulated_amplitude(k)+cos(2*pi*f*(t-t0));
    end
67
    simulated_amplitude(k)=abs(simulated_amplitude(k));
69  end


71  end
```

Appendix C

ACoRNE Acoustic Simulator

The following listing is an example code employed to generate a pulse at $1\,km$ from a $10^{11}\,GeV$ primary energy. It is available at the website https://www.hep.shef.ac.uk/research/acorne/shower.php.

The code is based on the use of a few functions and data files. There are four important functions; firstly *ShowerParm* that generates the shower parameters, supporting different energy parametrisations. The next function is *MCGEn*, that throws points by a Monte Carlo from the shower parametrisation matrix. The code takes into account the attenuation phenomena, that occur while the shower is propagating, using the function *atten_fna*; it calculates the attenuation in sea water through eight different models. The last and most important function is *kernelfr2*, that does the acoustic integration and returns the pressure pulse. An example of a simulated pulse is proposed in section 4.1.

```
1  rsc=[.5:9.5 15:10:105]; %radial bin centres (cm)
   zsc=10:20:2000;    %Longitudinal Bin Centres (cm)
3  Eo=1e11; %Primary Energy
   Do=[1e3 0 7.5]; % Position of observer
5  fs=1e6; %sampling frequency
   t_axis=(-512:511)/fs; %time axis for plot (default 1024 points)
7  atten=1; % Learned's attenuation
   nmc=1e4; % Number of MC points
9  tsmc=ShowerParm(rsc,zsc,Eo,'Sloan');
   %as the 10-100cm bins are 10x wider need to scale by a factor of 10
11 tsmc=tsmc*diag(kron([1 10],ones(1,10)));
   %generate MC points. Note bin EDGES need to be provided
```

```matlab
13  pointsc=MCGEn(tsmc,[0 zsc+10],[0 rsc+[0.5*ones(1,10) 5*ones(1,10)]],nmc);
    %Convert to Cartesian
15  [x,y,z]=pol2cart(rand(nmc,1)*2*pi,pointsc(:,2),pointsc(:,1));
    % Convert fom cm to m
17  points=[x y z]*1e-2;
    tic % start stopwatch
19  p=kernelfr2(points,Do,log10(Eo),atten,10);
    toc %generate time taken for integration
21  % Now plot
    %set(gca,'fonts',15)
23  plot(t_axis*1e3,p),xlabel('Time (ms)'),ylabel('Pressure (Pa)')
    %set(gca,'xlim',[-0.4 0.4])
25  title('Sample Pulse at 1 km')
```

Appendix D

Signal Computation

The following listing is the MATLAB code we have used to evaluate the input signals that we have to apply to the parametric source in order to obtain the propagated pressure wave, generated from hadronic shower. This code can estimate the coefficients of the transfer function of the apparatus and the attenuation factor in water medium. Then, moving to the Fourier space, we can multiply the signal by the transfer function and the attenuation, in order to obtain the propagated signal. This process can be done backwards knowing the bipolar pressure pulse, for example from the ACoRNE simulation, we are able to figure out the voltage input signal to use to generate this pulse.

The code takes in input the experimental data of amplitude and phase at various frequencies and computes the estimation of the coefficients $B(\omega)$ and $A(\omega)$ of the transfer function. Starting from the final pressure pulse, in fact, we can estimate the attenuation, both geometrically and from the Ainslie and McColm formula (4.3), and therefore, using the inverted transfer function, obtain the input signal. In the calculations we have used a low-pass filter on the data, with the cutoff frequency setted at $48\,kHz$, and we have setted the attenuation at a constant to avoid divergences.

```matlab
1  %%
   %clear all;
3
   %frequency (Hz) amplitude (Pa) and phase
5  daq_F=1e3*[15 20 25 30 35 40];
   daq_A=344*[1.362306 1.983580 3.211439 3.781197 4.323226 4.859709];
7  daq_P=[-0.597883 -0.775022 -0.665792 -0.914128 -1.196256 -2.026889];
   %complex transfer function
9  daq_H=daq_A.*exp(daq_P*1i);

11 %Constants
   Fs = 1e6; %Hz
13 N = 1024; %number of points
   Nyq = Fs/2; %Hz
15 dF=Fs/N; %frequency step (Hz)
   dT=1/Fs; %time step (s)
17 cnt_T=(0:N-1)*dT;
   cnt_F = (-N/2:N/2-1)*dF;
19 cnt_FP=(0:N/2-1)*dF;

21 Distanza=1; %km
   geo_A=1/(Distanza*1e3);
23
   %calculation of the coefficients of the filter from data
25 [b,a]=invfreqz(daq_H,daq_F*pi/Nyq,2,4,[],3000);
   %building the transfer function from the coefficients
27 h = freqz(b,a,cnt_FP,Fs);

29 %input signal
   %Ingresso=sin(2*pi*cnt_T*40000);%in Hz
31 Ingresso=p.'; %from ACoRNE
   %applying the filter calculated above
33 %Uscita=filter(b,a,Ingresso);
   %calculation of the attenuation in water
35 H=Attenuazione(cnt_F,Distanza);
   H=abs(H);
37 %propagation of the signal
```

```matlab
   %Uf=fft(Uscita);
39 %UPf=Uf.*fftshift(H);
   %Uscita_propagata=ifft(UPf);

41

   %backwards calculation
43 %Uscita_propagata=sin(2*pi*cnt_T*40000);
   Uscita_propagata=p.'; %from ACoRNE
45 %low-pass filter
   f_cut=48e3;

47

   [blp,alp] = butter(2,2*f_cut/Fs);
49 Uscita_propagata=filter(blp,alp,Uscita_propagata);


51 UPf=fft(Uscita_propagata/geo_A);
   H(find(abs(H)<1e-3))=1e-3;

53

   Uf=UPf./fftshift(H);
55 %Uf=UPf./H;
   Uscita=ifft(Uf);
57 Ingresso_ricostruito=filter(a,b,Uscita);
   Ingresso_nuovo=filter(blp,alp,Ingresso_ricostruito);

59


61 %%
   close all;

63

   figure;
65 %plot of the modulus of the transfer function
   subplot(3,2,1);
67 plot(cnt_FP,abs(h));
   hold on;
69 plot(daq_F,daq_A,'o-r');
   title('Transfer function');
71 xlabel('Frequency(Hz)');
   ylabel('Modulus');
73 xlim([0 100e3]);
   %plot of the phase of the transfer function
```

```matlab
75  subplot(3,2,3);
    plot(cnt_FP,angle(h));
77  hold on;
    plot(daq_F,daq_P,'o-r');
79  title('Transfer function');
    xlabel('Frequency(Hz)');
81  ylabel('Phase(rad)');
    xlim([0 100e3]);
83  %plot of the filter poles and zeros
    subplot(3,2,5);
85  zplane(b,a);
    %plot of the modulus of the attenuation in water
87  subplot(3,2,2);
    plot(cnt_F,abs(H));
89  title('Attenuation modulus');
    xlim([1e2 1e5]);
91  ylim([0 1]);
    grid on;
93  %plot of the phase of the attenuation in water
    subplot(3,2,4);
95  plot(cnt_F,angle(H));
    title('Attenuation phase');
97  xlim([1e2 1e5]);
    ylim([-pi pi]);
99  grid on;

101 figure;
    %plot of the input signal
103 %subplot(2,2,1);
    %plot(cnt_T,Ingresso);
105 %title('Input signal');
    %xlabel('Time(s)');
107 %ylabel('V');
    %gplot of the computed ouput signal
109 subplot(2,2,2);
    plot(cnt_T,real(Uscita));
111 title('Output signal');
```

```matlab
      xlabel('Time(s)');
113   ylabel('Pa');
      %plot of the propagated signal
115   subplot(2,2,3);
      plot(cnt_T,real(Uscita_propagata));
117   title('Propagated signal');
      xlabel('Time(s)');
119   ylabel('Pa');
      %plot of the input voltage signal
121   subplot(2,2,4);
      plot(cnt_T,real(Ingresso_ricostruito));
123   title('Computed input voltage signal');
      xlabel('Time(s)');
125   ylabel('V');


127   figure;
      %control plot on the filtered data
129   plot(abs(UPf),'b');
      hold on;
131   plot(abs(Uf),'r');
      hold on;
133   plot(1./abs(fftshift(H)),'g');
      xlim([0 200]);
135   grid on;
```

Bibliography

[1] Idasc Home Page. `http://www.idasc.cnr.it/`.

[2] MATLAB website. `https://it.mathworks.com/products/matlab.html`.

[3] ACoRNE website. `https://www.hep.shef.ac.uk/research/acorne/shower.php`.

[4] CRONIN, J. W., GAISSER, T. K., AND SWORDY, S. P. Cosmic rays at the energy frontier. *Scientific American*, **276** (1997).

[5] BLÜMER, J., ENGEL, R., AND HÖRANDEL, J. R. Cosmic rays from the knee to the highest energies. *Progress in Particle and Nuclear Physics*, **63** (2009). `http://www.sciencedirect.com/science/article/pii/S0146641009000362`, `doi:https://doi.org/10.1016/j.ppnp.2009.05.002`.

[6] BEREZINSKY, V. Extragalactic cosmic rays and their signatures. *Astroparticle Physics*, (2014). `http://www.sciencedirect.com/science/article/pii/S0927650513000595`, `doi:https://doi.org/10.1016/j.astropartphys.2013.04.001`.

[7] COLLABORATION, T. K.-G., ET AL. Kneelike structure in the spectrum of the heavy component of cosmic rays observed with kascade-grande. *arXiv preprint arXiv:1107.5885*, (2011).

[8] BERGMAN, D. R. AND BELZ, J. W. Cosmic rays: the second knee and beyond. *Journal of Physics G: Nuclear and Particle Physics*, (2007).

[9] SOKOLSKY, P. AND HiRes COLLABORATION. Final Results from the High solution Fly's Eye (HiRes) Experiment. *Nuclear Physics B Proceedings Supplements*, (2011). `arXiv:1010.2690`.

[10] ABU-ZAYYAD, T., ET AL. The cosmic-ray energy spectrum observed with the surface detector of the telescope array experiment. *The Astrophysical Journal Letters*, (2013).

[11] ABRAHAM, J., ET AL. Measurement of the energy spectrum of cosmic rays above 10^{18} ev using the pierre auger observatory. *Physics Letters B*, **685**.

[12] KAMPERT, K.-H. ET AL. Highlights from the pierre auger observatory. *arXiv preprint arXiv:1207.4823*, (2012).

[13] COLLABORATION, H. R. F. E., ET AL. First observation of the greisen-zatsepin-kuzmin suppression. *Physical Review Letters*.

[14] TSUNESADA, Y. ET AL. Highlights from telescope array. *arXiv preprint arXiv:1111.2507*, (2011).

[15] ABRAHAM, J., ET AL. Observation of the suppression of the flux of cosmic rays above 4×10^{19} eV. *Phys. Rev. Lett.*, (2008). `https://link.aps.org/doi/10.1103/PhysRevLett.101.061101`, doi:10.1103/PhysRevLett.101.061101.

[16] THE PIERRE AUGER COLLABORATION, ET AL. The Pierre Auger Observatory I: The Cosmic Ray Energy Spectrum and Related Measurements. *ArXiv e-prints*, (2011). `arXiv:1107.4809`.

[17] AHARONIAN, F. Galactic sources of high energy neutrinos. *Nuclear Physics B - Proceedings Supplements*, (2011). `http://www.sciencedirect.com/science/article/pii/S0920563211001526`, doi:https://doi.org/10.1016/j.nuclphysbps.2011.03.084.

[18] WAXMAN, E. Extra galactic sources of high energy neutrinos. *Physica Scripta*, (2005). `http://stacks.iop.org/1402-4896/2005/i=T121/a=022`.

[19] UCHIYAMA, Y., AHARONIAN, F. A., TANAKA, T., TAKAHASHI, T., AND MAEDA, Y. Extremely fast acceleration of cosmic rays in a supernova remnant. *Nature*, (2007). `http://dx.doi.org/10.1038/nature06210`.

[20] BELL, A. R. Cosmic ray acceleration in pulsar-driven supernova remnants. *Monthly Notices of the Royal Astronomical Society*, (1992). `arXiv:/oup/backfile/content_public/journal/mnras/257/3/10.1093/mnras/257.3.493/2/mnras257-0493.pdf`, doi:10.1093/mnras/257.3.493.

[21] AIELLO, S., ET AL. Sensitivity of an underwater Čerenkov km3 telescope to tev neutrinos from galactic microquasars. *Astroparticle Physics*, (2007). `http://www.sciencedirect.com/science/article/pii/S0927650507000448`, `doi:https://doi.org/10.1016/j.astropartphys.2007.03.003`.

[22] STECKER, F. W., DONE, C., SALAMON, M. H., AND SOMMERS, P. High-energy neutrinos from active galactic nuclei. *Phys. Rev. Lett.*, (1991).

[23] ATOYAN, A. AND DERMER, C. Neutrinos and γ-rays of hadronic origin from agn jets. *New Astronomy Reviews*, (2004). `http://www.sciencedirect.com/science/article/pii/S1387647303003695`, `doi:https://doi.org/10.1016/j.newar.2003.12.046`.

[24] HALZEN, F. AND HOOPER, D. High energy neutrinos from the tev blazar 1es 1959+650. *Astroparticle Physics*, (2005). `http://www.sciencedirect.com/science/article/pii/S0927650505000666`, `doi:https://doi.org/10.1016/j.astropartphys.2005.03.007`.

[25] PIRAN, T. Gamma-ray bursts and the fireball model. *Physics Reports*, (1999). `http://www.sciencedirect.com/science/article/pii/S0370157398001276`, `doi:https://doi.org/10.1016/S0370-1573(98)00127-6`.

[26] WAXMAN, E. AND BAHCALL, J. High energy neutrinos from cosmological gamma-ray burst fireballs. *Phys. Rev. Lett.*, (1997). `https://link.aps.org/doi/10.1103/PhysRevLett.78.2292`, `doi:10.1103/PhysRevLett.78.2292`.

[27] BARBOT, C., DREES, M., HALZEN, F., AND HOOPER, D. Neutrinos associated with cosmic rays of top-down origin. *Physics Letters B*, (2003). `http://www.sciencedirect.com/science/article/pii/S037026930300039X`, `doi:https://doi.org/10.1016/S0370-2693(03)00039-X`.

[28] MYERS, Z. AND NUSSER, A. Searching for neutrinos from wimp annihilations in the galactic stellar disc. *Monthly Notices of the Royal Astronomical Society*, (2008). `+http://dx.doi.org/10.1111/j.1365-2966.2008.13366.x`, `arXiv:/oup/backfile/content_public/journal/mnras/387/4/10.1111/j.1365-2966.2008.13366.x/2/mnras0387-1712.pdf`, `doi:10.1111/j.1365-2966.2008.13366.x`.

[29] GONDOLO, P., GELMINI, G., AND SARKAR, S. Cosmic neutrinos from unstable relic particles. *Nuclear Physics B*, (1993). `http://www.sciencedirect.com/science/article/pii/055032139390199Y`, `doi:https://doi.org/10.1016/0550-3213(93)90199-Y`.

[30] GREISEN, K. End to the cosmic-ray spectrum? *Phys. Rev. Lett.*, **16** (1966). `https://link.aps.org/doi/10.1103/PhysRevLett.16.748`, `doi:10.1103/PhysRevLett.16.748`.

[31] ZATSEPIN, G. T. AND KUZMIN, V. A. Upper limit of the spectrum of cosmic rays. *JETP Lett.*, **4** (1966), 78. [Pisma Zh. Eksp. Teor. Fiz.4,114(1966)].

[32] Lake BAIKAL Neutrino Telescope Home Page. `http://baikalweb.jinr.ru/`.

[33] AMANDA Home Page. `http://amanda.uci.edu/`.

[34] IceCube Home Page. `http://amanda.uci.edu/`.

[35] AGGOURAS, G., ET AL. NESTOR Deep Sea Neutrino Telescope: Deployment and results. *Nuclear Physics B - Proceedings Supplements*, **151** (2006). `http://www.sciencedirect.com/science/article/pii/S0920563205009394`, `doi:https://doi.org/10.1016/j.nuclphysbps.2005.07.060`.

[36] ANTARES Home Page. `http://antares.in2p3.fr/`.

[37] NEMO Home Page. `http://www.roma1.infn.it/km3/NEMO.html`.

[38] KM3NeT Home Page. `https://www.km3net.org/`.

[39] HiRes Home Page. `http://www.cosmic-ray.org/`.

[40] PAO Home Page. `https://www.auger.org/`.

[41] TA Home Page. `http://www.telescopearray.org/`.

[42] DE OLIVEIRA, M. Pierre auger observatory: status report. *Brazilian journal of physics*, **34** (2004).

[43] ASKARYAN, G. A. Excess negative charge of electron-photon shower and the coherent radiation originating from it. Radiorecording of showers under the ground and on the moon. *J. Phys. Soc. Japan*, (1962). `http://www.osti.gov/scitech/servlets/purl/4754120`.

[44] MIOCINOVIC, P., ET AL. Tuning into UHE Neutrinos in Antarctica - The ANITA Experiment. *arXiv preprint astro-ph/0503304*, (2005).

[45] ARA Home Page. `https://ara.wipac.wisc.edu/home`.

[46] VANDENBROUCKE, J., GRATTA, G., AND LEHTINEN, N. Experimental study of acoustic ultra-high-energy neutrino detection. *The Astrophysical Journal*, **621** (2005).

[47] ACoRNE Home Page. `https://www.hep.shef.ac.uk/research/acorne/`.

[48] COSENTINO, L., FAVETTA, M., LAROSA, G., PAVAN, G., ROMEO, D., PRIVITERA, S., SPEZIALE, F., COLLABORATION, N., ET AL. NEMO-OνDE a submarine station for real-time monitoring of acoustic background installed at 2000 m depth in the mediterranean sea. *arXiv preprint arXiv:0804.2913*, (2008).

[49] LAHMANN, R. Status and first results of the acoustic detection test system AMADEUS. *Nuclear Instruments and Methods in Physics Research Section A: Accelerators, Spectrometers, Detectors and Associated Equipment*, **604** (2009). `http://www.sciencedirect.com/science/article/pii/S016890020900504X`, doi:`https://doi.org/10.1016/j.nima.2009.03.058`.

[50] SMO Project. `https://www.lns.infn.it/it/applicazioni/attivita-interdisciplinari-marine.html`.

[51] SIMEONE, F. ET AL. Underwater acoustic detection of uhe neutrinos with the antares experiment. *arXiv preprint arXiv:0908.0862*, (2009).

[52] GANDHI, R., QUIGG, C., RENO, M. H., AND SARCEVIC, I. Ultrahigh-energy neutrino interactions. *Astroparticle Physics*, **5** (1996). `http://www.sciencedirect.com/science/article/pii/0927650596000084`, doi:`https://doi.org/10.1016/0927-6505(96)00008-4`.

[53] KLEIN, S. R. Bremsstrahlung and pair creation: Suppression mechanisms and how they affect ehe air showers. In *AIP Conference Proceedings CONF-9711122*, vol. 433, pp. 132–147. AIP (1998).

[54] LANDAU, L. D. AND POMERANCHUK, I. Limits of applicability of the theory of bremsstrahlung electrons and pair production at high-energies. *Dokl. Akad. Nauk Ser. Fiz.*, **92** (1953), 535.

[55] Landau, L. D. and Pomeranchuk, I. Electron cascade process at very high-energies. *Dokl. Akad. Nauk Ser. Fiz.*, **92** (1953), 735.

[56] Migdal, A. B. Bremsstrahlung and pair production in condensed media at high energies. *Phys. Rev.*, **103** (1956), 1811. `https://link.aps.org/doi/10.1103/PhysRev.103.1811`, `doi:10.1103/PhysRev.103.1811`.

[57] Niess, V. and Bertin, V. Underwater acoustic detection of ultra high energy neutrinos. *Astroparticle Physics*, **26** (2006). `http://www.sciencedirect.com/science/article/pii/S0927650506000971`, `doi:https://doi.org/10.1016/j.astropartphys.2006.06.005`.

[58] Askaryan, G. Hydrodynamic radiation from the tracks of ionizing particles in stable liquids. *The Soviet Journal of Atomic Energy*, **3** (1957).

[59] Lehtinen, N. G., Adam, S., Gratta, G., Berger, T. K., and Buckingham, M. J. Sensitivity of an underwater acoustic array to ultra-high energy neutrinos. *Astroparticle Physics*, **17** (2002). `http://www.sciencedirect.com/science/article/pii/S092765050100158X`, `doi:https://doi.org/10.1016/S0927-6505(01)00158-X`.

[60] Bevan, S., et al. Simulation of ultra high energy neutrino induced showers in ice and water. *Astroparticle Physics*, **28** (2007).

[61] Wilson, W. D. Equation for the speed of sound in sea water. *The Journal of the Acoustical Society of America*, **32** (1960).

[62] Riccobene, G., et al. Deep seawater inherent optical properties in the southern ionian sea. *Astroparticle Physics*, **27** (2007).

[63] Learned, J. G. Acoustic radiation by charged atomic particles in liquids: An analysis. *Phys. Rev. D*, **19** (1979). `https://link.aps.org/doi/10.1103/PhysRevD.19.3293`, `doi:10.1103/PhysRevD.19.3293`.

[64] Ainslie, M. A. and McColm, J. G. A simplified formula for viscous and chemical absorption in sea water. *The Journal of the Acoustical Society of America*, **103** (1998).

[65] Gaisser, T. K., Engel, R., and Resconi, E. *Cosmic Rays and Particle Physics*. Cambridge University Press (2016).

[66] DE BONIS, G. Acoustic detection of ultra-high-energy cosmic neutrinos.

[67] SIMEONE, F. Detection of underwater acoustic signals induced by ultra-high energy neutrinos interactions.

[68] KULIKOV, G. AND KHRISTIANSEN, G. On the size spectrum of extensive air showers. *SOVIET PHYSICS JETP-USSR*, (1959).

List of Figures

List of Tables